UNIVERSIDAD COMPLUTENSE DE MADRID
FACULTAD DE CIENCIAS FÍSICAS
DEPARTAMENTO DE FÍSICA ATÓMICA, MOLECULAR Y NUCLEAR

TESIS DOCTORAL

Measurement of π^0 meson properties through its *Dalitz* decay channel in pp and p-Pb collisions with the ALICE experiment at the LHC

Medida de propiedades de π^0 usando la desintegración *Dalitz* en el experimento ALICE del LHC en colisiones pp y p-Pb

MEMORIA PARA OPTAR AL GRADO DE DOCTOR

PRESENTADA POR

Pedro González Zamora

DIRECTORES

Ana María Marín García
Pedro Ladrón de Guevara Montero

Madrid, 2017

CENTRO DE INVESTIGACIONES, ENERGÉTICAS MEDIOAMBIENTALES Y TECNOLÓGICAS

(CIEMAT-MADRID)

Ciemat

UNIVERSIDAD COMPLUTENSE DE MADRID

FACULTAD DE CIENCIAS FÍSICAS
DEPARTAMENTO DE FÍSICA ATÓMICA, MOLECULAR Y NUCLEAR

TESIS DOCTORAL

Medida de las propiedades del π^0 usando la desintegración "Dalitz" en el experimento ALICE del LHC en colisiones pp y p–Pb

MEMORIA PARA OPTAR AL GRADO DE DOCTOR

PRESENTADA POR

Pedro González Zamora

DIRECTORES

ANA MARÍA MARÍN GARCÍA
PEDRO LADRÓN DE GUEVARA MONTERO

Madrid, 2016

CENTRO DE INVESTIGACIONES, ENERGÉTICAS MEDIOAMBIENTALES Y TECNOLÓGICAS

(CIEMAT-MADRID)

Ciemat

UNIVERSIDAD COMPLUTENSE DE MADRID

FACULTAD DE CIENCIAS FÍSICAS

DEPARTAMENTO DE FÍSICA ATÓMICA, MOLECULAR Y NUCLEAR

Measurement of π^0 meson properties through its "Dalitz" decay channel in pp and p–Pb collisions with the ALICE experiment at the LHC

THESIS SUBMITTED FOR THE DEGREE OF

DOCTOR OF PHILOSOPHY

BY

Pedro González Zamora

SUPERVISED BY

ANA MARÍA MARÍN GARCÍA

PEDRO LADRÓN DE GUEVARA MONTERO

Madrid, 2016

Abstract

Quarks and gluons are elementary particles described in the Standard Model of particle physics which have never been observed free in nature. Quarks are always bound with other quarks through gluons (which are the force carriers of the strong force) forming other particles named hadrons. However, the Quantum Chromodynamics theory (QCD), which is the theory that describes the strong force, predicts that at extreme conditions of temperature and density quarks and gluons behave as quasi-free particles. The phase transition from hadronic matter to a state of free quarks and gluons is known as Quark-Gluon Plasma (QGP) and is believed to have existed shortly after the Big Bang.

Ultra-relativistic Heavy-ion Collisions is the field of Physics that allows to study the QGP in the laboratory since extreme conditions of temperature and energy are expected to occur in such collisions.

The Large Hadron Collider (LHC) is the most powerful particle accelerator in the world. It has a circumference of 27 km and is located at the border between Switzerland and France, close to Geneva. Although the LHC has been designed to study the Physics of the Higgs Boson, it also includes a program of ultra-relativistic heavy-ion collisions (Pb–Pb). The experiment installed at the LHC optimized for the study of the QGP is called ALICE (A Large Ion Collider Experiment).

The QGP formed in ultra-relativistic heavy-ion collisions has a lifetime so short that it is not possible to observe it directly. Instead, it is studied by analyzing the properties of the thousands of particles produced during the collision. Within the variety of observables proposed as signatures of the QGP, there is one known as "jet quenching". The phenomenon of jet quenching refers to a hadron suppression at intermediate and high transverse momentum (p_{T}) in nucleus-nucleus collisions with respect to their production in nucleon-nucleon collisions at the same center-of-mass collision energy and was first observed at the RHIC experiments. The first measurements on charged hadrons and neutral mesons (π^0) production in Pb–Pb collisions at $\sqrt{s_{\mathrm{NN}}}$ = 2.76 TeV reported by ALICE, have also shown a suppression in their production at $p_{\mathrm{T}} > 2$ GeV/c. In order to give a definitive conclusion of what was observed, one has to be sure that the hadron suppression is due to effects of the QGP formation (also known as final-state effects) and not due to initial-state effects also known as cold nuclear matter (CNM) effects. The CNM effects can be studied in pp and p–Pb collisions by computing the so-called "nuclear modification factor $R^{\pi^0}_{\mathrm{pPb}}$".

The aim of this thesis is to measure the π^0 meson production in proton-lead (p–Pb) collisions at $\sqrt{s_{\mathrm{NN}}}$ = 5.02 TeV and in proton-proton (pp) collisions at $\sqrt{s}$ = 2.76

TeV and $\sqrt{s}$ = 7 TeV in order to disentangle initial- from final-state effects in the π^0 meson suppression observed in Pb–Pb collisions. The measurement of the π^0 meson production in pp and p–Pb collisions is also important for testing model calculations such as pQCD NLO and Color-Glass Condensate since it is dominant at low Bjorken-x energy scale. Moreover, the measurement of the π^0 spectra is necessary for the analysis of direct photons since π^0s are the main source of photons and therefore, they are the main source of background in that study. Additionally, the work of this thesis provides an additional method to the existing ones in ALICE for the π^0 meson detection. This method reconstructs the π^0 meson in its Dalitz decay channel ($\pi^0 \rightarrow e^- e^+ \gamma$) which allows to cross-check the description of the material thickness and its estimated precision when compared to the measurement of the π^0 in its 2-γ decay channel. The detection of virtual photons (γ^*) requires the reconstruction of an electron-positron pair coming from the main interaction. The two primary electrons are reconstructed using the main ALICE tracking detectors, the TPC and the ITS. Moreover, the particle identification is carried out by using the specific energy loss ($\mathrm{d}E/\mathrm{d}x$) of electrons when they cross the TPC detector. On the other hand, photons (γ) are reconstructed through the detection of their conversion products ($\gamma \rightarrow e^+ e^-$) in the ALICE central barrel using the Photon Conversion Method (PCM).

This thesis analyzes data collected by ALICE during the LHC Run1 (2010-2013) in pp collisions at $\sqrt{s}$ = 2.76 TeV and at $\sqrt{s}$ = 7 TeV and in p–Pb collisions at $\sqrt{s_{\mathrm{NN}}}$ = 5.02 TeV with a minimum bias trigger.

The π^0 meson is then obtained by computing the invariant mass distribution of the virtual photons and photons ($\gamma^*\gamma$). The resulting combinatorial background is estimated using the mixed event technique which combines photons and virtual photons from different events. After background subtraction the π^0 meson signal is fitted with a gaussian function convoluted with an exponential and a linear function. The π^0 meson raw yield in each bin of p_{T} is obtained by integrating the π^0 meson signal. The integration window is obtained by a gaussian fit. Using Monte Carlo simulations that use PYTHIA, PHOJET and HIJING as particle generators and GEANT3 as a package transport, the π^0 meson raw yield is corrected by the number of analyzed events, efficiency, acceptance, contamination and Dalitz Branching ratio. The systematic errors are computed by varying every cut used in the virtual photon, the photon, and the π^0 meson reconstruction. The largest deviations from the corrected yield and the one obtained by varying one cut at a time are obtained.

The resulting invariant differential π^0 meson yield spectra at the three energies were fitted with the Tsallis function. Moreover, the spectra were compared with the ones obtained by other independent methods that measure π^0s through their 2-γ decay channel using the PCM method and the electromagnetic calorimeters PHOS and EMCal. A good agreement is observed in the three systems under study.

The pQCD model calculations using Particle Distribution Functions (PDFs) MSTW with the newest Parton-to-Hadron Fragmentation Functions (FFs) DSS14 reproduce the shape of the pp spectrum at $\sqrt{s}$ = 7 TeV and they are in agreement with the results obtained in pp collisions at $\sqrt{s}$ = 2.76 TeV in the range $2 < p_{\mathrm{T}} < 5$ GeV/c. The comparison between PYTHIA 8 Tune 4C and 2.76 TeV results shows also a good

agreement in the p_{T} range of 0.8-5.0 GeV/c.

In order to quantify possible nuclear effects on the π^0 meson production for $p_{\mathrm{T}} > 2$ GeV/c, the nuclear modification $R^{\pi^0}_{\mathrm{pPb}}$ was computed. As pp collisions at $\sqrt{s}$ = 5.02 TeV, were not taken at the LHC Run1, the pp reference needed for the $R^{\pi^0}_{\mathrm{pPb}}$ was calculated using an interpolation method. This method assumes a power-law behaviour of the π^0 meson production in pp collisions. As an input for the interpolation method, the PCM part of the published measurements in pp at $\sqrt{s}$ = 2.76 TeV and at $\sqrt{s}$ = 7 TeV were used.

The $R^{\pi^0}_{\mathrm{pPb}}$ shows a compatibility with unity for transverse momenta above 2 GeV/c. This indicates that the suppression observed in Pb–Pb collisions is due to the Quark-Gluon Plasma formation. Color-Glass Condensate (CG) predictions and pQCD NLO EPS09s describe, within the uncertainties of the measurement, the measured $R^{\pi^0}_{\mathrm{pPb}}$.

Resumen

Los quarks y los gluones son partículas elementales descritas en el modelo estándar de la física de partículas que nunca han sido observadas libres en la naturaleza. Los quarks siempre están unidos a otros quarks por medio de gluones (quienes actúan como portadores de la interacción nuclear fuerte) formando otra clase de partículas llamadas hadrones. Sin embargo, la teoría de la Cromodinámica Cuántica (la teoría que describe la interacción nuclear fuerte), predice que en condiciones extremas de temperatura y densidad los quarks y los gluones se comportan como partículas casi libres. La transición de fase de la materia hadrónica al estado de quarks y gluones libres se conoce como Plasma de Quarks y Gluones (QGP, por sus siglas en inglés) y ésta pudo haber existido poco después del Bing Bang.

Las propiedades del QGP pueden estudiarse en el laboratorio mediante colisiones de iones pesados ultra-relativistas. Esto es debido a que en dichas colisiones se alcanzan condiciones de extrema temperatura y densidad, condiciones necesarias para la formación del QGP.

El Gran Colisionador de Hadrones (LHC, por sus siglas en inglés) es el acelerador de partículas más potente que existe en el mundo actualmente. El LHC tiene una forma circular y un diámetro de aproximadamente 27 kilómetros y se encuentra ubicado entre la frontera suiza y francesa, cerca de la ciudad de Ginebra. Aunque el LHC fue diseñado para estudiar la física del Bosón de Higgs, también incluye dentro de su programa colisiones de iones pesados (Pb–Pb). El experimento diseñado para el estudio del QGP en el LHC se llama ALICE (A Large Ion Collider Experiment).

El QGP creado en colisiones de iones pesados ultra-relativistas tiene una vida muy corta, por lo tanto su estudio se lleva a cabo analizando las propiedades de miles de partículas producidas durante dichas colisiones. Entre las señales que indican la formación del QGP, se encuentra la supresión de hadrones a intermedio y alto momento transverso (p_{T}) en collisiones núcleo-núcleo con respecto a su producción en colisiones nucleón-nucleón a la misma energía en el centro de masas. Este fenómeno es conocido como *jet quenching* y fue observado por primera vez en los experimentos de RHIC. La medida de la producción de hadrones cargados y mesones neutros (π^0) en colisiones Pb–Pb para energías en el centro de masas de $\sqrt{s_{\mathrm{NN}}}$ = 2.76 TeV hechas por ALICE, presentan una supresión para $p_{\mathrm{T}} > 2$ GeV/c. Para poder dar conclusiones definitivas sobre estas observaciones es importante asegurar que esta supresión es debida a efectos de la formación del QGP (también conocidos como efectos del estado final) y no debida a efectos del estado inicial también conocidos

como efectos de la materia nuclear fría (CNM, por sus siglas en inglés). Los efectos de la CNM pueden estudiarse en colisiones protón-protón (pp) y protón-Plomo (p–Pb) mediante el cálculo del "factor de modificación nuclear $R^{\pi^0}_{\rm pPb}$".

El objetivo de esta tesis es medir la producción del π^0 en colisiones protón-Plomo (p–Pb) para energías en el centro de masas de $\sqrt{s_{\rm NN}}$ = 5.02 TeV y en colisiones protón-protón para energías en el centro de masas de $\sqrt{s}$ = 2.76 TeV y $\sqrt{s}$ = 7 TeV. La medida de la producción del π^0 en colisiones pp y p–Pb también es importante para probar modelos teóricos tales como "pQCD NLO" y "Color-Glass Condensate" ya que ésta es dominante a bajos valores de energía en la escala de "Bjorken-x". Además, estas medidas son importantes para el estudio de fotones directos ya que los π^0 son la principal fuente de fotones y por lo tanto la principal fuente de contaminación en ese estudio. Adicionalmente, esta tesis proporciona un nuevo método para detectar π^0s en ALICE a través de su canal de desintegración Dalitz ($\pi^0 \rightarrow \gamma^*\gamma \rightarrow e^-e^+\gamma$). Este canal de desintegración permite comprobar la descripción del espesor del material y su precisión estimada por medio de la comparación con la medida del π^0 hecha a través de su canal de desintegración 2-γ. La detección de los fotones virtuales (γ^*) requiere de la reconstrucción de pares de electrones (positivos y negativos) provenientes de la interacción principal. Los electrones han sido reconstruidos utilizando los principales detectores en ALICE para la reconstrucción de trazas, ITS y TPC. La identificación de electrones se lleva a cabo mediante la medida de la perdida de energía por unidad de longitud ($\mathrm{d}E/\mathrm{d}x$) en la TPC. Por otro lado, los fotones (γ) son reconstruidos a través de la detección de sus productos de conversión ($\gamma \rightarrow e^-e^+$) utilizando un método llamado "Photon Conversion Method (PCM)".

En esta tesis se analizan datos tomados por el experimento ALICE durante la primera fase del funcionamiento del LHC en colisiones pp con energías en el centro de masas de $\sqrt{s}$ = 2.76 TeV y $\sqrt{s}$ = 7 TeV y en colisiones p–Pb con energías en el centro de masas de $\sqrt{s_{\rm NN}}$ = 5.02 TeV utilizando un disparador de sesgo mínimo (MB, por sus siglas en inglés).

El π^0 se obtiene calculando la masa invariante de pares $\gamma^*\gamma$. El ruido combinatorio se estima usando la técnica de mezcla de sucesos, la que combina fotones virtuales con fotones de diferentes sucesos. Después de restar el ruido de fondo, la señal del π^0 es ajustada utilizando una convolución entre una función gaussiana, una función exponencial y una función lineal. La producción del π^0 se obtiene mediante la integración de la señal del π^0 en diferentes intervalos de $p_{\rm T}$. La ventana de integración se obtiene tomando en cuenta los valores del ajuste. Mediante simulaciones Monte Carlo que utilizan PYTHIA, PHOJET y HIJING como generadores de partículas y GEANT3 para simular la propagación de estas en el detector, la producción del π^0 es corregida por el número de sucesos analizados, eficacia de reconstrucción, aceptancia, contaminación y "Dalitz Branching Ratio". Los errores sistemáticos son calculados variando cada uno de los cortes utilizados en la reconstrucción del fotón virtual, del fotón y la extracción de la señal del π^0.

Los espectros de la producción diferencial invariante del π^0 obtenidos en esta tesis han sido ajustados con la función Tsallis. Además, estos espectros han sido comparados con aquellos obtenidos por métodos independientes al nuestro y que miden π^0s a través de su canal de desintegración 2-γ usando el método PCM y los calorímetros

electromagnéticos PHOS y EMCal. Un buen acuerdo se observa en las tres energías bajo estudio.

La sección eficaz invariante del π^0 medida en colisiones pp ha sido comparada con modelos teóricos basados en pQCD (NL0 pQCD) MSTW que utilizan la nueva versión de "Parton-to-Hadron Fragmentation Functions (FFs)" DSS14. La teoría reproduce la forma del espectro para energía en el centro de masas de $\sqrt{s}$ = 7 TeV y esta en acuerdo con el espectro a $\sqrt{s}$ = 2.76 TeV en el rango 2 < p_{T}< 5.0 GeV/c. Además, la sección eficaz invariante del π^0 en colisiones pp ha sido comparada con PYTHIA 8 Tune 4C mostrando un buen acuerdo en el rango 0.8 < p_{T}< 5 GeV/c.

Para cuantificar posibles efectos nucleares en colisiones p–Pb en la producción del π^0 para $p_{\mathrm{T}} > 2$ GeV/c, el factor de modificación nuclear ($R^{\pi^0}_{\mathrm{pPb}}$) fue calculado. Debido a que datos de colisiones pp a $\sqrt{s}$ = 5.02 TeV no fueron tomados durante la primera fase de funcionamiento del LHC, la referencia en colisionas protón-protón (necesaria para el cálculo del $R^{\pi^0}_{\mathrm{pPb}}$) fue obtenida mediante un método de interpolación que asume un comportamiento en ley de potencia de la producción del π^0 en dichas colisiones. Como datos de entrada para el método de interpolación se usaron las medidas de la producción del π^0 en colisiones pp a $\sqrt{s}$ = 2.76 TeV y a $\sqrt{s}$ = 7 TeV publicadas por ALICE y que fueron hechas midiendo el π^0 a través de su canal de desintegración 2-γ con el método PCM.

El $R^{\pi^0}_{\mathrm{pPb}}$ medido por esta tesis es compatible con la unidad para valores de p_{T} superiores a 2 GeV/c como se esperaría en la ausencia de efectos nucleares. Esto nos indica que la supresión del π^0 observada en colisiones Pb–Pb a $\sqrt{s}$ = 2.76 TeV son debidas a la formación del Plasma de quarks y gluones. Además nuestro $R^{\pi^0}_{\mathrm{pPb}}$ está en acuerdo con predicciones teóricas basadas en modelos pQCD NLO EPS09s y "Color-Glass Condensate".

A mis padres
To my parents

Acknowledgements

En primer lugar me gustaría agradecer a mis directores de tesis al Dr. Pedro Ladrón de Guevara y a la Dra. Ana María Marín García, por su esfuerzo, dedicación y orientación en la realización de esta tesis, así como su enorme paciencia para conmigo. Gracias a ambos por compartir conmigo sus conocimientos y por hacer de mi una mejor persona.

También me gustaría agradecer al CIEMAT por todas las facilidades prestadas y por haberme brindado un espacio de trabajo durante casi 9 años. Muy especialmente a José Manuel Pérez y a Fernando Blanco Marcilla.

Estoy muy agradecido con la Prof. Johanna Stachel por darme la oportunidad de realizar dos estancias de investigación en la Universidad de Heidelberg. Dichas estancias han sido de gran ayuda para realización de este trabajo y también para mi formación profesional.

Quiero agradecer a los miembros del grupo de fotones (PCG), en especial al Dr. Klaus Reygers, Annika Passfeld, Friederike Bock y Lucia Leardini por sus valiosas observaciones y consejos durante las reuniones de grupo.

También quiero agradecer al GSI, Darmstadt por permitirme usar las facilidades informáticas para el análisis de los datos del experimento ALICE.

Agradezco al Consejo Nacional de Ciencia y Tecnología de México (CONACYT) por haberme apoyado con una beca de doctorado para la realización de esta tesis.

Por último, me gustaría agradecer a todas las personas maravillosas que he conocido durante mi estancia en Madrid y que se volvieron parte de mi familia. En especial a Daniel Pérez, Priscilla Vergara, Itziguari Pérez, Javier Francisco, Álvaro Pavón, Jurgen, Diego León, Daniel Martínez y Bea. Gracías a todos por su amistad y apoyo anímico.

I would like to thank my supervisors Dr. Pedro Ladrón de Guevara y Dr. Ana María Marín García for the their efforts, dedication and direction for the realization of this thesis as well as for their enormous patience with me. Thanks both for sharing your knowledge with me and for making me a better person.

I would like to thank to CIEMAT for the facilities provided and for giving me a workspace during almost 9 years. Specially, I would like to thank to José Manuel Pérez and Fernando Blanco Marcilla.

I would also like to thank to Prof. Johanna Stachel for giving me the opportunity to do research stays in the University of Heidelberg. Such stays have been very important for carrying out this work and they also have been important for my professional training.

I would like to thank to all members of the photon conversion group (PCG), specially to Dr. Klaus Reygers, Annika Passfeld, Friederike Bock and Lucia Leardini for their value comments and advise during the meeting groups.

I would also like to thank to GSI, Darmstadt for the facilities and services provided; they were important for the analysis of the data of the ALICE experiment.

I would like to thank to Consejo Nacional de Ciencia y Tecnología de México (CONACYT) for its financial support thorugh a PhD Scholarship.

Finally, I would like to thank all the people who I have met during my stay in Madrid; they became part of my family. Specially, Daniel Pérez, Priscilla Vergara, Itziguari Pérez, Javier Francisco, Alvaro Pavón, Jurgen, Diego León, Daniel Martínez y Bea. Thanks all of you for your frienship and personal support.

Contents

List of Figures

List of Tables

Glossary

ALICE	A Large Ion Collinder Experiment
ATLAS	A Toroidal LHC ApparatuS
CGC	Color-Glass Condesate
CMS	Compact Muon Solenoid
DCA	Distance of closest approach
EMCal	Electromagnetic Calorimeter
ITS	Inner Tracking System
LHC	Large Hadron Collinder
PHENIX	A Physics Experiment at RHIC
PHOS	Photon Spectrometer
QCD	Quantum Chromodynamics
QED	Quantum Electrodynamics
QGP	Quark-Gluon Plasma
RHIC	Relativistic Heavy Ion Collinder
SPD	Silicon Pixel Detector
SPS	Super Proton Synchrotron
SSD	Silicon Strip Detector
STAR	Solenoidal Tracker at RHIC
TOF	Time of Flight Detector
TPC	Time Projection Chamber
TRD	Transition Radiation Detector

Introduction

One of the oldest questions that humans made themselves is “what is the origin of the universe?”. Among the suggested theories that try to answer this question, there is one called the Big Bang Theory which says that the universe was formed after a big explosion.

According to the Big Bang Theory, before the big explosion, the universe was extremely dense that all matter was concentrated in a limited space. Moreover, the Physics laws that we know until now may not exist or they behaved differently. For unclear reasons, the universe experimented an exponential expansion. This expansion lead the universe to cool down and form fundamental particles. At one point, it is believed that matter was dissolved into its constituents in a hot soup of quarks and gluons. Later, the expansion of the universe lead to colder temperatures that quarks were bound by gluons and formed protons and neutrons. At one stage protons and neutrons combined each other and formed light nuclei which in turn combined with electrons and formed atoms. Subsequently, the fusion of atoms created stellar objects like stars, planets and galaxies.

Continuous efforts of humans trying to understand the origin of everything and the fundamental ingredients of matter have lead to the development of the Standard Model of particle physics which has shown to describe many aspects of matter and interacting forces existing in the universe precisely. However, many other aspects remain unknown as gravitational force, dark matter, etc., and therefore, the Standard Model is in continuous development.

The Large Hadron Collider (LHC) is intended to answer questions of the Standard Model like what is the mechanism that gives particles the property of mass; the Higgs Bosson. It also tries to study how the matter behaves at conditions of high temperature and density, similarly to the conditions that prevailed at earliest stages of the universe where the matter is believed to be dissociated into a plasma composed of gluons and quarks; the Quark-Gluon Plasma (QGP). There is one experiment primarly devoted to the study of the QGP in the LHC called ALICE.
One of the signatures proposed to proof the formation of the QGP is the hadron suppression at intermediate and high p_{T}. The first measurements of the π^0 meson production in Pb–Pb collisions at $\sqrt{s_{\mathrm{NN}}}$ = 2.76 TeV reported by ALICE show a suppression (strongest in most central events) at transverse momenta higher than 2 GeV/c compared to that in pp collisions at the same center of mass energy. This suppression was also observed in RHIC experiments at $\sqrt{s_{\mathrm{NN}}}$ = 200 GeV. However, the suppression observed can also be due to cold nuclear matter (CNM) effects present at the initial state of heavy-ion collisions. Deep Inelastic Scattering (DIS) experiments have shown that Parton Distribution Functions (PDFs) of free protons are different from the ones of protons bound in nuclei. The CNM effects can be studied in p–Pb collisions where part of them are present and where the conditions of energy density and temperature dot

not allow the formation of the Quark-Gluon Plasma.

The aim of this thesis is to measure the π^0 meson production in proton-lead (p–Pb) collisions at $\sqrt{s_{\rm NN}}$ = 5.02 TeV in order to disentangle initial- from final-state effects in the π^0 meson suppression observed in highly central events in Pb–Pb collisions. Moreover, the work of this thesis provides an additional method to the existing ones in ALICE for the π^0 meson detection. This method reconstructs the π^0 meson in its Dalitz decay channel ($\pi^0 \rightarrow e^- e^+ \gamma$). For consistency check, the π^0 meson production in pp collisions at $\sqrt{s}$ = 2.76 TeV and $\sqrt{s}$ = 7 TeV were measured using the method developed in this thesis and compared to that obtained by measuring the π^0 in the 2γ channel. The measurement of π^0 meson in pp and p–Pb collisions serves as a test for pQCD model calculations and Color-Glass Condensate predictions and it can also give new constrains for these models.

This document is organized as follows: Chapter 1 includes a brief description of the standard model, Quantum Chromodynamics, the Quark-Gluon Plasma and Heavy-Ion collisions. Chapter 2 presents the properties of the π^0 meson which are used for its reconstruction. Chapter 3 concerns the description of the LHC, the ALICE experimental setup and the software for the reconstruction, simulation and analysis of the data. Chapter 4 is devoted to describe the data sample used in this thesis and to describe the reconstruction of the π^0 Dalitz decay products as virtual photon and photon. The π^0 signal extraction and the calculation of the systematic errors will be described in chapter 5. In chapter 6 the measured invariant π^0 meson yields in pp collisions at $\sqrt{s}$ = 2.76 TeV and $\sqrt{s}$ = 7 TeV and in p–Pb collisions at $\sqrt{s_{\rm NN}}$ = 5.02 TeV as well as the nuclear modification ($R^{\pi^0}_{\rm pPb}$) factor will be presented and compared to model calculations. Finally, a summary and outlook is given in chapter 7.

Chapter 1

Physics Theory

1.1 The Standard Model

The Standard Model of particle physics is the theory that describes the matter that forms the Universe and their interactions [1, 2]. A schematic description of it can be seen in Fig. 1.1. The Standard Model includes two classes of fundamental particles [3]: fermions and bosons. Fermions are the main ingredients of matter. Elementary fermions (quarks and leptons) have spin 1/2 and are grouped into three generations. Each of these generations includes two quarks and two leptons. The lightest and most stable fermions belong to the first generation. Particles from this generation play an important role in the Universe composition, since all stable matter is composed of them [4]. Each subsequent generation contains more unstable and heavier particles than the previous one. Except neutrinos, all particles belonging to the second and the third generation have a very short lifetime. On the other hand, bosons are the mediators of the fundamental forces: electromagnetic, weak and strong. Bosons have an integer spin and do not follow the Pauli exclusion principle[1] as fermions do. The boson that mediates the electromagnetic force is called photon, a massless particle with electric charge zero. The weak interaction is mediated by the bosons W^+, W^-, and Z. All of them are massive particles; being Z boson the heaviest. The Higgs mechanism is the responsible for the mass of bosons and fermions [5–7]. The particle predicted in such mechanism is called the Higgs Boson and it was discovered in 2012 by the LHC experiments: CMS [8] and ATLAS [9]. The force carrier of the strong interaction is a massless particle with color charge named gluon. The consequence of the color charge property of gluon is that it also experiments the strong force, and therefore, it can interact with itself.

Quarks experience the strong, weak and electromagnetic forces. However, quarks have never been observed free in nature. They are bound colorless states, hadrons. There are two types of hadrons: baryons and mesons. Mesons are composed by a quark and an anti-quark ($q\bar{q}$) and baryons are composed by three quarks (qqq). Protons and neutrons are an example of baryons. Furthermore, leptons experiment weak and electromagnetic forces (except neutrinos that are not affected by the electromagnetic force).

[1] The Pauli exclusion principle was postulated by Wolfgang Pauli in 1925 and it asserts that two fermions with identical quantum numbers cannot be at the same time in the same quantum state.

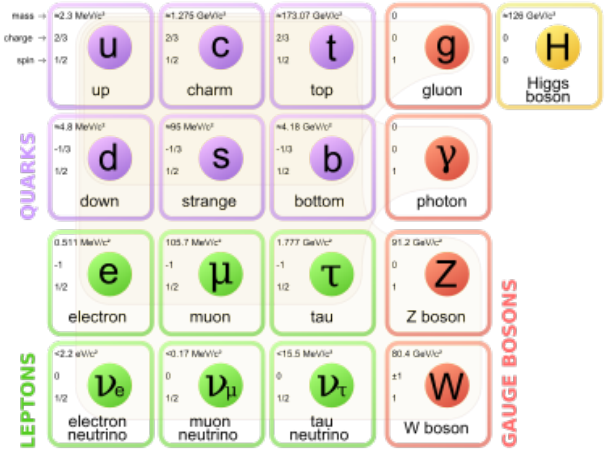

Figure 1.1: Schematic description of the standard model with the three generations of matter, the gauge bosons in the fourth column and the Higgs boson in the fifth. Plot taken from [11].

1.2 Quantum Chromodynamics

Quantum Chromodynamics (QCD) is the theory that describes the strong interaction between the elementary constituents of matter. A detailed description of QCD can be found in [3]. In an analogy to the Quantum Electrodynamics (QED), where its name refers to the electric charge, the name of QCD refers to color charge, which is an important characteristic of the strongly interacting particles. QCD is the SU(3) component of the SU(3)×SU(2)×U(1) and its dynamics are given by the Lagrangian of QCD [3]:

$$\mathcal{L} = \sum_q \bar{\psi}_{q,a} \left(i\gamma^\mu \partial_\mu \delta_{ab} - g_s \gamma^\mu t^C_{ab} \mathcal{A}^C_\mu - m_q \delta_{ab} \right) \psi_{q,b} - \frac{1}{4} F^A_{\mu\nu} F^{A\mu\nu} \tag{1.1}$$

where γ^μ are the Dirac γ-matrices, $\psi_{q,a}$ are quark-field spinors with q and a representing the index of the six quark flavors (up, down, strange, charm, top, and bottom) and the three color charges (blue, green and red), respectively. The m_q represents the quarks masses. The $\mathcal{A}^C_\mu$ are the gluon fields with C corresponding to the index of the eight type of gluons. The t^C_{ab} corresponds to eight 3×3 matrices, which are the generators of the SU(3) group. The parameter $g_s = \sqrt{4\pi\alpha_s}$ is the QCD coupling constant. The gluon field tensor $F^A_{\mu\nu}$ is defined as:

$$F^A_{\mu\nu} = \partial_\mu \mathcal{A}^A_\nu - \partial_\nu \mathcal{A}^A_\mu - g_s f_{ABC} \mathcal{A}^B_\mu \mathcal{A}^C_\nu \qquad [t^A, t^B] = i f_{ABC} t^C \tag{1.2}$$

Although QCD is similar to QED, there are two important differences between them: their force carrier and their coupling constant. In contrast to the force carrier of QED (photon), which is electrically neutral, the force carrier of QCD (gluon) is a color charge particle. This means that gluons can interact with themselves; making QCD a more complex theory. On the other hand, the coupling constant (α_s) of QCD is various orders of magnitude larger than the one of QED ($\alpha = e^2/\hbar c = 1/137$) and shows a strong dependence to the momentum transferred in an interaction (Q^2). The α_s of QCD is thus a running-coupling constant. Its leading-order for larger momentum transfer can be expressed as [12]:

$$\alpha_s(Q^2) = \frac{4\pi}{\beta_0 ln(Q^2/\Lambda^2)} \tag{1.3}$$

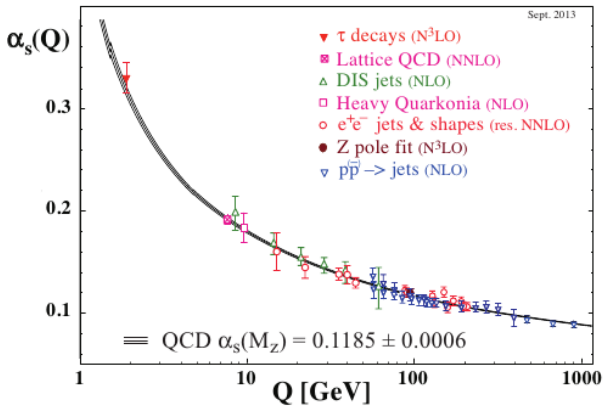

Figure 1.2: Summary of measurements of α_s as a function of the energy scale Q [3].

where Λ is the QCD scale, however, it can only be determined experimentally or by lattice calculations and its value is $\Lambda \approx 200$ MeV [13]. The distribution of α_s as function of Q^2 is shown in Fig. 1.2. An inverse dependence of α_s with the momentum transfer is observed. The consequence, is that at lower values of Q^2, α becomes large enough that the perturbative models developed for QED cannot be used to describe the strong interaction. Instead, lattice QCD calculations are used in this regime of energy. On the other hand, at larger values of Q^2, particles interact weakly enough that their dynamics can be described by perturbative QCD models (pQCD) assuming that they behave as quasi free particles. The value of α_s in which the strong interaction can be described by pQCD model calculations is normally measured at the scale of the Z boson mass (M_z) and its average value until now is $\alpha_s(M_z) = 0.1185 \pm 0.0006$ [3].

In addition to the above, one should mention that QCD has three implicit properties [14]: confinement, asymptotic freedom and infrared safety. In order to illustrate better the confinement property one should introduce the strong-interaction potential:

$$V(r) = -\frac{4}{3}\frac{\alpha_s}{r} + kr \tag{1.4}$$

where α_s is the QCD coupling constant and r is the radial distance between quarks. At small values of r (small distances) the first term of the potential is dominant and it is similar to the Coulomb potential. Moreover, one can see a linear dependence between the potential and r. This means that for longer distances the potential becomes so strong that quarks cannot be separated. Besides, if the energy of the potential becomes larger than the energy needed for $q\bar{q}$-pair production, a new meson will be produced [12, 15]. The above phenomenon is known as $confinement$ and it is the reason why quarks and gluons have never be observed as a free particles in the nature.

On the other hand, $asymptotic\ freedom$ is the phenomenon that at short distances or larger values of transfer momentum, the coupling constant becomes weaker enough that quarks and gluons behave as quasi-free particles. This phenomenon was discovered in 1974 by Frank Wilczek and David Gross [16], and by David Politzer [17]. They were awarded the Nobel Prize in 2004 for this achievement.

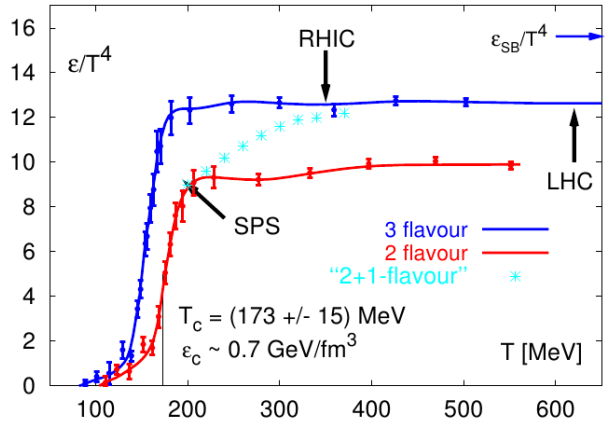

Figure 1.3: Scaled energy density (ϵ/T^4) as a function of the temperature (T) of the hadronic matter obtained from lattice calculations for two massless quarks and three massless quarks. The energy density expected for a strange quark mass is labeled as "2+1-flavour". Calculations using real quark masses show a lower critical temperature [18–21]. Figure taken from [22].

Finally, the $infrared\ safety$ refers to the fact that the quantities like hard-scattering cross sections observed in the short distances regime of the strong interaction theory do not depend of the light quark and gluon masses, which means that they are "safe" from the infrared divergences present in the long distances regime of QCD, and therefore, they can be determined by pQCD model calculations [14].

1.3 The Quark-Gluon Plasma

After the postulation of the asymptotic freedom, the idea that at extreme conditions of temperature or energy density the hadronic matter undergoes a phase where it dissolves into its constituents (quarks and gluons), came out [23]. This phase of the matter was named as Quark-Gluon Plasma (QGP) in analogy to the electromagnetic plasma where ions and electrons are dissociated [18]. The QGP is believed to have existed shortly after the big bang and it may exists in the nucleus of very dense stellar objects like neutron stars.

The critical temperature (T_c) and the critical energy density (ϵ_c) for the phase transition between hadronic matter to the deconfined state have been studied for many years and the values given by lattice calculations until now are $T_c = 173 \pm 15$ MeV and $\epsilon_c \sim 0.7$ GeV/fm^3 [3] (see Fig. 1.3).

Figure 1.3 shows that the scaled energy density (ϵ/T^4) rapidly increases above the critical temperature ($T > T_c$). This behaviour may be due to the phase transition between hadronic matter to deconfined state of gluons and quarks. It is also observed that ϵ is proportional to T^4 for T above T_c, which is an expected behaviour for an ideal gas. However, the proportional factor is below to the Sfefan-Boltzmann constant [18] (the limit for an ideal gas of gluons and massless u, d and s quarks). This means that quarks and gluons interact in the QGP.

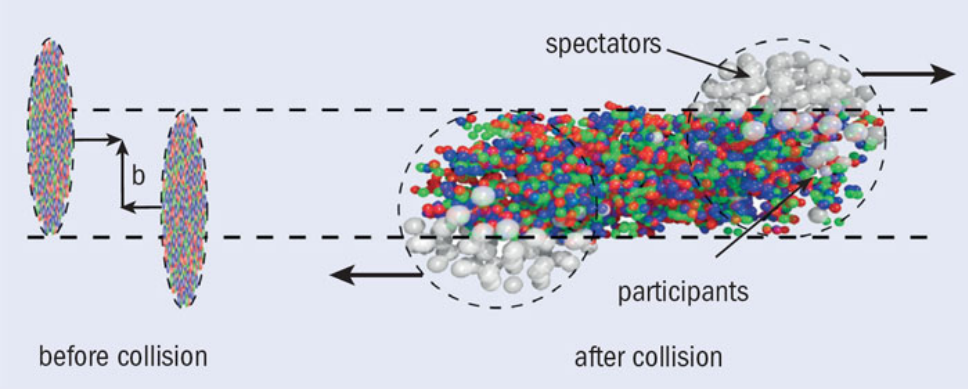

Figure 1.4: Illustration of a heavy-ion collision. Figure taken from [24]

The only way to study the properties of the QGP in a laboratory is by ultrarelativistic heavy-ion collisions, where the conditions of high temperature and/or high energy density are expected to occur [18]. A description of some signatures of the Quark-Gluon Plasma is given in section 1.5.

1.4 Heavy-Ion Collisions

Ultrarelativistic heavy-ion collisions allows to study the properties of the QGP in the laboratory. The collision between two heavy nuclei is illustrated in Fig. 1.4. As the two heavy nuclei travel with a velocity close to the speed of light, they are Lorentz contracted in the laboratory frame; resembling as two thin plates. In the overlapping region of the crossing path, nucleons of the two heavy nuclei collide hitting the matter at a temperature above T_c forming the QGP. The nucleons that participate in the collision are called participants and the nucleons that do not collide are called spectators. The spectators may continue their trajectory without being affected by the collision.

The geometry of the overlapping region is called “centrality” and it is determined by the impact parameter "b" which is defined as the distance between the two centers of the colliding nuclei in the transverse plane (see Fig. 1.4). Experimentally, the impact parameter cannot be directly measured. However, as the total transverse energy of the produced particles and the particle multiplicity is proportional to the number of participants (N_{part}) and the number of binary collisions (N_{coll}), the impact parameter can be estimated using a Glauber model [25]. The centrality is commonly expressed in percentage; with < 10 % for the most central collisions and > 70 % for the most peripheral collision. The Quark-Gluon Plasma is more likely to occur in highly central collisions where the highest temperature is reached.

The knowledge of the different stages of a heavy-ion collision is important in order to give any interpretation of the properties observed at the final state. Normally the stages are defined as "pre-equilibrium", "thermal-equilibrium", "hadron gas" and "freeze-out". Figure 1.5 shows the space-time evolution of a heavy-ion collision and the stages are briefly described below:

- pre-equilibrium: The first interactions between the two ultrarelativistic Lorentz-contracted heavy nuclei take place at $\tau = 0$ fm/c. Hard scattering interactions where hard partons are produced are dominant here. Subsequently, the particles produced in the volume

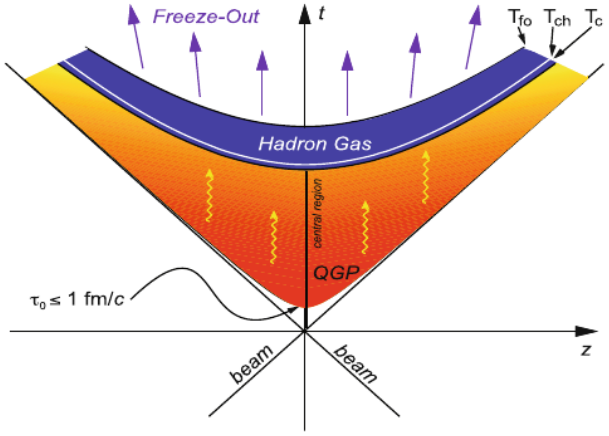

Figure 1.5: Evolution of heavy-ion collisions. Figure taken from [27].

interact. This leads to a fast increase of the energy density that the system will thermalise forming the Quark-Gluon Plasma. This stage is normally known as "pre-equilibrium". The initial conditions may be described by the Color Glass Condensate (CGC) framework [26]. The time that takes to form the QGP is expected to be $\tau_0 \approx 1$ fm/c, so that the further evolution of the system can be described by hydrodynamical models. However, the fast thermalization of the system is still not fully understood [18].

- thermal-equilibrium: At certain moment ($\tau > \tau_0$) the system will reach an thermal-equilibrium and due to the high energy density and high gradient pressure it will rapidly expand and cool down. The evolution of the system in this stage is well described by hydrodynamical models.

- hadron gas: During the expansion, the system will eventually be diluted into a hadron gas at temperatures below T_c. As the energy density decreases gradually, a mixed phase between the deconfined state of hadronic matter and the hadron gas is expected.

- freeze-out: As the energy density will be very low at $T = T_{ch}$, the inelastic collisions do not take place anymore. Therefore, the composition of the particle abundances will not change. The above is known as chemical freeze-out. With further expansion of the system, the energy density becomes much smaller at $T = T_{fo}$, when the elastic collisions will end. Therefore, the kinematic properties of the particles will not change. The above is known as thermal freeze-out. Finally the particles will travel in the vacuum and if they are inside the acceptance they can be measured by the experimental aparatus.

1.5 The signatures of the Quark-Gluon Plasma

The Quark-Gluon Plasma phase formed in collisions between two ultrarelativistic heavy-ions has a short lifetime, which cannot be detected directly by the experiments.
Instead, the only way to proof its existence and study its properties is by looking at the characteristics of the bulk of particles that emerge from the final-state of the collision. However, there is no unique signature of the QGP formation. Moreover, in order to describe the phenomenology of the QGP in terms of thermodynamics and hydrodynamics, the hot and dense medium

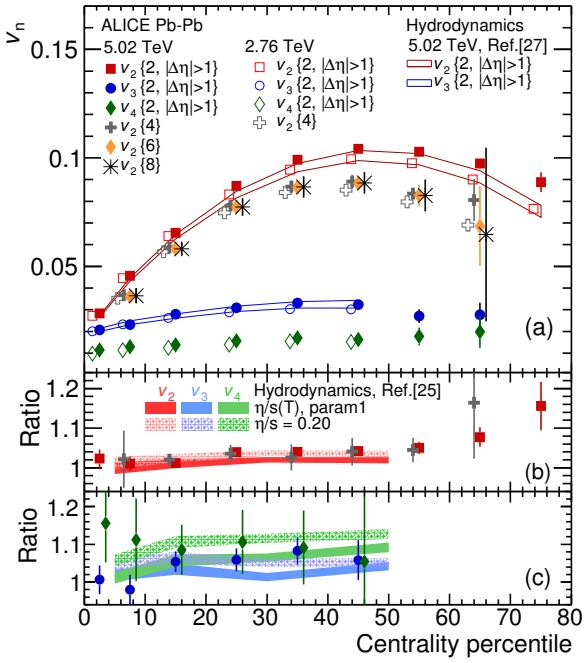

Figure 1.6: (a) Results of anysotropy flow (v_n) reported by ALICE in Pb–Pb collisions at $\sqrt{s_{\rm NN}}$ = 2.76 TeV and at $\sqrt{s_{\rm NN}}$ = 5.02 TeV [33] presented in $p_{\rm T}$ as a function of centrality. The ratio between $v_2\{2, |\Delta\eta| > 1\}$ (red) and $v_2\{4\}$ (gray) and the ratio between $v_3\{2, |\Delta\eta| > 1\}$ (blue) and $v_4\{2, |\Delta\eta| > 1\}$ (green) for Pb–Pb collisions at $\sqrt{s_{\rm NN}}$ = 5.02 TeV and $\sqrt{s_{\rm NN}}$ = 2.76 TeV, respectively, are shown in panels (b) and (c). The figure also includes comparison to hydrodynamic model calculations.

has to reach a local equilibrium [28]. This means that it has to behave as matter and not as an assembly of thousands of particles [28]. Moreover, the system has to be as long as possible in local equilibrium so that one can extract the quantities needed (temperature, energy, pressure, entropy density) for its description.

There are many aspects of the hot and dense hadronic matter that have been studied for 20 years. Results obtained by the RHIC [29] and by the LHC [30–32] experiments have revealed that the evolution of QGP is well described by hydrodynamical models if one assumes a very low value of viscosity (the lower value ever measured). For this reason, the QGP is believed to be closely to an ideal liquid [20, 28]. In the following subsections some QGP signatures will be described.

1.5.1 Collective Flow

The study of the properties (transverse momentum, azimuthal distribution, etc.,), in a collective way, of the produced particles in a collision between two heavy nuclei can give us information of the different phases of Quark-Gluon Plasma. The phenomenological description of this properties are known as flow [12]. There are three types of flow: radial flow, elliptic flow and directed flow. The radial flow is produced in highly central events and the emission of the produced particles is expected to be distributed isotropically in the plane transverse to the beam direction. The elliptic flow is produced in non-central events and due to the fact that the shape of the

overlapping region of the two colliding nuclei describes an elliptic form, an anysotropy can be observed in the azimuthal distribution of the produced particles in the transverse plane. The directed flow receives its name because the emission of the produced particles has a direction. The distribution of particles can be described by a Fourier form [34]:

$$E\frac{\mathrm{d}^3N}{\mathrm{d}^3p} = \frac{1}{2\pi}\frac{\mathrm{d}^2N}{p_{\mathrm{T}}\mathrm{d}p_{\mathrm{T}}\mathrm{d}y}\left(1 + 2\sum_{i=1}^{\infty} v_n(p_{\mathrm{T}}, y)\cos[n(\phi - \Psi_R)]\right) \tag{1.5}$$

where Ψ corresponds to position of the reaction plane which is defined by the impact parameter and the axes parallel to the beam direction (z) [35].
The coefficients of v_n are obtained as the average values:

$$v_n(p_{\mathrm{T}}, y) = \langle\cos[n(\phi - \Psi_R)]\rangle \tag{1.6}$$

The coefficient v_1 corresponds to the directed flow and the coefficient v_2 corresponds to the elliptic flow. The most abundant flow is the elliptic flow and, at the same time, the most interesting due to its sensibility to the early stages of the QGP [12, 36]. A collection of the different coefficients measured by ALICE in Pb–Pb collisions at $\sqrt{s_{\mathrm{NN}}}$ = 2.76 TeV and at $\sqrt{s_{\mathrm{NN}}}$ = 5.02 TeV are shown in Fig. 1.6 [33]. Hydrodynamical models describe the measured values.

1.5.2 Jet Quenching and Nuclear Modification Factor

High energy partons, commonly named as hard partons, are produced in hard scattering processes that may occur in high energy hadron colliders like the LHC. The term parton is the collective name for quarks and gluons in the parton model proposed by Richard Feynman in 1969 [37]. The produced hard partons fragment into new quarks and gluons. The fragments produce a shower of particles, called jets, when they combine during the hadronization process. In heavy-ion collisions, hard partons are produced before the creation of the QGP; therefore they propagate through a hot and dense medium before they fragment and form hadrons. During the propagation, hard partons interact with the components of the QGP and can lose energy. The two main meachisms of energy loss of a particle crossing the QGP are known as [38] collisional energy loss (by elastic scatterings) and radiative energy loss (by inelastic scatterings). The dominant mechanism of hard parton energy loss when they cross the QGP is the radiative one. Multiple interactions of partons with the medium induce to an increament of gluon radiation (gluon-strahlung[1]) that lead to an energy loss of the most energetic partons [39]. As high energy partons are the main source of high-p_{T} hadrons [40], a hadron suppression will be observed, specially above 2 GeV [41]. This phenomenon is called “jet quenching” and was first observed at RHIC [42, 43].

As the production of hard partons is expected to scale as the number of binary collisions of nucleons, the effect of the jet quenching can be studied with the nuclear modification factor (R_{AA}), which is defined as:

$$R_{\mathrm{AA}}(p_{\mathrm{T}}) = \frac{\mathrm{d}^2N/\mathrm{d}p_{\mathrm{T}}\mathrm{d}y|_{\mathrm{AA}}}{\langle T_{\mathrm{AA}}\rangle \cdot \mathrm{d}^2\sigma/\mathrm{d}p_{\mathrm{T}}\mathrm{d}y|_{\mathrm{pp}}} \tag{1.7}$$

[1] In analogy with the radiation of photons by electrons in EM in QED known as breemstrahlung, the radiation of gluons by partons in QCD is known gluon-strahlung

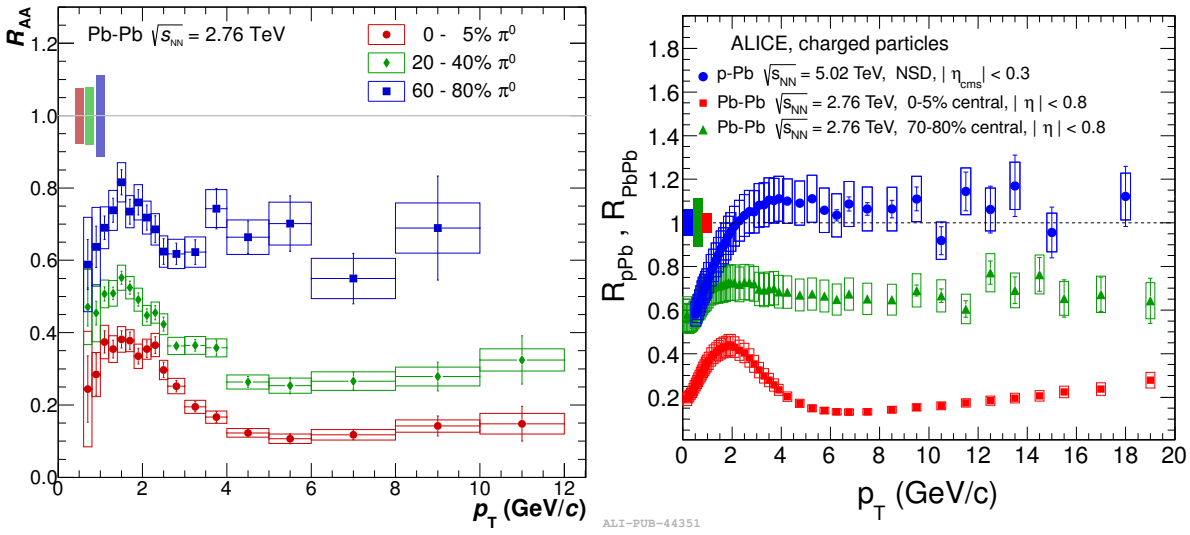

Figure 1.7: Nuclear modification factor of π^0 mesons in Pb–Pb collisions at $\sqrt{s_{\rm NN}}$ = 2.76 TeV for different centralities [44] (left). Nuclear modification factor of charged particles in Pb–Pb collisions at $\sqrt{s_{\rm NN}}$ = 2.76 TeV and in p–Pb collisions at $\sqrt{s_{\rm NN}}$ = 5.02 TeV [45] (right).

where $\langle T_{\rm AA}\rangle = \langle N_{\rm coll}\rangle/\sigma^{\rm pp}_{\rm inel}$ with $\langle N_{\rm coll}\rangle$ as the average of inelastic binary collisions estimated using a Glabuer model [25]. If there is no nuclear effect, the nuclear modification factor resulting from the comparison between the yields produced in pp collisions and the yields produced in Pb–Pb should be equal to unity.

The measurement of the π^0 production in pp collisions and Pb–Pb collisions reported by ALICE [44] (see left panel of Fig. 1.7), shows a clear suppression of the π^0 at energies above 2 GeV in Pb–Pb collisions. The suppression reaches values up to 8-10 for $5 \lesssim p_{\rm T} \lesssim 7$ GeV for most central events. A similar behaviour is observed in the $R_{\rm AA}$ for charged particles (see right panel of Fig. 1.7). The above could be an indication of the creation of the QGP. However, in order to give any conclusion from the observed results, one should discard that the suppression is not due to the initial-state effects of cold nuclear matter.

The initial-state effects can be studied in p–Pb collisions because the conditions needed for the formation of QGP are not expected to occur. Therefore, the hadron production at high-$p_{\rm T}$ will only be affected by the initial conditions of the collision. The nuclear modification factor ($R_{\rm pPb}$) for charged particles is shown in right panel of Fig. 1.7. One can see that there is no suppression for transverse momenta above 2 GeV. A similar behaviour is expected for the $R^{\pi^0}_{\rm pPb}$ of the π^0 and this is one of the subjects of this thesis. The initial-state effects are commonly named as cold nuclear matter (CNM) effects and they will be briefly described in section 1.6.

1.5.3 Quarkonia suppression

Quarkonia is the name received by bound states ($q\bar{q}$) of heavy quarks like J/ψ, ψ, etc. As quarkonia states are only produced at the initial stages of heavy-ion collisions (because their larger masses prevent them to be formed in the thermal phase of the QGP), they have to travel through the QGP. As a consequence, quarkonia are expected to melt into the hot and dense matter (depending on the temperature of the medium) due to the color screening effect which weakens their potential [46]. Moreover, as quarkonia states have different binding energies

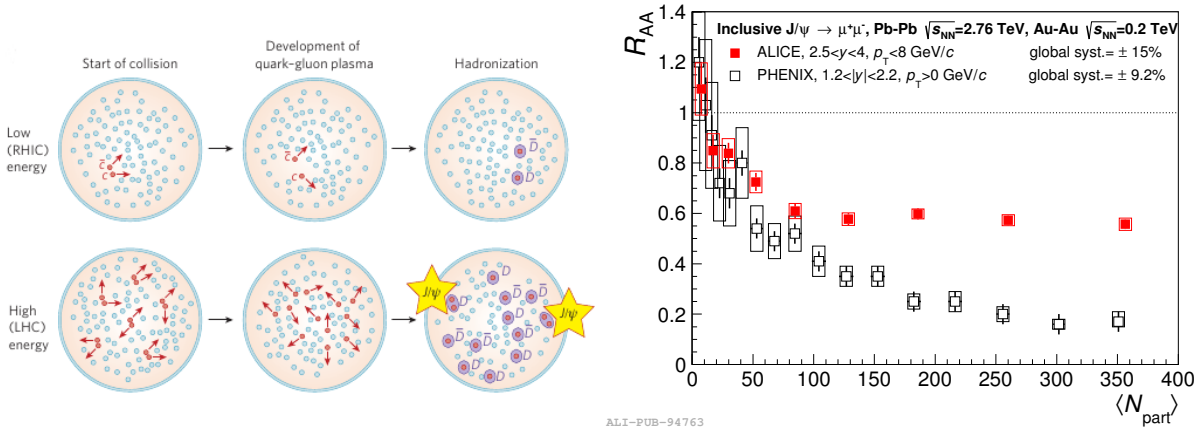

Figure 1.8: (Left) Plot adapted from [28] that illustrates the charmonium suppression. At low energy the produced quark and anti-quark are combined with other quarks to form a D meson. At high energy many quarks and anti-quarks are produced and they recombine at the hadronization process to form a charmonium state. (Right) Nuclear modification factor (R_{AA}) of inclusive J/ψ as a function of number of participants ($\mathrm{N_{part}}$) measured by ALICE [52] in Pb–Pb collisions at $\sqrt{s_{\mathrm{NN}}}$ = 2.76 TeV compared to one measured by PHENIX [49] in Au-Au collisions at $\sqrt{s_{\mathrm{NN}}}$ = 200 GeV. Right plot taken from [51].

they would melt at different temperatures [47]. For this reason, the quarkonia suppression was proposed as an important signature of the deconfined state of hadronic matter [46] and as an important quantity to study the thermal properties of the QGP [47].

Quarkonia suppression has already been observed in results obtained by the SPS and RHIC experiments. However, the suppression observed in both experiments was of the same order in spite of their large difference in energy [48, 49]. The above leads to the idea of the regeneration [50]. The regeneration can be described as the combination of two independent charm quarks (created at the initial stages of the collision) that form a quarkonia state in the hadronization process (see left side of Fig. 1.8). This phenomenon is expected to increase quadratically with respect to number of $\mathrm{c\bar{c}}$-pairs produced at the initial stages [28]. As at the energies of the LHC, a significant increase of $\mathrm{c\bar{c}}$-pairs production at the initial stages is expected, an enhancement instead of a suppression of the quarkonia production should be observed [28]. These behaviour, has indeed been measured by ALICE [51] (see right side of Fig. 1.8).

1.6 Cold nuclear matter effects

In order to give a definitive interpretation of the quantities observed in Pb–Pb collisions as the jet quenching, J/ψ suppression, etc., the initial conditions of the Pb–Pb collisions have to be well understood. As it was mentioned previously, those conditions can be studied in p–Pb collisions since the hot and dense medium is not expected to be created. Commonly, those conditions are called as cold nuclear matter effects. In this section a brief description of this conditions will be given.

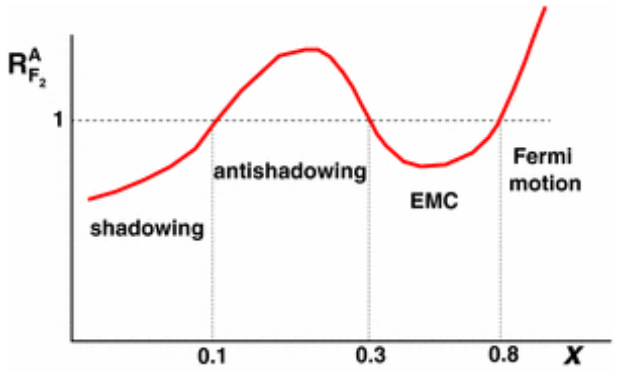

Figure 1.9: Ratio of the nuclear structure functions for a fixed Q^2 as a function of the momentum fraction x. Plot taken from [57]

1.6.1 Cronin effect

In 1970, results from the study of the hadron production in pp collisions and in p-nucleus (p-A) collisions, showed that the invariant hadron cross sections in p-A relative to that in pp collisions, not only scales as the number of binary collisions, but also they show a strong dependence to the atomic nuclei (A) for intermediate transverse momenta [53, 54]. In this study, the invariant cross section dependence with A was parametrized as [53]:

$$\frac{\mathrm{E}\mathrm{d}\sigma}{\mathrm{d}^3p}(p_{\mathrm{T}}, A) = \frac{\mathrm{E}\mathrm{d}\sigma}{\mathrm{d}^3p}(p_{\mathrm{T}}, 1)A^{\alpha} \tag{1.8}$$

They found that $\alpha > 1$ for transverse momenta above 2 GeV/c. This means that an enhancement of the hadron production is expected in that region of p_{T}. This phenomenon is called Cronin effect and it is explained in terms of multiple scattering of the incoming partons when they propagate through the target nucleus [55].

1.6.2 Shadowing, anti-shadowing and EMC effect

It is well known that the nuclear structure functions of free nucleons (F_2^{nucleon}) differs from those of nucleons bound in a nucleus (F_2^A). The above was discovered by the EMC experiment when compared the nuclear structure function of nucleons bound in nuclei with those nucleons of deuterium. The deuterium was used in this study because it is the best approximation to the structure function of a free nucleon [56]. The behaviour of the nuclear distribution function can be observed in the $R^A_{F_2}$ which is defined as[57]:

$$R^A_{F_2}(x, Q^2) = F_2^A(x, Q^2)/AF_2^{nucleon}(x, Q^2) \tag{1.9}$$

where A is atomic number.
The effects are normally classified in different regions of x [56, 57] as it is shown in Fig. 1.9:

- $x > 0.8$ is called the fermion motion.
- $0.1 - 0.2 < x < .8$ the behaviour is this region is called "EMC" effect.
- $x \approx 0.1 - 0.2$ is called anti-shadowing.
- $x < 0.05 - 0.1$ this phenomenon is called shadowing.

1.6.3 Color-Glass Condensate

The structure of protons has been studied in Deep Inelastic Scattering experiments (DIS) for many years. One important observation by DIS experiments was that the number of quarks and gluons inside a nucleon grows rapidly when increasing the high energy resolution. An illustration of this can be seen in Fig. 1.10.

The enhancement of the parton density at high energy interactions is due to the Lorentz contraction of nucleons when traveling to velocities close to the speed of light [26]. One should remember that nucleons are composed by three valence quarks bound by gluons. The valence quarks eventually fluctuate into new gluons and q-$\bar{\text{q}}$ pairs. In a low energy interaction, only few on these extra gluons and quarks are visible because of their short life and because they do not affect the reaction [26]. Contrary, in high energy collisions, the Lorentz contraction of nucleons not only modifies the geometry of the nucleon, but it also increases the lifetime of these fluctuations making them visible.

Another important discovery by DIS experiments is that at small values of the Bjorken variable x (which corresponds for high energy interactions to $x \equiv p_x/\sqrt{s}$) the parton content of protons is dominant by gluons as the valence quarks are negligible at these scales and the sea quarks are suppressed by the weak coupling constant [26]. Consequently, the gluon density increases at lower values of x and at larger values of Q^2.

The continuous increasing of gluon density at lower values of x is expected to suturate at a certain point because low energy gluons start to recombine to form more energetic ones. This leads to a more difficult description of the processes using the perturbative regimen of QCD although the weak coupling constant ($\alpha_s \ll 1$).

Strongly interacting systems with high parton densities $\alpha_s \ll 1$ are considered as non-perturbative in the QCD theory because of the number of processes involving multiple partons makes non-linear effects (which break down pQCD) more important. The scale in which the non-linear effects becomes important is known as saturation scale (Q_s). Consequently, process with a $p_{\mathrm{T}} \ll Q_s$ can be affected by the gluon saturation regime. The Color-Glass Condensate (CGC) [26] is a theory that provides a description of the process below the saturation scale.

The saturation scale depends on the x and on the nucleon thickness $Q_x \sim A^{1/3}$ [26]. Therefore, the gluon saturation effects are expected to be present in Pb–Pb and p–Pb collisions at the LHC energies and this can lead to an additional suppression on the hadron production at high p_{T}.

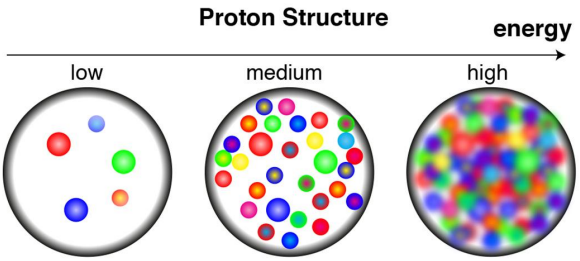

Figure 1.10: Illustration of the parton density of protons at different energy resolutions. Plot taken from [58].

Chapter 2

The π^0 meson

The measurement of π^0 mesons is very important in order to cross check predictions from model calculations at low p_{T} and cross check pQCD NLO predictions at high p_{T}. They are also necessary for the measurement of direct photons because they are the main source of background of decay photons. The π^0 meson is one of the three types of pions: π^+, π^- and π^0. It decays via the electromagnetic force. Its main properties and its two main decay modes into two photons (2γ) and the Dalitz decay ($\mathrm{e}^+\mathrm{e}^-\gamma$) are given in Tab. 2.1.

Symbol	**Quark content**	**Rest mass (MeV/c^2)**	**I^G**	**J^{PC}**	**Mean lifetime(s)**	**Decay modes**	
						Mode	**Branching ratio**
π^0	$\frac{u\bar{u}-d\bar{d}}{\sqrt{2}}$	134.9766 ± 0.0006	1^-	$0^\pm$	8.52×10^{-17}	2γ	(98.823 ± 0.034) %
						$\mathrm{e}^+\mathrm{e}^-\gamma$	(1.174 ± 0.035) %

Table 2.1: Properties of the π^0 meson and the two main π^0 meson decay modes with the corresponding branching ratios. The values were obtained from [3].

A compilation of π^0 measurements is shown in Fig. 2.1. The spectra shows a clear power law behaviour at high p_{T}, with a power increasing as the energy increases. The ALICE measurements that are a combination of the photon conversion method and calorimeters show the largest p_{T} coverage. Moreover, the π^0 measurements in pp collisions are necessary in order to extract medium effects in Pb–Pb and in p–Pb collisions. π^0 suppression has been measured in central Au-Au (Pb–Pb) collisions at many different energies. Figure 2.2 shows a compilation of R_{AA} from $\sqrt{s_{\mathrm{NN}}}$ = 17.3 GeV to $\sqrt{s_{\mathrm{NN}}}$ = 2.76 TeV.

2.1 The Dalitz decay

In this thesis, the π^0 meson is reconstructed through its Dalitz decay mode. The Feynman diagrams of π^0 Dalitz and 2γ decay modes are illustrated in Fig. 2.3. The dynamics of π^0 Dalitz decay can be described by the Vector Dominance Model (VDM). The VDM [66] was introduced in the 1960s by J. J. Sakurai to described photon-hadron interactions. In this model photons are defined as the combinations of vector mesons like ρ^0, ω, ϕ, etc., [67].

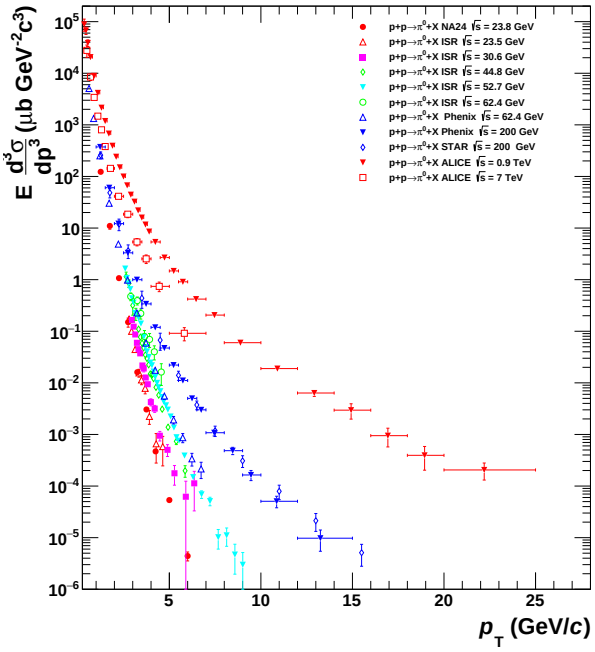

Figure 2.1: Collection of π^0 meson production in pp collisions at different center of mass energies [59–65].

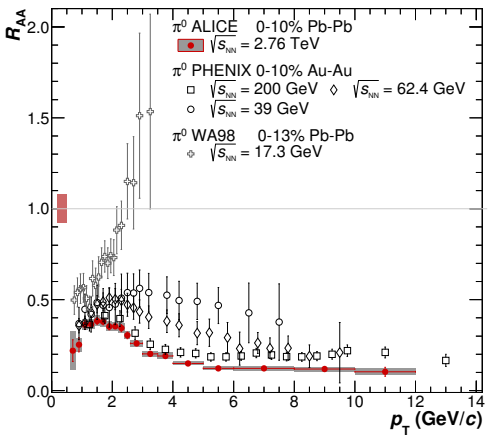

Figure 2.2: Collection of nuclear modification factors of π^0 meson in A-A collisions at different center of mass energies. Plot taken from [44].

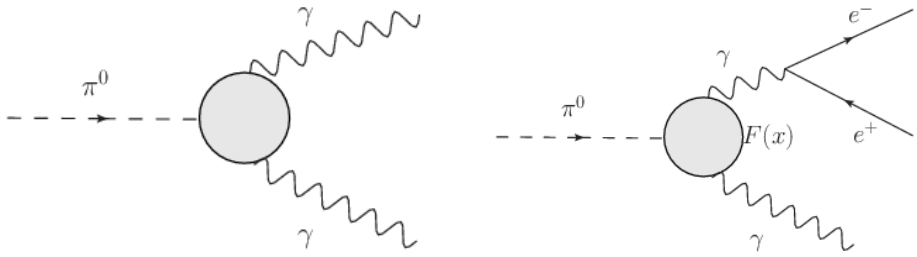

Figure 2.3: Leading order Feynman diagrams for the two most significant π^0 decay modes: 2γ (left) and $e^+e^-\gamma$ (Dalitz) (right).

The invariant mass distribution of the e^+e^- pairs from the π^0 Dalitz decay follows the Kroll-Wada QED formula [68] and at form factor:

$$\frac{d^2N_{e^+e^-}}{dM_{e^+e^-}} = \frac{2\alpha}{3\pi}\frac{1}{M_{e^+e^-}}\sqrt{1-\frac{4M_e^2}{M_{e^+e^-}^2}}(1+\frac{2M_e^2}{M_{e^+e^-}^2})(1-\frac{M_{e^+e^-}^2}{M_{\pi^0}^2})^3|F(M_{e^+e^-}^2)|^2 \tag{2.1}$$

where $M_{e^+e^-}$ is the invariant mass of the e^+e^- pairs, M_e is the electron mass, M_{π^0} is the π^0 mass and $F(M_{e^+e^-}^2)$ is the form factor defined as [69]:

$$F(M_{e^+e^-}^2) = \frac{1}{1-M_{e^+e^-}^2/\Lambda^2} \tag{2.2}$$

with $\Lambda^2 = 0.43 \pm 0.06$ GeV$/c^2$ [69]. For comparison, this parametrization and the invariant mass distribution $M_{e^+e^-}$ from π^0 Dalitz decays obtained in Monte Carlo simulations were superimposed, as it is shown in Fig. 2.4. A very good agreement is obtained for PYTHIA and PHOJET simulations in pp collisions (see Fig. 2.4a) as well as for HIJING p–Pb simulations (see Fig. 2.4b). On the other hand, π^0 Dalitz decays were not treated properly in DPMJET (see Fig. 2.4c) and it was therefore discarded in this analysis.

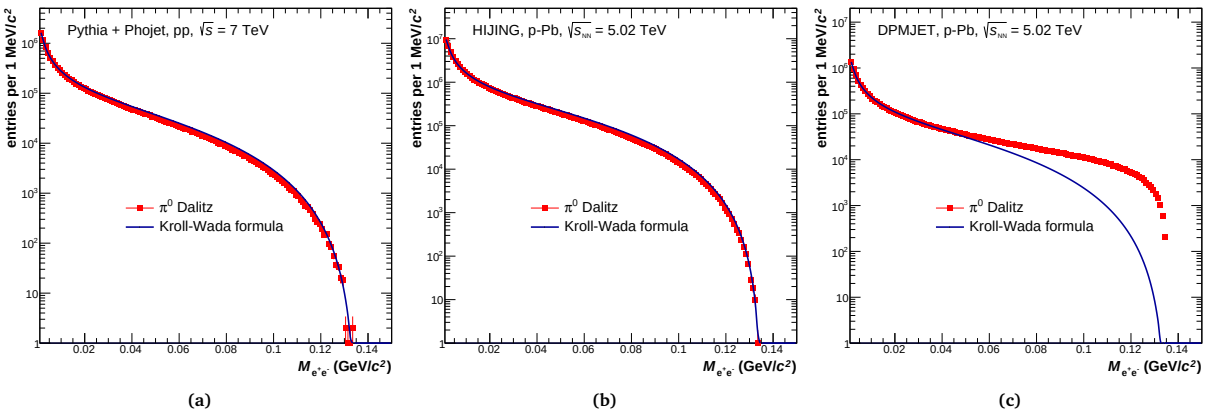

Figure 2.4: Invariant mass distribution $M_{e^+e^-}$ for π^0 Dalitz decays obtained in Monte Carlo simulations: (a) Pythia+Phojet, (b) HIJING and (c) DPMJET. The blue line is a parametrization of the Kroll-Wada formula with $\Lambda^2 = 0.43 \pm 0.06$ [69].

2.2 Relevance for the knowledge of the ALICE material budget

In order to establish the PCM method (see section 4.4) as valid for physics measurement, one of the main objetives of this thesis, it is essential to cross-check that the material thickness of the experiment and the photon reconstruction efficiency are known with a good precision. One possibility to do so is to compare the π^0 results when they are reconstructed in two different decay channels. The ratio of the two results can be written as:

$$\frac{\pi^0 \to \gamma\gamma \to e^+e^-e^+e^-}{\pi^0 \to e^+e^-\gamma \to e^+e^-e^+e^-} = \frac{BR(\gamma\gamma)}{BR(Dalitz)} \times \frac{Conv.Prob.^2 \cdot \epsilon_\gamma^2}{Conv.Prob. \cdot \epsilon_\gamma \cdot \epsilon_{e^+} \cdot \epsilon_{e^-}} \tag{2.3}$$

where ϵ correspond to the reconstruction efficiency of the γ and the e and $Conv.Prob$ represents the probability of one photon to convert into one electron-positron pair. From $Eq.$ (2.3) one can see that one error of the material budget of the 2-γ cancel with the corresponding one of the Dalitz channel. The results of these comparison will be presented in section section 6.1.1.

Chapter 3

Experimental setup

3.1 Large Hadron Collider (LHC)

The Large Hadron Collider (LHC) [70] at CERN is the biggest and the most powerful accelerator and particle collider ever built. It is installed in a circular tunnel of about 27 km of diameter located in the border between Switzerland and France, near Geneve. It was designed to accelerate protons (p) up to 7 TeV and lead ions (Pb) up to 2.76 TeV. Therefore, it is expected to afford, at its maximum capacity, pp and Pb–Pb collisions at $\sqrt{s}$ = 14 TeV and $\sqrt{s_{\rm NN}}$ = 5.5 TeV with a luminosity of $\mathcal{L} = 10^{34}\text{cm}^{-2}\text{s}^{-1}$ and $\mathcal{L} = 10^{27}\text{cm}^{-2}\text{s}^{-1}$, respectively. During the LHC Run1 (2009-2013) the machine performed pp collisions at $\sqrt{s}$ = 0.9, 2.36, 2.76, 7 and 8 TeV, and Pb–Pb collisions at $\sqrt{s_{\rm NN}}$ = 2.76 TeV, reaching half of its capacity. In addition, the LHC Run1 program also included p–Pb collisions at $\sqrt{s_{\rm NN}}$ = 5.02 TeV.

The LHC is equipped with two ultrahigh-vacuum ring-shaped beam pipes with an opposite magnetic field to accelerate and collide particles with the same electric charge. The bunch of particles are conducted through the accelerator by a strong magnetic field (8.33 T for 7 TeV [70]) provided by superconducting electromagnets. There are 1232 dipole magnets to bend the particles and 392 quadrupole magnets to focus the beams. The electromagnets consist of superconducting coils that should be kept at a temperature of -272.3 °C (colder than the outer space and close to absolute zero) to operate efficiently. Therefore, the LHC also includes a cryogenic system based on liquid helium to maintain the magnets at that very low temperature.

A schematic view of the LHC is shown in Fig. 3.1. The LHC is connected to an accelerator complex at CERN which provides the bunch of particles. The complex includes a set of sequentially-connected machines that sped-up particles up to a given energy before they are injected into the beam pipes of the LHC. The LHC tunnel has eight straight sections and eight arcs. At four of the straight sections are installed the biggest experiments of the LHC: ATLAS [71], CMS [72], LHCb [73] and ALICE [74]. The ATLAS and CMS experiments are devoted to study the physics of the higgs bosson, the LHCb experiment is dedicated to study the B-physics and the measurement of the CP violation and the ALICE experiment is optimized to study the physics of the QCD at high energies and densities and will be explained in more detail in section 3.2. In addition, there are also three smaller experiments at the LHC: MoEDal [76], TOTEM [75] and LHCf [77]. MoEDal is an experiment designed to search an hypothetical particle with only one magnet pole, TOTEM is a low luminosity experiment optimized to measure the proton-proton interaction cross section,

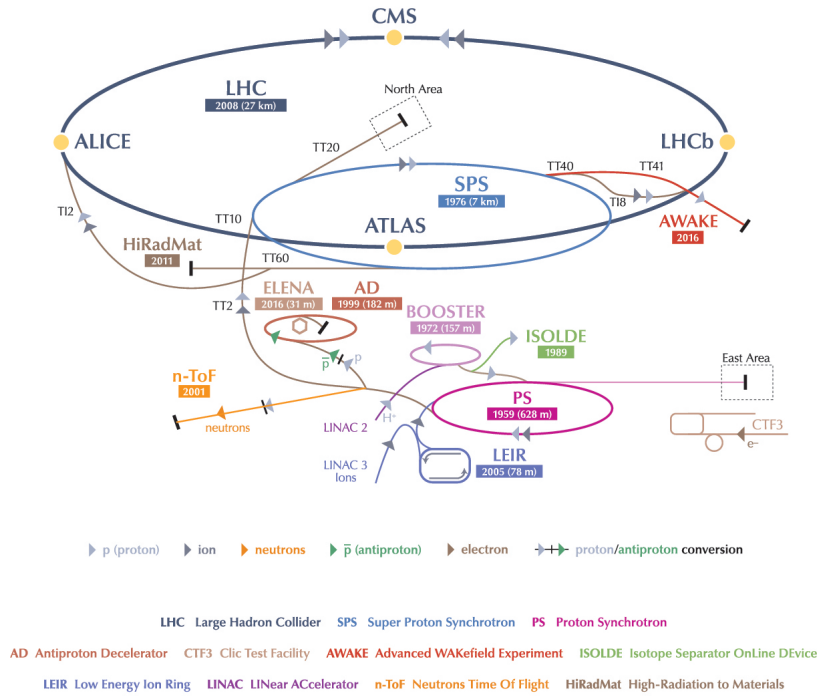

Figure 3.1: Illustration of the Large Hadron Collider (LHC) complex at CERN. Figure taken from [78].

and LHCf is the smallest experiment at the LHC designed to measure neutral-particle production cross sections in proton-proton and nucleus-nucleus collisions in very forward region in order to simulate cosmic rays.

The accelerator chain of the LHC starts with the creation of the protons or lead ions beams. Protons are obtained from hydrogen gas and lead ions from lead atoms[1]. Both sources are passed through an electric field to remove electrons. Next, the obtained bunch of particles are injected to the first accelerator in the chain. This can vary according to the type of beam. In the case of lead ions, the first two accelerators in the chain are the linear accelerator (LINAC 3) and the Low Energy Ion Ring (LEIR) which accelerate lead ions to 4.5 MeV and to 72 MeV per nucleon, respectively. On the other hand, the acceleration of protons begins with the linear accelerator (LINAC 2) which increases their energy to 50 MeV, followed by the Proton Synchrotron Booster (PSB) which accelerates them to 1.4 GeV. The subsequent steps are the same for both kind of beam particles. The bunch of protons (lead ions) are injected to the Proton Synchrotron (PS) to reach an energy of 25 GeV(5.9 GeV/u). After that, the Super Proton Synchrotron pushes them to 450 GeV (177 GeV/u) before they are delivered to the two rings of the LHC. Finally, the LHC accelerates particles up to the desired energy.

[1]The lead atoms sample are obtained by heating a small piece of pure lead to 500 °C.

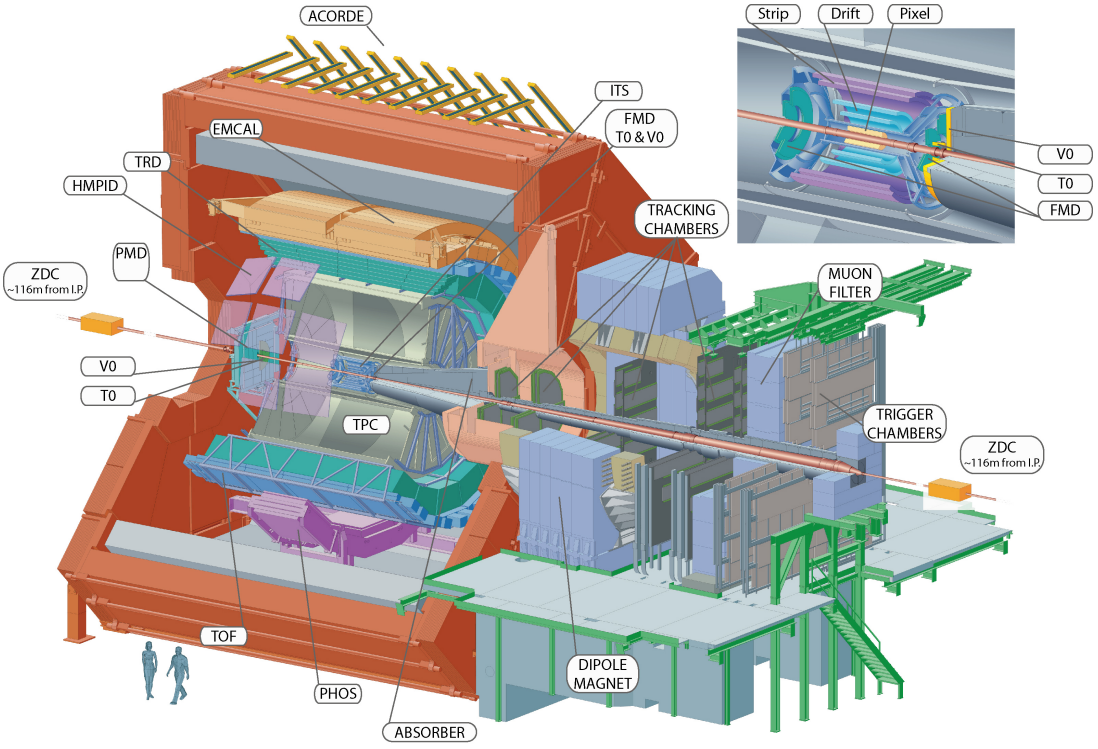

Figure 3.2: Schematic view of the ALICE detector [74] at the LHC.

3.2 ALICE Experiment

ALICE (A Large Ion Collider Experiment) [74] is a general-purpose heavy-ion experiment at the LHC designed to study the physics of the strongly interacting matter and the QGP in extreme conditions of energy density and temperature in nucleus-nucleus collisions. According to the high charged-particle multiplicity densities expected in nucleus-nucleus collisions, it was designed for $\mathrm{d}N_{ch}/\mathrm{d}y = 4000$[1]. Nevertheless, it was tested for charged-particle multiplicities up to $\mathrm{d}N_{ch}/\mathrm{d}y \approx 8000$. Moreover, it is the unique among the experiments at the LHC that allows to reconstruct and identify particles over a large range of momenta: starting from 100 MeV/c up to 100 GeV/c.

A schematic view of the ALICE detector is shown in Fig. 3.2. The detector consists of a central barrel part ($|\eta| < 0.9$) dedicated to measure hadrons, electrons and photons; a forward muon spectrometer ($-4 < \eta < -2.5$) dedicated to measure muons; and a set of forward detectors (V0, T0, PMD, FMD and ZDC) used for triggering, event characterization and multiplicity studies. Additionally, there is an array of scintillators (ACORDE) installed on top of the ALICE detector for cosmic ray triggering.

The central barrel is embedded in a large solenoid magnet with the capability to provide a magnetic field up to 0.5 Tesla. The sub-detectors that integrate the central barrel are the Inner Tracking System (ITS), the Time-Projection Chamber (TPC), the Time-Of-Flight (TOF), the High Momentum Particle Identification Detector (HMPID), the Transition Radiation Detector

[1]Measurements from the LHC run 1 have revealed lower charged-particle multiplicities than expected [79, 80].

(TRD), and the two electromagnetic calorimeters: the Photon Spectrometer (PHOS) and the Electromagnetic Calorimeter (EMCal)[1]. In the following subsections a brief description of the sub-dectors related to this thesis will be given.

3.2.1 The V0 detector

The V0 detector [82] consists of two arrays of scintillator plastic, V0-A and V0-C, which cover the pseudorapidity ranges $2.8 < \eta < 5.1$ and $-3.7 < \eta < -1.7$, respectively. Each array is segmented in four rings and each ring is divided into eight sections, resulting in 32 cells per array. The time of flight of particles crossing the detector is used to distinguish beam-beam interactions from beam-gas background interactions. This feature makes V0 important for the selection of minimum bias events and other process like single, double and central diffraction. Moreover, each cell of the two arrays has been calibrated to have the same response to the impact of one ionizing particle. Hence, using the information of the total energy deposited in the detector it is possible to measure the charged particle multiplicity in the corresponding pseudorapidity range and the centrality of the event. In addition, the V0 is also used to measure the beam luminosity and to determine the event plane.

3.2.2 The T0 detector

The T0 detector [83] consist of two arrays of 12 Cherenkov counters, T0-C and T0-A. The two arrays are located at 70 cm (T0-C) and 374 cm (T0-A) from the nominal vertex and cover the pseudorapidity ranges $-3.28 < \eta < -2.97$ (TO-C) and $4.61 < \eta < 4.92$ (T0-A). The T0 detector is used to measure the collision time with a precision of 40 ps and 20 ps for pp and Pb-Pb collisions, respectively. Moreover, it is capable of measuring the vertex position with a precision of 1 cm along the beam axis. This feature allows to reject beam-gas background interactions by rejecting events with a reconstructed vertex outside of a given range where the beam-beam interactions are expected. Additionally, due to its high precision, the T0 is also used as wake up trigger for the TOF and TRD detectors.

3.2.3 The Inner Tracking System

The Inner Tracking System (ITS) [84] consist of 6 cylindrical layers made of three kind of silicon detector technology: two layers of Silicon Pixel (SPD), two layers of Silicon Drift Detector (SDD) and two layers of Silicon Strip Detector (SSD). The ITS has an inner radii of 3.9 cm, an outer radii of 43.0 cm and it covers a pseudorapidity range $|\eta| < 0.9$. A schematic view of the ITS detector is shown in Fig. 3.3.

The ITS detector was designed to reconstruct the primary vertex with a resolution better than 100 μ and to reconstruct secondary vertices from photon conversions and weak decays of charm and beauty particles. It is also capable of reconstructing and identifying particles up to 200 MeV/c. Moreover, it is used to improve the momentum resolution of particles reconstructed by the Time Projection Chamber (TPC).

[1] During the long shut down 1 (LS1) the electromagnetic calorimeter (DCAL) that is an extension of the EMCal was installed [81]

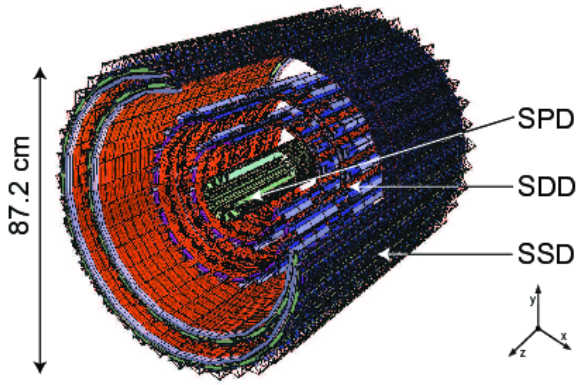

Figure 3.3: Inner Tracking System layout [84].

Table 3.1: Specifications of the ITS detectors [74].

Layer	Type	r cm	$\pm$z
1	pixel	3.9	14.1
2	pixel	7.6	14.1
3	drift	15.0	22.2
4	drift	23.9	29.7
5	strip	38.0	43.1
6	strip	43.0	48.9

The two innermost layers of the ITS (SPD) have the capability of measuring high charged-particle multiplicity densities of about 8000 tracks per unit of rapidity. Moreover, the SPD layers extend the ITS acceptance up to $|\eta| < 1.9$, which together with the Forward Multiplicity Detector (FMD) provide a continuous charged-multiplicity measurement. Furthermore, the material budget has been kept to a minimum, allowing the measuring of particles with momenta lower than 80 MeV/c.

The four outer layers (SDD and SSD) are capable of identifying particles through the measurement of the specific energy loss ($\mathrm{d}E/\mathrm{d}x$) when particles cross the detector. The specifications of the ITS detector are shown in Tab. 3.1.

3.2.4 The Time Projection Chamber

The Time Projection Chamber (TPC) [85, 86] is the main device for tracking and charged particle identification in ALICE. It has a cylindrical shape with an inner radius of about 85 cm, an outer radius of about 240 cm and an overall length along the beam direction of 500 cm. It has an acceptance coverage of $|\eta| < 0.9$ for full track length and 2π in azimuthal angle.

A schematic view of the TPC detector is shown in Fig. 3.4. The TPC consists of a field cage divided into two half-volumes of 250 cm separated by a high voltage electrode. The field cage is filled with a gas mixture, which composition has changed over the time. For pp collisions at $\sqrt{s}$ = 7 TeV the gas mixture was Ne : $C0_2$: N_2 (85.7:9.5:4.8), for pp collisions at $\sqrt{s}$ = 2.76 TeV and for p–Pb collisions at $\sqrt{s_{\mathrm{NN}}}$ = 5.02 TeV the composition was Ne : $C0_2$ (90:10) and in the LHC Run2 the composition has changed to Ar : $C0_2$. The field cage provides a uniform electrostatic field in the gas volume in order to transport ionizing electrons from their point of creation to the readout chambers. The electrode operates with a high voltage of 100 kv resulting in a maximum drift time of about 90 μs. The readout consists of multi-wire proportional chambers located in the endplates of both sides of the TPC. The readout is divided into 18 sectors and each sector is segmented into two chambers which in turn are divided into pads. There are about 560 000 pads which size depends of the track density according to their radial position. The readout chambers are activated upon a L1 trigger for the drift time interval ($\sim$100 μs).

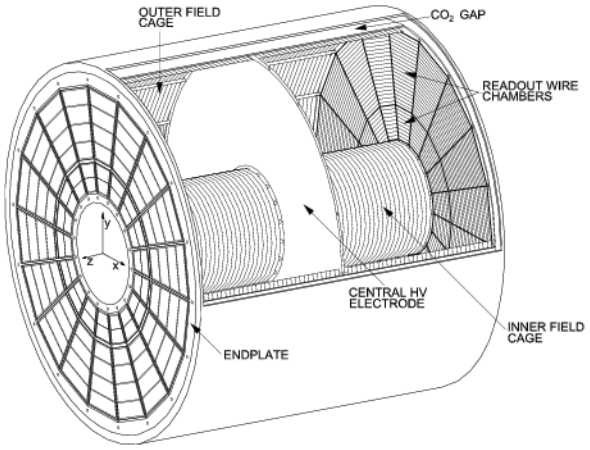

Figure 3.4: Schematic view of the TPC detector [86].

The TPC is optimized to measure multiplicities up to $\mathrm{d}N_{ch}/\mathrm{d}y = 8000$, resulting in 20 000 charged primary and secondary tracks in the acceptance per one event. Furthermore, with a maximum number of 160 clusters, the TPC allows to measure particles within a momentum range from 100 MeV/c up to 100 GeV/c with a good resolution. It also allows to identify particles through the specific energy loss measurement ($\mathrm{d}E/\mathrm{d}x$) with a resolution of $\sim 5\%$ for tracks with 160 clusters [86]. The particle identification capabilities of the TPC based on the $\mathrm{d}E/\mathrm{d}x$ will be described in detail in section 3.3.3.

3.2.5 The Time-Of-Flight detector

The Time-of-Flight (TOF) [85, 87, 88] is a detector devoted to identify kaons and pions in the momentum range from 0.3 to 2.5 GeV/c and protons in the range from 0.3 to 4 GeV/c with a separation better than 3σ for π/K and K/p. It has an acceptance in the pseudorapidity range of $|\eta| < 0.9$ and a full acceptance in azimuthal angle. Its total cylindrical surface area is $\sim$ 141 m^2 with an inner radius of 370 cm and an outer radius of 399 cm. Its whole structure is divided into 18 sectors in ϕ and 5 segments along the beam direction (with holes in front of PHOS). The design of the TOF is based on Multi-gap Resistive-Plate Chamber (MRPC) technology and it has more than 10^5 independent channels.

3.2.6 The Transition Radiation Detector

The Transition Radiation Detector (TRD) [89, 90] was designed to identify electrons with momenta higher than 1 GeV/c. The TRD consists of 6 layers segmented into 18 sectors in azimuthal direction and into 5 modules along the beam direction (z), for a total of 540 chambers (with holes in front of PHOS). Each chamber contains a radiator, a gas detector with a drift region of 3.0 cm and a multi-wire proportional chamber with amplification on anode wires of 0.7 cm. The gas mixture in the chamber is Xe:C0$_2$ (85:15). The TRD is located between the TPC and TOF detectors and covers the pseudorapidity range $|\eta| \leq 0.9$. The detector is based on transition radiation. This consists on photons with an energy in the X-ray range created when an electron with $\gamma > 800$ crosses several boundaries between media with different dielectric constants. In conjunction with the TPC and ITS detectors the TRD allows to study semi-leptonic decays of

heavy-flavor hadrons, di-electron mass spectra of heavy quarkonia states and jets. In addition, the TRD provides a jet and an electron trigger at L_1.

3.2.7 The Photon Spectrometer

The Photon Spectrometer (PHOS) [91] is a high energy resolution ($\sigma_{E(\mathrm{GeV}/c)}/E = 0.01\%/E \oplus 0.04/\sqrt{E} \oplus 0.01\%$) photon spectrometer designed to provide photon identification. It is located at a distance of 460 cm from the interaction point and covers a limited pseudorapidity acceptance ($|\eta| < 0.12$) and azimuthal angle ($260^\circ < \phi < 320^\circ$). It consists of a highly segmented electromagnetic calorimeter which is divided into 5 modules (during the LHC Run1 only 3 modules were installed and in Run2 half module more was added) and a Charge-Particle Veto (CPV) detector (only one PHOS CPV module installed from Run2) consisting of a Multi-Wire Proportional Chamber with cathode-pad readout. Each module is segmented in $64x56$ cells made of lead-tungstate crystals. Furthermore, PHOS provides L_0,L_1 triggers for photon and electrons.

3.2.8 The ElectroMagnetic Calorimeter

The ElectroMagnetic Calorimeter (EMCal) [92] is a large Pb-scintallator sampling calorimeter with a cylindrical geometry. It was designed in 2009 so that increases the electromagnetic-calorimeter coverage of ALICE by nearly one order of magnitude. It is located at a distance of ~ 4.5 meters from the interaction point and it is positioned approximately opposite in azimuth to PHOS. It has an energy resolution of $\sigma_{E(\mathrm{GeV}/c)}/E = 5.1\%/E \oplus 11.1/\sqrt{E} \oplus 1.7\%$ [93], and covers a pseudorapidity range $|\eta| < 0.7$ and azimuthal angle $1.4 < \phi < 3.4$. Furthermore, it provides a fast and efficient trigger (L_0,L_1) for hard jets, photons and electrons.

3.3 AliRoot: ALICE offline framework

The software used for simulation, reconstruction, calibration, visualization and analysis of the data produced by the ALICE experiment is called AliRoot [94]. It is based on ROOT [95], which is an oriented-object framework written in C++ that implements a set of tools for the data analysis of the high-energy physics. The development of AliRoot started in 1998 and it has been an important software tool used at the different stages of the ALICE experiment, which include the designing and testing of sub-detectors and more recently the analysis of the real data [96].

A schematic view of the AliRoot framework is shown Fig. 3.5. Thanks to its modular design, AliRoot allows to implement different Monte Carlo generators, transport packages, detector descriptions (this includes geometry, detector responses, etc.) and reconstruction algorithms with a minimum interference with the rest of the components. Moreover, as it will be explained in section 3.4.1, AliRoot incorporates an interface to AliEn so that it is capable of running in a grid environment.

The two goals of AliRoot are (1) to reproduce as much as possible the collisions events and the detector responses and (2) to reconstruct the raw data produced by either simulations or real events [96]. The achievement of the above has an important significance for the understanding of the data produced in ALICE. Therefore, a brief description of the simulation and reconstruction will be given below.

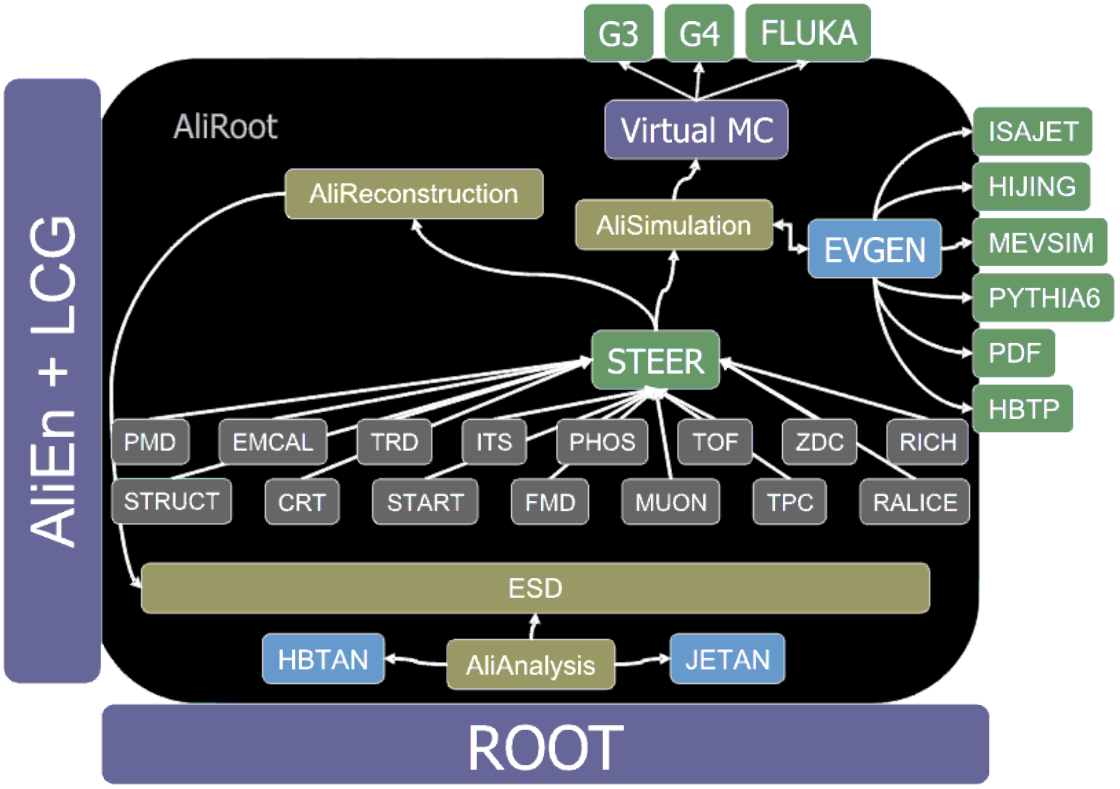

Figure 3.5: A schematic view of the AliRoot architecture [94]

3.3.1 Simulation

The simulation of an event can be divided into two stages: (1) the generation of the particles produced in the main interaction (pp, p–Pb, and p–Pb collision or particle cocktails) and (2) the transport of these particles through the detector. The (1) is carried out by Monte Carlo generators and the (2) by transport packages. AliRoot implements various interfaces with different Monte Carlo generators, this includes PYTHIA [97], PHOJET [98], HIJING [99] and DPMJET [100]. Apart from this, it also contains interfaces with various transport packages like GEANT3 [101], GEANT4 [102] and FLUKA [103]. The description of the Monte Carlo generators used in this thesis is given in section 4.1.2.

The simulation starts with the generation of particles produced in the main interaction. The output of the Monte Carlo generators is stored in a hierarchy tree data structure that contains information of the primary particles (those produced in the main interaction). This information includes their properties (momentum, energy, identity, etc.) and their family tree (decay chain), which are needed to calculate the reconstruction efficiency and the acceptance of the different detectors during the analysis process. In the next step, the transport packages propagate these particles through the detector. During this propagation, the interaction between particles and the detector material produces hits and may also produce new particles (for this reason, it is very important to have a good description of the detector material in AliRoot). The hits contain information of the energy deposited at the sensible parts of detector as their position and the particles which generate them. Afterwards, the detector response to the hits is given in summable digits, which are corrected for possible detector effects like noise before they are

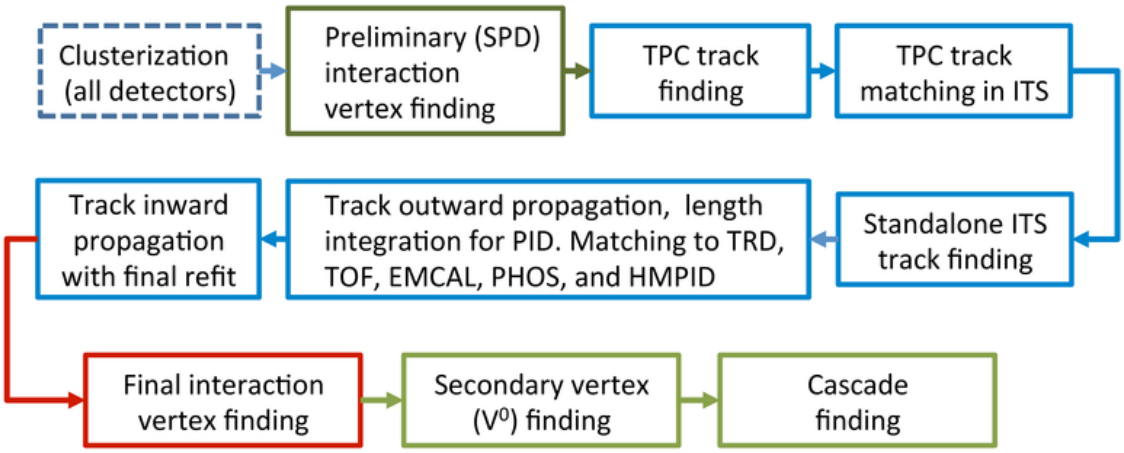

Figure 3.6: Event reconstruction chain [104].

transformed into digits. Finally, digits should have similar format as the raw data generated by real events so that they serve as input for the reconstruction chain that will be briefly described below.

3.3.2 Reconstruction

A schematic description of the different stages of the reconstruction process is given in this section (see Fig. 3.6). The reconstruction chain starts with the clusterization process for all detectors. In this process, groups of adjacent digits are transformed into clusters. The centroid of the clusters is assumed to be the point where the particle crosses the detector. The way that the digits are transformed into clusters can varied from each detector. A more detailed description of clusterization process can be found in [85]. The subsequent stages as the primary vertex reconstruction, track reconstruction and secondary vertex reconstruction will be briefly described below.

Primary vertex reconstruction

The primary vertex is computed using the hits in the two layers of the SPD [85]. The correlation between the hits in the first and in the second layer is calculated using the method described in [105]. The resulting correlation distribution is fitted with a constant and a Gaussian function in order to obtain the position of the primary vertex, which is assumed to be part of the fit.

At the stage of the primary vertex reconstruction, it is not possible to know if the two hits were produced by the same particle. Therefore, all the combinations between the hits in the first and in the second layer are taken into account. This produces a large amount of uncorrelated pairs (combinatorial background), which dominates the correlation distribution. In order to reduce the combinatorial background, two methods described below can be followed [105].

In the first method, only pairs with a z-vertex position (z_v) within a confidence interval are used for the estimation of primary vertex position. The intervals are estimated as follows: first a

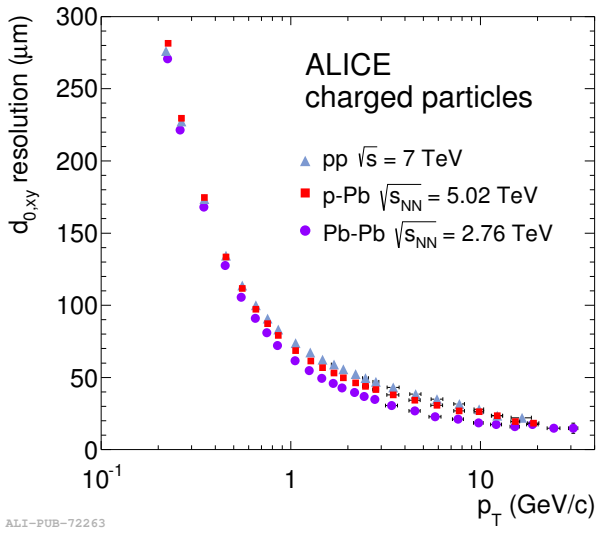

Figure 3.7: Impact parameter resolution in the transverse plane versus p_{T} for ITS-TPC global tracks in pp, p–Pb and Pb–Pb collisions [104].

rough estimation of the z-vertex position (z_v^0) is done by using the z_v-distribution of the hits in the two SPD layers. Subsequently, the confidence region (z_v^{min}, z_v^{max}) is obtained by evaluating the function $z_v^{min,max} = z_v^0 \pm \Delta z_v^0$, where $\Delta z_v^0 = a + b z_v^0 + c(z_v^0)^2$. On the other hand, in the second method, as the hits produced by the same particle in the first layer and in the second layer of the SPD have a similar azimuthal angle [105], only pairs with a $\Delta\phi$ below a certain value are taken into account. The cut value applied on $\Delta\phi$ depends on the particle density and on the magnetic field settings.

The resolution of the primary vertex depends on the charged-particle multiplicity; events with low multiplicity have lower combinatorial background but worse vertex resolution. The resolution also depends on the position of the primary vertex. At larger values of $|z_v|$, the correlation distribution does not reproduce the vertex position because many of the primary particles are produced outside the detector acceptance, and therefore they do not leave hits on the SPD. However, a good description of the vertex position is given up to $|z_v| < 12$ cm [85]. The resolution of the impact parameter (see Eq. (3.1)) in the transverse plane versus p_{T} for ITS-TPC global tracks is shown in Fig. 3.7 for pp, Pb–Pb and p–Pb collisions. Similar behaviour is observed in the three systems, the resolution for is $\sim 60\mu m$ for momenta above 1 GeV/c and it drops to $\sim 25\mu m$ for momenta above 10 GeV/c.

Track reconstruction

The track reconstruction is done using the central tracking detectors: ITS, TPC, TRD, TOF, HMPID, PHOS and EMCal. The track finding procedure starts searching for track candidates or "seeds" by combining clusters in the outermost pad-rows of the TPC. The seed finding procedure is carried twice using two different approaches: the first assumes that the tracks originate at the main interaction and the second assumes that the tracks originate somewhere else. A more detailed description of the two approaches can be found in [85].

Once the track candidates are found, the next step is to propagate them, pad-row by pad-row, to the inner limit of the TPC. For this, the Kalman filtering algorithm [106], which estimates the track parameters at one point using a state vector, is used. The state vector takes into account multiple scattering, energy loss of the tracks and the precision of the reconstruction of the clusters [85]. Therefore, if one cluster at the next pad-row is compatible with the track trajectory it is added to the track and the state vector is updated. Afterwards, when all track candidates have reached the limits of the TPC, the algorithm continue in the ITS, which eventually tries to propagate the TPC tracks to the primary vertex. At this point, all the tracks that have been reached the primary vertex with TPC and ITS clusters are labeled as ITS-TPC global tracks. The ITS clusters that have not been associated to these tracks are used for the "ITS stand-alone" finding process, which tries to reconstruct tracks that have not reached the TPC or tracks that crossed the TPC in dead zones.

Next, a second pass of the algorithm in backward direction is performed, starting from the primary vertex to the outer limit of TPC. Once on the TPC limit, tracks are propagated to the TRD, TOF, HMPID, PHOS and EMCal detectors if they are inside of the detector acceptances. At this level, PID information is assigned to the tracks. Finally, a final track refit in inward direction (towards to the main interaction) is performed in order to take the final track parameters. This procedure is carried out twice: with a vertex constraint and without vertex constraint (to avoid secondary track losses). Additionally, a vertex finding process is carried out using the ITS-TPC global tracks found above to obtain the final position of the interaction vertex.

The track finding efficiency for ITS-TPC global tracks is shown in 3.8 for pp collisions at $\sqrt{s}$ = 0.9, 2.76, and 7 TeV (bottom panel) and for p–Pb collisions at $\sqrt{s_{\rm NN}}$ = 5.02 TeV (top panel). The track finding efficiency for pp collisions shown in the figure is integrated over all particle species and it is $\sim 70\%$ for momenta above 0.5 GeV/c for $\sqrt{s}$= 0.9, 7 TeV, dropping for $\sqrt{s}$ = 2.76 up to $\sim \%55$ due to the absence of the SDD detectors. On the other hand, for p–Pb collisions, the efficiency for kaons, protons and pions are shown separately for positive (top left) and negative (top right) particles, reaching $\sim 90\%$ for pions and protons and $\sim 70\%$ for kaons for momenta above 0.5 GeV/c.

Secondary vertex reconstruction (V^0)

The reconstruction of secondary vertices is very important for the detection of neutral particles like K^0_S, Λ, $\bar{\Lambda}$ and photons. The decay topology for $K^0_S \to \pi^+\pi^-$, $\Lambda \to p\pi^-$, and $\bar{\Lambda} \to \pi^+\bar{p}$ which is similar to the one of photon conversions, is shown in Fig. 3.9. This topology is characterized by having a displaced vertex with two opposite-charge particles (track daughters). Moreover, given that the pattern shape of these decays (photon conversions) observed on the detector resemble the letter “V”, the mentioned neutral particles are known as V^0s.

The V^0 finding procedure starts selecting secondary tracks (those which are not produced in the main interaction). For this, tracks with a distance to the main vertex below a certain value in the transverse plane (xy) and along the beam direction (z), are rejected. The proximity to the main vertex is calculated by using the distance of closest approach (DCA), which is defined as [85]:

$$\mathrm{DCA}_{xy} = \rho - \sqrt{(x_v - x_0)^2 + (y_v - y_0)^2} \qquad \mathrm{DCA}_z = z_{track} - z_v \tag{3.1}$$

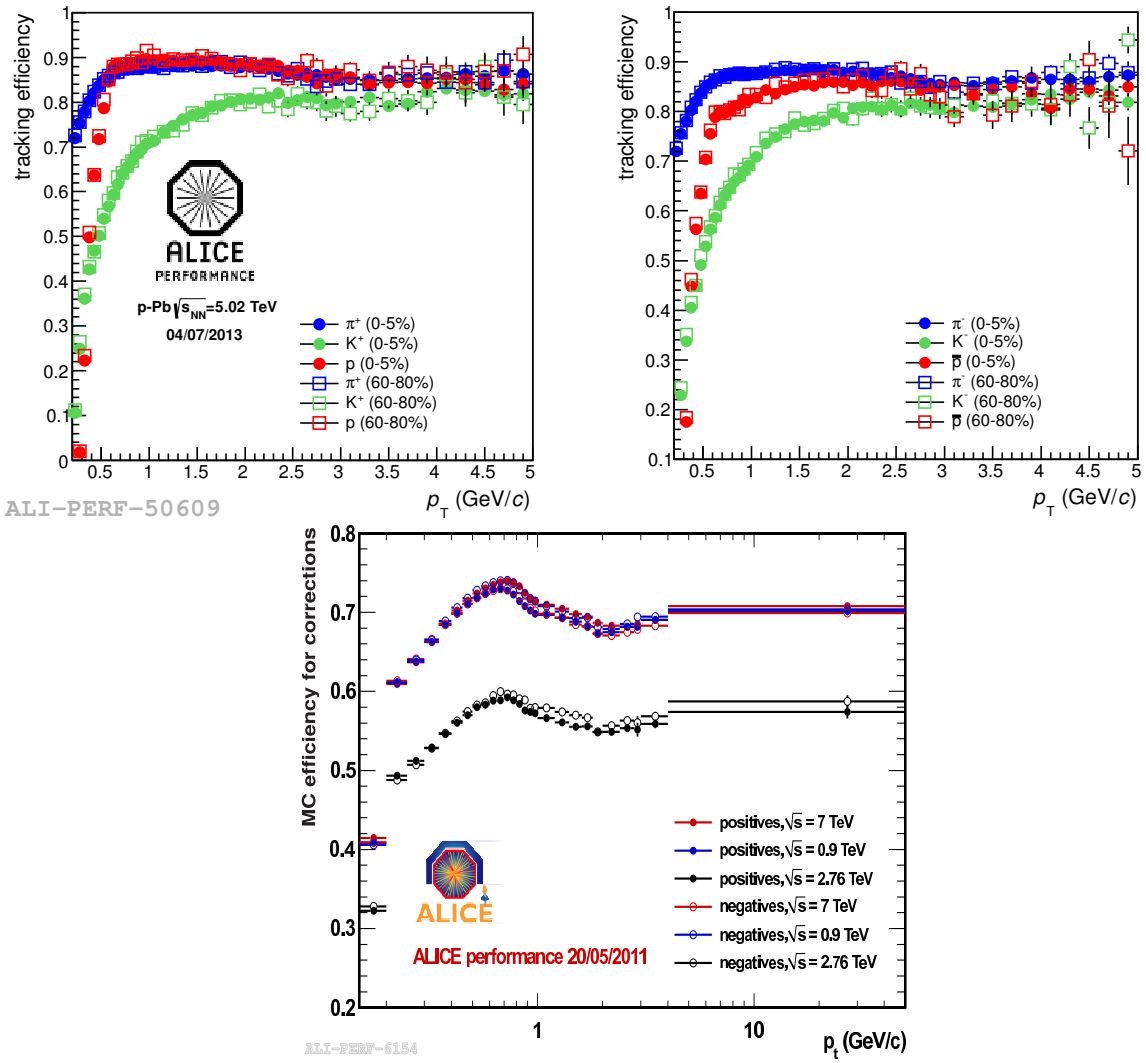

Figure 3.8: (Top) Global tracks efficiency for positive (left panel) and negative (right panel) particles in p–Pb collisions at $\sqrt{s_{\rm NN}}$ = 5.02 TeV [107]. (Bottom) Global tracks efficiency for positive and negative particles for pp collisions at $\sqrt{s}$ = 0.9, 2.76 and 7 TeV [108].

where ρ and (x_0, y_0) corresponds to the radius and the centre of the track projection in the transverse plain, (x_v, y_v, z_v) is the primary vertex position, and z_{track} is the z-track position resulting from the extrapolation of the track to the DCA$_{xy}$.

Once the secondary tracks are selected, the next step is to form opposite-charge pairs. For this, all the combinations between positive and negative secondary tracks are done. Afterwards, for all these pairs, the DCA between the two track daughters is calculated by using a 3-dim helix track parametrization [85]. If the DCA is larger than a given value, the pair is rejected. Subsequently, the point of closest approach (PCA) between the two tracks is assumed to be the secondary vertex position, and only those V^0s with a PCA within a fiducial zone are accepted in this procedure. The inner radius of this fiducial zone is normally defined very close to the main

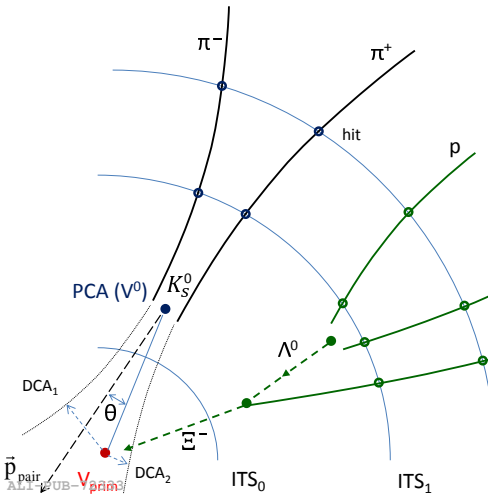

Figure 3.9: Schematic view of the secondary vertex reconstruction [104]. The solid lines correspond to the reconstructed charged particle tracks extrapolated to the secondary vertex candidates. The dashed lines represent the extrapolation to the primary vertex and auxiliary vectors.

interaction (0.5 cm) but it can vary according to the collision system and energy. On the other hand, the outer radius is defined at one point within the TPC where the two tracks daughters can be reconstructed with a good resolution.

Next, the V^0 momentum is calculated as the sum of the momentum vectors of the two track daughters at the PCA. Thereafter, the procedure checks if the V^0 proceeds from the main interaction by applying a cut on the cosine of the angle between the V^0 momentum vector and the vector which connects the PCA and the main vertex. Finally, all the V^0s that survive the above cuts are considered V^0 candidates and are stored in analysis output files.

There are two algorithms for the V^0 finding in ALICE: one performed during (On-the-Fly) and other performed after (offline) the track finding process. The On-the-Fly method benefits from the information available during the track finding process as the state vector of the tracks and the ITS and TPC clusters. This allows to do extra refinements to the secondary tracks parameters (momentum, vertex position, etc.,) that in the offline method are not possible to do. However, the offline method allows to re-computed the V^0 sample without further pass reconstructions of the full data set.

In addition, thanks to their kinematical properties as momentum, mass, etc., the V^0s candidates can be illustrated in a two dimensional plot called "Armenteros-Podolanski plot" [109], which x (α) and y (q_{T}) axes are defined as:

$$\alpha = \frac{p_{\mathrm{L}}^{+} - p_{\mathrm{L}}^{-}}{p_{\mathrm{L}}^{+} + p_{\mathrm{L}}^{-}} \tag{3.2}$$

$$q_{\mathrm{T}} = \frac{|\overrightarrow{p_{\mathrm{T}}} \times \overrightarrow{p_{\mathrm{m}}}|}{|\overrightarrow{p_{\mathrm{m}}}|} \tag{3.3}$$

where q_{T} is the transverse momentum of the daughter particle with respect to the momentum of the mother particle and α is the asymmetry of the longitudinal momentum of the positive p_{L}^{+}

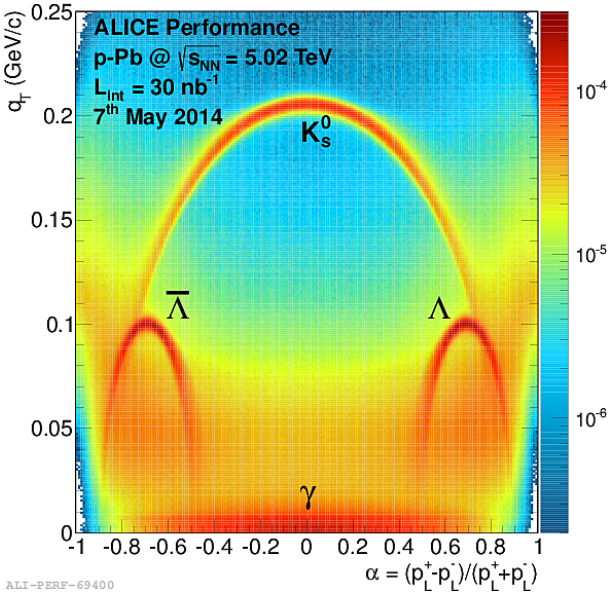

Figure 3.10: Armenteros-Podolanski plot for p–Pb collisions at $\sqrt{s_{\rm NN}}$ 5.02 TeV.

and the negative $p_{\rm L}^-$ daughters relative to the direction of the momentum of the mother particle. The Armenteros-Podolanski plot is shown in Fig. 3.10 for all V^0 candidates which were selected using soft cuts in p–Pb collisions. The bands corresponding to photons, K^0_S, Λ and $\bar{\Lambda}$ are clearly visible in the plot. The symmetric α distribution observed for photons can be explained by the fact that their resulting conversion products (e^+, e^-) have the same mass, and therefore the momentum of photons is distributed symmetrically between the two electrons. A similar situation is present for the K^0_Ss decay products (π^+, π^-). By contrast, in the case of $\Lambda \rightarrow \pi^+\bar{p}$ and $\bar{\Lambda} \rightarrow \pi^- p$, where protons and pions have different masses, the momentum of Λs ($\bar{\Lambda}$s) is distributed asymmetrically between the two particles, taking protons (antiprotons) a larger part on average. Furthermore, the observed lower $q_{\rm T}$ values for photons are due to their small opening angle.

3.3.3 Particle Identification

ALICE is capable of measuring, identifying different species in different $p_{\rm T}$ ranges exploiting the particle identification (PID) capabilities of the detectors: ITS, TPC, TOF, HPMID and TRD. For more precise PID, ALICE allows to combine the information of more than one detector if the track is inside their acceptance [110]. As the PID of the TPC was the main one used in this thesis, only a description of the particle identification with the TPC will be given in this section.

The particle identification with the TPC is based on the specific energy loss ($\mathrm{d}E/\mathrm{d}x$), by ionization, when a particle propagates through the detector. The $\mathrm{d}E/\mathrm{d}x$ for a given track is obtained from the total energy deposited in the clusters used for track reconstruction. However, as this method is sensitive to overlapping, it is only used in environments with not very high charge-particle multiplicity like in pp collisions. Instead of the total energy, in Pb–Pb collisions where the charge multiplicity is much higher than that in pp collisions, the maximum energy deposited in a cluster normalized to the length of the corresponding track segment is used for the estimation of the $\mathrm{d}E/\mathrm{d}x$ [85]. The $\mathrm{d}E/\mathrm{d}x$ can be theoretically described by the Bethe Bloch equation:

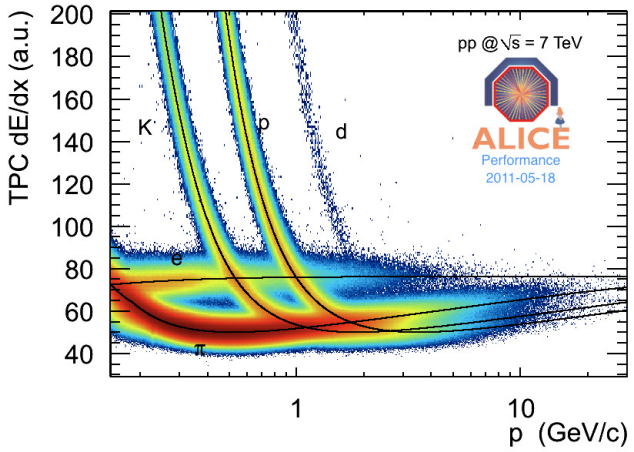

Figure 3.11: Specific energy loss ($\mathrm{d}E/\mathrm{d}x$) versus momentum for global tracks in pp collisions at $\sqrt{s}$ = 7 TeV [111]. For comparison, the Bethe-Bloch lines (black) for electrons (e), kaons (K), protons (p), and pions (π) are superimposed.

$$(dE/dx) = C_1/\beta^2(ln(C_2\beta^2\gamma^2) - \beta^2 + C_3) \tag{3.4}$$

where $\gamma = 1/\sqrt{1-\beta^2}$ and C_1, C_2 and C_3, are constants which relate the mean energy loss per path length to the velocity β of the particle. The parameters of the formula are obtained after several calibrations of the TPC and adjusted for each run of data taking. During the analysis process, those parameters are loaded and the expected value of $\mathrm{d}E/\mathrm{d}x$ for a given track is computed. Then, the compatibility between the measured $\mathrm{d}E/\mathrm{d}x$ and the predicted $\mathrm{d}E/\mathrm{d}x$ is computed and it is expressed in number of standard deviations n_σ. Finally, the n_σ value is used to identify the track.

The $\mathrm{d}E/\mathrm{d}x$ performance for global tracks in pp collisions at $\sqrt{s}$ = 7 TeV is shown in Fig. 3.11. For comparison, a parametrization of the Bethe-Bloch bands has been superimposed. The measured $\mathrm{d}E/\mathrm{d}x$ for electrons (e), kaons (K), protons (p), deuteriums (d) and pions (π) are clearly visible in the figure.

3.4 ALICE computing model

The enormous amount of data produced by the ALICE experiment (~ 50 Petabytes until now [112]) need to be processed in different ways in order to be available for their analysis to the ALICE collaboration, which is composed by hundreds of scientist from different parts of the world. Furthermore, for an optimal work the access to the data and to the software tools should be democratic, permanent and efficient for all these people [96]. This leads to the requirement of a tremendous amount of computing power (storage, data processing, bandwidth, etc.,), which translates into a large number of resources, including buildings, hardware and humans support. These and other reasons, make difficult to concentrate all these components in a single institution [96]. Consequently, it was better to split all these infrastructure into the various institutes, universities and research centres belonging to the collaboration by implementing a computing model based on the Grid technology [113]. This technology allows for several heterogeneous

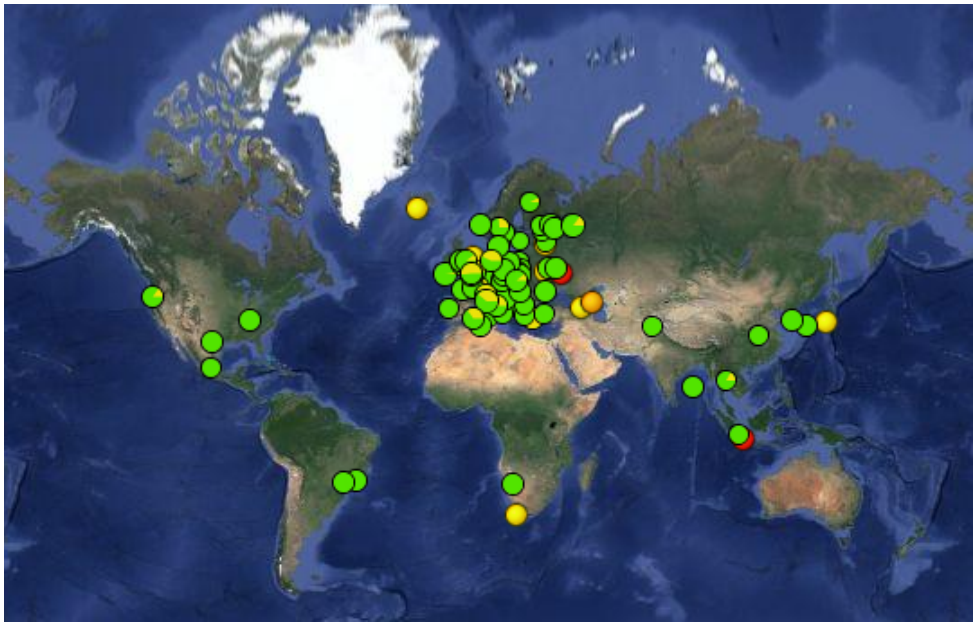

Figure 3.12: Distribution of the ALICE computing nodes around the world. Plot taken from [115].

computing resources to work in a coordinate way to carry out a common task regardless of their location; they can be located anywhere on earth. The goal of the grid is to give end-users transparent access to the computing components. This means that the scientists should not worry for the complexity of the grid, they should have the feeling of being working on a single powerful computer.

The ALICE computing infrastructure is therefore integrated by various nodes spread over four continents (see Fig. 3.12): Europe, America, Asia and Africa. In order to have a better control of the components and to be less dependent to the issues related to the network connections, the nodes are classified according to a hierarchical model named MONARC [114]. This model organizes the nodes (based on the computing power and the services they offer) into five tiers, running from T0 to T4. The highest tier, T0, is located at CERN and it perform tasks that need more reliability and computing capacity, including data taking, first reconstruction of the data, and a local copy of the RAW data. One level below there is the T1 which is capable of processing subsequent reconstructions of the data and of providing mass storage service (for backups of RAW data). It can also perform scheduled Monte Carlo simulations and data analysis. The next in line is the T2 that is dedicated to perform Monte Carlo simulations and data analysis launched by the users.

What makes the grid possible is a computing software called middleware [113]. The middleware implements a set of network protocols and services for the management of the geographically distributed computing resources. Since 2000, the ALICE experiment has developed its own middleware to give their users access to grid resources. This middleware is called AliEn and it will be described below.

3.4.1 AliEn: ALICE Environment on the GRID

AliEn [116] is a middleware software developed in 2000 to provide a transparent environment for the reconstruction, simulation and data analysis of the ALICE experiment. It is built manly ($\sim$ 95 %) from an existing open source code and web services and it is optimized to hide the multiple components of the grid to the end-user, looking as a single entity [96]. The above can be possible by implementing a sophisticated file catalogue and an efficient workload manager. It also includes the following services: authentication, authorization and auditing, information, Grid and Job monitoring, and storage and computing elements.

The workload manager is the responsible of coordinating the job execution in AliEn, which given the amount of heterogeneous components of the grid, it is not a trivial task. For an efficient work, the workload manager should send the jobs, based on their requirements, to the most appropriate resource (computing element) for their execution. To achieve this, AliEn implements the pull approach [96], which consists in collecting information, from time-to-time, of the status of each computing element.

The status of a computing element is collected by the so-called job agents (JA), which execute various tests in it. The results of these tests, which can include information of the disk space, memory size, CPU capacity, etc., are sent back to a central manager, which, if everything is o.k, puts the computing element on a list of available resources. While the computing element membership is valid, it can be chosen for a job execution if it is the best option.

Although the AliEn file system is composed by multiple storage elements, their file system environment resembles the one for Linux, which organizes the directories and files in different levels. This transparent environment is achieved by implementing high-level indexing. This includes a file catalog with contains information to retrieve the files from the closest storage element, and it is also optimized to avoid duplicated entries in the catalog.

AliEn uses a framework named MONALISA (MONitoring Agents using a Large Integrated Services Architecture) [115] to check the status of its different components and the status of the job executions. The framework implements a web interface where every user with a grid certificate can access to check the status of his/her different jobs. Moreover, it contains a graphical interface that allows to manipulate the output files of each analysis.

Chapter 4

Electron, Virtual Photon and Photon Reconstruction

The π^0 Dalitz decay used in this thesis for the π^0 meson reconstruction was described in chapter 2. As photons will be reconstructed using the photon conversion method (PCM), this implies the detection of two electron-positron pairs: one originated at the main interaction vertex since virtual photos convert internally, and other from a secondary vertex since photons convert throughout the detector material. The method employed for the reconstruction of the two electron-positron pairs will be explained in this chapter. The description of the data sample and event selection used in this analysis is also included.

4.1 Data sample and event selection

All data used in this thesis were taken during the LHC Run1. The proton-proton (pp) collision data at $\sqrt{s}$ = 7 TeV and at $\sqrt{s}$ = 2.76 TeV and the proton-lead (p–Pb) collision data at $\sqrt{s_{\rm NN}}$ = 5.02 TeV were collected with a minimum bias trigger (MB)[1] in 2010, 2011 and 2013, respectively. This trigger is configured in such a way that it minimizes, as much as possible, the machine-induced effects which could bias the events related to the physics process under study. The MB configuration depends on the data taking conditions (see Tab. 4.1). In pp collisions, the minimum bias trigger configuration ($\rm MB_{OR}$) required a hit in either the SPD or V0-A and V0-C detectors. On the other hand, the minimum bias trigger used in p–Pb collisions ($\rm MB_{AND}$) required a hit in both V0-A and V0-C detectors. The $\rm MB_{AND}$ trigger selects non-single diffractive collisions (NSD). Moreover, in order to reject background events which proceed mainly from beam-gas collisions, the time in which particles arrive to the V0 detector is taken into account. Normally, the arrival time of signals from background events is shorter than that of signals from beam-beam collision events.

Subsequently, all the information needed for the MB trigger and for background rejection are re-calculated offline in order to discard technical issues that may lead to a bad selection. The offline information is used in this analysis during the event selection which will be explained later in this section.

[1] Rare triggers with Calorimeter and Muon detectors were also used in data taking, but not in this thesis

System	$\sqrt{s_{\rm NN}}$ (TeV)	Running mode	Peak $\mathcal{L}$ ($\mu b^{-1} s^{-1}$)	Delivered $\mathcal{L}$
pp	7	MB + rare	1.7	0.5 pb^{-1}
pp	2.76	MB	4.4 x 10^{-1}	46 nb^{-1}
p–Pb	5.02	MB	5 x 10^{-3} (10 kHz)	0.91 nb^{-1}

Table 4.1: Run conditions for pp collisions and for p–Pb collisions during the LHC Run1 [104].

A compilation of data and Monte Carlo samples used in this thesis with the number of analyzed events is given in Tab. 4.2.

4.1.1 Run selection

The data taking is divided into periods and each period into runs. The way that periods and runs are divided is related to their conditions: duration and detector settings. After the recording period, a quality assurance task (QA) is performed in order to check the reliability of each run. The description of the QA task can be found in [117]. Only runs labeled as good by the QA task were taken into account in this analysis. The list of the all periods and runs used in this analysis can be found in appendix A.

4.1.2 Monte Carlo simulations

In this section a description of the Monte Carlo event generators used for simulation of full-events in pp and p–Pb collisions (see Tab. 4.2) used in this thesis will be given.

PYTHIA

PYTHIA [97] is a software tool used to simulate high-energy events. It was originally written in fortran but it has moved to C++. Pythia implements a library which contains a set of models and analytical results to simulate soft and hard processes. The soft processes, which include elastic and single and double diffraction, are based on the Regge theory [118]. On the other hand, the versions 6.4 (fortran) and 8.1 (C++), which were used for the simulations shown in Tab. 4.2, include an extensive library that allows Pythia to simulate about 300 different hard processes. If these processes are classified as the number of final-state objects, one can say that Pythia is optimized for leading 2→1 and 2→2 processes.

The generation of a high-energy interaction, starts with the simulation of the hard processes. The initial-state parton configuration is given by parton distribution functions (PDFs). The default PDFs set for proton in Pythia is CTEQ 5L [119]. The algorithms used to simulate the initial- and final-state parton showers are base on $p_\perp$-ordered evolution [120]. The hadronization of the

[a] In order to increase the statistics of the π^0 Dalitz decay channel within a reasonable computing time, the branching ratios of the 2γ and Dalitz π^0 decay channels were set as 0.9 and 0.1, respectively, in the LHC14b2 sample.

	Sample name	System	$\sqrt{s_{\mathrm{NN}}}$ (TeV)	MB events	Accepted
Data	LHC10b, Pass 2	pp	7	26.1M	23.5M
	LHC10c, Pass 2			69.8M	61.8M
	LHC10d, Pass 2			158.7M	126M
	LHC10e, Pass 2			131M	104.2M
Total				385.6M	315.5M
MC, PYTHIA 6.4	LHC10d1 (b)	pp	7	18.7M	17.2M
(Perugia0)	LHC10d4 (c)			49.8M	47.6M
	LHC10f6a (d)			130.4M	104.6M
	LHC10e20 (e)			7.3M	6M
MC, PHOJET	LHC10d2 (b)			14.5M	13.7M
	LHC10d4a (c)			62M	60.4M
	LHC10f6 (d)			74.9M	63.5M
	LHC10e21 (e)			10.2M	8.8M
Total				367.8M	321.8M
Data	LHC11a, Pass 4	pp	2.76	67.3M	53.7M
MC, PYTHIA 8.1	LHC12f1a, Pass 4		2.76	24.3M	20.2M
MC, PHOJET	LHC12f1b, Pass 4			20.6M	17.2M
Total				44.9M	37.4M
Data	LHC13b, Pass3	p–Pb	5.02	28M	24.3M
	LHC13c, Pass2			88.9M	77.5M
Total				116.9M	101.8M
MC, HIJING	LHC14b2[a]	p–Pb	5.02	49.8M	43.5M

Table 4.2: Data and Monte Carlo samples used for analysis and corrections of the π^0 meson production measurement.

partons at the final state is based on the Lund string fragmentation framework [121]. Furthermore, Pythia implements particle decay tables based on the 2006 PDG to simulate the decays of unstable particles produced in the hadronization process.

PHOJET

PHOJET [98] is designed to study the soft and semihard particle production at high energies. Based on the ideas of the Dual Parton Model (DPM) [122] (to describe soft process) and pQCD models (to describe hard processes), it simulates hadron-hadron, photon-hadron and photon-photon interactions at high energies. With the DPM it allows to calculate the cross sections of both elastic and inelastic interactions. By the two-component approach of DPM [123], which incorporates soft and hard processes, it gives a description of hadronic interactions at high energies. In this model the soft and hard processes are simulated separately, but their results are merged following a unitary procedure. The way that both processes are differentiated is by applying a transverse momentum cutoff $p_{\perp}^{\mathrm{Cutoff}}$. Then, hadronic interactions with a transverse momentum greater than $p_{\perp}^{\mathrm{Cutoff}}$ are considered as hard. The initial-state radiation can follow the DGLAP evolution equations [124–127]. The final-state radiation is similar to the one used for Pythia.

Cut name	pp	p–Pb
Alice Physics Selection	MB_{OR}	MB_{AND}
Pile-Up rejection	IsPileupFromSPD(3,0.8,3.,2.,5.) IsSPDClusterVsTrackletBG	IsPileUpFromSPD(5,0.8,3.0,2.0,5.0) IsSPDClusterVsTrackletBG
Primary vertex (Vtx)	$N_{\text{contributors}} \geq 1$ $\lvert \text{Vtx}_z \rvert < 10$ cm	$N_{\text{contributors}} \geq 1$ $\lvert \text{Vtx}_z \rvert < 10$ cm

.

Table 4.3: Event selection criteria for pp and p–Pb collisions. The same criteria were used for pp collisions at $\sqrt{s}$ = 7 TeV and at $\sqrt{s}$ = 2.76 TeV. For Pile-Up rejection, events with more than one primary vertex and with a minor fraction of SPD tracklets ($N_{\text{tracklets}}$) with respect to the number of SPD clusters (N_{SPDcls}) are removed using the AliRoot framework functions "IsPileUpFromSPD" and "IsSPDClusterVsTrackletBG", respectively. The definition of the parameters of the "IsPileupFromSPD" function can be found in [135].

HIJING

HIJING (Heavy Ion Jet INteraction Generator) [99] is an event generator used for multi-jets and particle production in nucleon-nucleon, nucleon-nucleus and nucleus-nucleus collisions. Based on the Lund FRITIOF [128, 129], DPM [130, 131] and pQCD models for hadrons interactions already implemented in Pythia [132–134], it is optimized to study the initial conditions of high-energy nuclear collisions. Therefore, it implements: multiple minijets production which include the initial and final-state radiation of partons, nuclear shadowing and a simple simulation of the energy loss of high-energy partons due to their interactions with the created hot and dense matter.

4.1.3 Event selection

The analyzed events in this thesis, were selected according to the criteria shown in Tab. 4.3 and explained below:

Alice Physics Selection (PS): It is a class of the AliRoot Framework used to select the so-called "collision candidate events". This kind of events are MB after background subtraction (beam-gas collisions). The information used in the PS is the one which has been re-calculated offline and, therefore, detector issues have been taken into account.

Pile-Up: The probability of an interaction (beam-beam collision) depends on the luminosity ($\mathcal{L}$) and on the LHC filling scheme [136]. The higher luminosity, the higher interaction rate (μ). Since at higher interaction rates the interval between collisions becomes shorter, it may occur that more than one interaction be recorded in the same event. Such events are known as Pile-Up and they are characterized by having various interaction vertices and by having a minor fraction of SPD tracklets[1] with respect to the number of SPD clusters (see Fig. 4.1) because the probability to form a tracklet which points to the main vertex becomes smaller if there are clusters from multiple interactions. As Pile-Up events affect negatively the analysis of the data

[1] A straight line pointing to the main vertex formed with two SPD clusters; one at the first layer and another at the second layer.

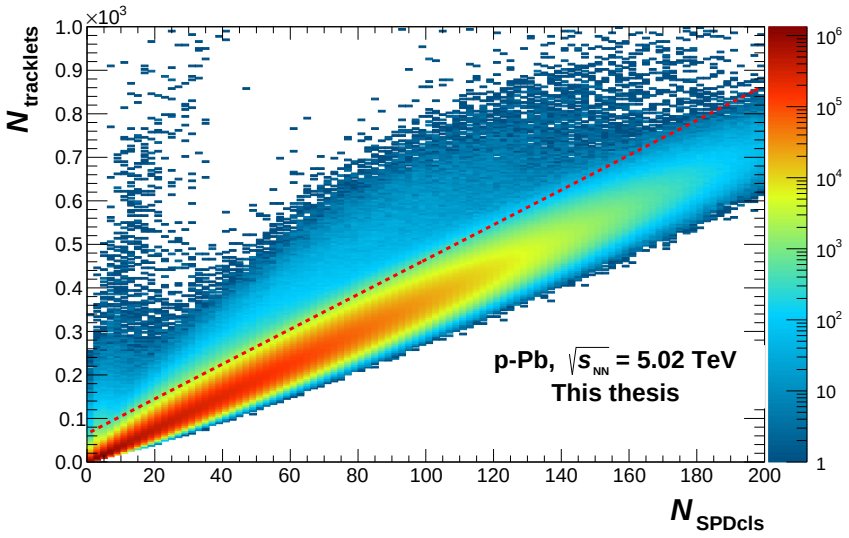

Figure 4.1: Number of tracklets ($N_{\text{tracklets}}$) as a function of number of SPD clusters (N_{SPDcls}). Events above the dashed red line are considered Pile-Up events and therefore are rejected in the event selection.

(they can lead to an unreal enhancement of the particle multiplicity), they are rejected in this thesis by discarding events with more than one reconstructed primary vertex (found using the SPD method described in [137]) and by applying a cut on the correlation between the number of SPD clusters and the number of SPD tracklets.

Primary vertex (Vtx): This condition requires events to have a reconstructed primary vertex with either SPD clusters (SPD_{cls}), global tracks[1] or TPC only tracks. It also requires at least one contributor used for vertex reconstruction to ensure its quality. Moreover, as there is a dependency between the geometrical acceptance (η) and the position of the primary vertex along the beam direction (Vtx_{Z}), a cut on Vtx_{Z} is applied to have a uniform acceptance.

4.1.4 Normalization

The number of events used for the calculation of the π^0 differential invariant yield spectrum (see Eq. (6.1)) is defined for pp collisions as:

$$N^{\text{pp}}_{\text{evt,norm}} = N_{\text{MB}_{\text{OR}},\text{Vtx},|\text{Vtx}_{\text{z}}|<10\text{ cm}} + \frac{N_{\text{MB}_{\text{OR}},\text{Vtx},|\text{Vtx}_{\text{z}}|<10\text{ cm}}}{N_{\text{MB}_{\text{OR}},\text{Vtx},|\text{Vtx}_{\text{z}}|<10\text{ cm}} + N_{\text{MB}_{\text{OR}},\text{Vtx},|\text{Vtx}_{\text{z}}|>10\text{ cm}}} N_{\text{MB}_{\text{OR}},\text{no Vtx}} \quad (4.1)$$

and for p–Pb collisions as:

$$N^{\text{p–Pb}}_{\text{evt,norm}} = N_{\text{MB}_{\text{AND}},\text{Vtx},|\text{Vtx}_{\text{z}}|<10\text{cm}} \quad (4.2)$$

where $N_{\text{MB}_{\text{OR}},\text{Vtx},|\text{Vtx}_{\text{z}}|<10\text{ cm}}$ and $N_{\text{MB}_{\text{AND}},\text{Vtx},|\text{Vtx}_{\text{z}}|<10\text{ cm}}$ correspond to the total number of events that passed the selection criteria summarized in Tab. 4.3 and $N_{\text{MB}_{\text{OR}},\text{no Vtx}}$ corresponds to num-

[1] A global track is the one reconstructed with global parameters. This means that it was reconstructed with the ITS+TPC detectors at least.

System	$\sqrt{s_{\mathrm{NN}}}$ (TeV)	$\sigma_{\mathrm{MB_{OR}}}/\sigma_{\mathrm{INEL}}$(%)	σ_{INEL} (mb)
pp	2.76	$88.1^{+5.9}_{-3.5}$	$62.8^{+2.4}_{-4.0} \pm 1.2$
pp	7	$85.2^{+6.2}_{-3.0}$	$73.2^{+2.0}_{4.6} \pm 2.6$

Table 4.4: Efficiencies of the $\mathrm{MB_{OR}}$ trigger and the inelastic cross sections (σ_{INEL}) for pp collisions at $\sqrt{s}$ = 2.76 TeV and at $\sqrt{s}$ = 7 TeV measured by ALICE [138] using van-der-Meer Scans.

ber of events without a reconstructed primary vertex. Due to the fact that in pp collisions the $N_{\mathrm{MB_{OR}, no\ Vtx}}$ was found to be significant, it was taken into account in the normalization factor. However, for p–Pb collisions this was found to be negligible ($\sim$ 1.3%) and therefore not considered.

Inelastic cross section

The inelastic cross section (σ_{INEL}) is an important observable that helps to characterize and understand phenomenologically the process observed in pp collisions [138]. The σ_{INEL} has two contributions: non-diffractive processes and diffractive processes. For the estimation of the σ_{INEL} was a requisite to measure the luminosity. The luminosity in pp collisions at $\sqrt{s}$ = 7 TeV and $\sqrt{s}$ = 2.76 TeV was computed using van-der-Meer scans [138]. The van-der-Meer scans studies were performed using a $\mathrm{MB_{AND}}$ trigger and the corresponding fractions $\mathrm{MB_{AND}}/\mathrm{MB_{OR}}$ were estimated using Monte Carlo simulations and real data. The portion of diffractive processes were obtained from a detailed study of the pseudorapidity distribution of the charged particles produced in a collision (see [138] for more details). The σ_{INEL} cross sections measured by ALICE are shown in Tab. 4.4 for pp collisions at the two energies under study.

4.2 Electron Selection

This selection consists on picking out the electrons originated at the main collision vertex from the whole set of reconstructed tracks. This task can be therefore divided into two: primary track selection and electron identification.

4.2.1 Primary track selection

For a better comparison the quantities that will be shown in this section (Figs. 4.2 to 4.4 and B.4) correspond to electron and positron candidates that contribute to the π^0 meson signal. Therefore, only those with $0.1 < M_{e^+e^-\gamma} < 0.145$ GeV/c were taken into account in the mentioned plots.

The cuts used for primary track selection in pp and p–Pb collisions are summarized in Tab. 4.5. The selection criteria used in pp collisions at $\sqrt{s}$ = 7 TeV and at $\sqrt{s}$ = 2.76 TeV correspond to the ALICE standard of 2010 for global tracks while the one used in p–Pb collisions correspond to the ALICE standard of 2011. The primary tracks are selected according to the distance of their closest point to the main interaction vertex in the transverse plane (DCA_{xy}) and in the axis along the beam direction (DCA_z). As the resolution of DCA_{xy} depends on p_{T} (see Fig. 3.7), the cut used for this distance is also p_{T} dependent. Moreover, a test with $\mathrm{DCA}_{xy} < 1$ cm for all

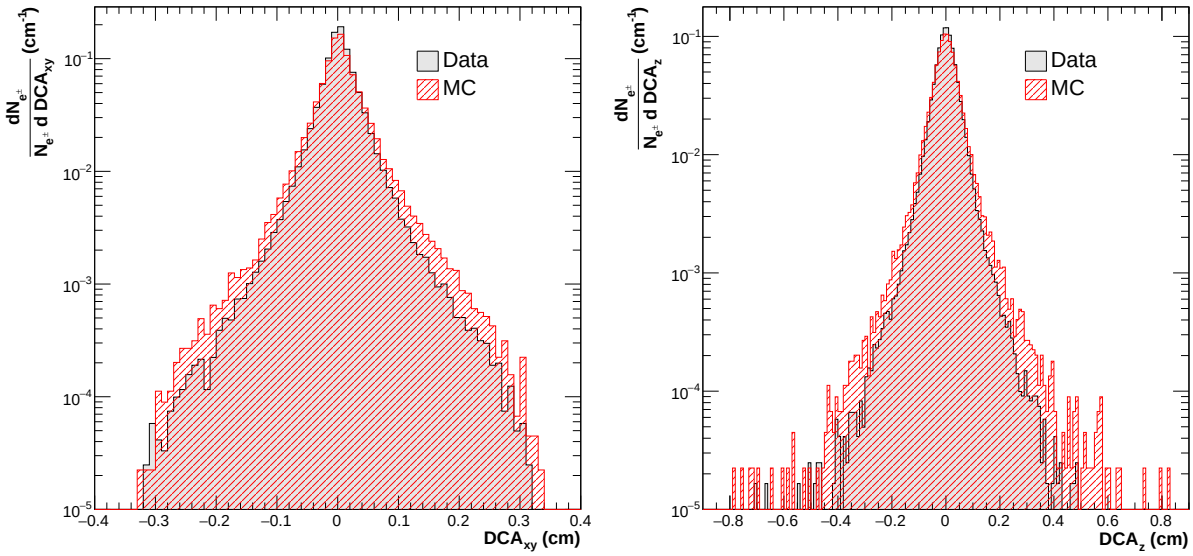

Figure 4.2: Distance of closest approach in the plane transverse to the beam direction (DCA$_{xy}$) (left) and along the beam direction (DCA$_z$) (right) in p–Pb collisions at $\sqrt{s_{\rm NN}}$ = 5.02 TeV for Monte Carlo simulations (red) and for data (grey).

tracks was carried out and not significant difference was observed. In any case, it is taken into account in the systematic errors. The DCA$_{xy}$ and DCA$_z$ distributions are shown in Fig. 4.2 for p–Pb collisions at $\sqrt{s_{\rm NN}}$ = 5.02 TeV for data and Monte Carlo (see Fig. B.4 for all systems). A good agreement between data and Monte Carlo is observed.

Given the small branching ratio of the π^0 into the Dalitz decay channel (see Tab. 2.1) and that a fraction of photons convert with the material of the beam pipe which is close to the main interaction (see Fig. 4.14), there is a sizable amount of conversion products (electrons) that passed the DCA cuts as if they were primary tracks. For this reason, tracks are required to have a least one cluster in either of the two layers of the SPD. Furthermore, the residual contamination is removed during the virtual photon reconstruction that will be explained in section 4.3.1.

Quality cuts

In addition to the cuts mentioned above, there are a set of them which are applied to assure the quality of the tracks. This means that the reconstructed track values of $p_{\rm T}$, $\mathrm{d}E/\mathrm{d}x$, etc., should be kept closer, as much as possible, to the real ones and should have a good resolution. The quality cuts are described as follows:

TPC refit and ITS refit: The track resolution can be improved by combining the information of various detectors during the reconstruction. For this reason, tracks are required to be reconstructed with the detectors ITS and TPC. The TOF and TRD detectors were not required due to the fact that the average $p_{\rm T}$ of the electrons from the π^0 Dalitz decay falls below the TOF threshold ($\sim$ 300 MeV) and due to the lower geometrical acceptance of the TRD at the time of this thesis.

	Values for pp	Values for p–Pb
Primary selection cuts		
DCA$_{xy}$	$< 0.0105 + 0.0350/p_{\mathrm{T}}^{1.1}$ cm	$< 0.0182 + 0.0350/p_{\mathrm{T}}^{1.01}$ cm
DCA$_z$	$<$ 2 cm	$<$ 2 cm
N_{SPDcls}	≥ 1	≥ 1
Quality cuts		
Require TPC refit	Yes	Yes
Require ITS refit	Yes	Yes
$N_{\mathrm{TPCcrossedRows}}$	–	> 70
$N^{\mathrm{found}}_{\mathrm{TPCcrossedRows}}/N^{\mathrm{findable}}_{\mathrm{TPCcrossedRows}}$	–	> 0.8
$N^{\mathrm{found}}_{\mathrm{TPCcls}}/N^{\mathrm{findable}}_{\mathrm{TPCcls}}$	> 0.35	–
χ^2_{TPCcls}	< 4	< 4
χ^2 TPC constrained Global	< 36	< 36
χ^2_{ITScls}	< 4	< 4
NoKinkDaughters	Yes	Yes
η	$\lvert\eta\rvert < 0.9$	$\lvert\eta\rvert < 0.9$
p_{T}	≥ 0.125 GeV/c	≥ 0.125 GeV/c
PID cuts (TPC $\mathrm{d}E/\mathrm{d}x$)		
Electron inclusion n_σ^{e} [min,max]	[-4,5]	[-4,5]
Pion rejection n_σ^{π} [min,max]	[-∞,+2] $p > 0.5$ GeV/c	[-∞,+2] $0.5 < p < 3.5$ GeV/c [-∞,-100] $p > 3.5$ GeV/c

Table 4.5: Primary track selection and quality cuts applied in pp and p–Pb collisions.

Kinks: Particle decays like $K^+ \rightarrow \mu^+\nu$ where only the charged particle can be detected, leave a pattern shape on the detector as if the particle has suffered a deviation in its trajectory. This decays are called kinks and tracks labeled as kink daughter are excluded from the analysis.

TPC clusters: The p_{T} resolution is related to the length of the track, which in turn is related to the number of cluters (N_{TPCcls}). However, the number of clusters depends on the cluster finding efficiency which can be affected by dead zones, gas composition of the TPC, etc. This implies that for some tracks the number of clusters do not reflect their length. Therefore, cutting just in N_{TPCcls} can lead to a diminution on the track quality. Nevertheless, given the geometry of the track, it is possible to estimate the total amount of clusters that can be attributed to it. These clusters are known as findable clusters ($N^{\mathrm{findable}}_{\mathrm{TPCcls}}$). Then, the ratio between the number of found clusters and the number of findable clusters ($N^{\mathrm{found}}_{\mathrm{TPCcls}}/N^{\mathrm{findable}}_{\mathrm{TPCcls}}$) gives the fraction of cluster loses. This fraction together with the N_{TPCcls} can be associated to the quality of the track. Therefore, in this thesis one requires a minimum N_{TPCcls} and minimum $N^{\mathrm{found}}_{\mathrm{TPCcls}}/N^{\mathrm{findable}}_{\mathrm{TPCcls}}$. In addition, a good χ^2 from the fit between the track and the clusters is also required.

It is important to mention that for p–Pb collisions instead of the number of clusters, the number

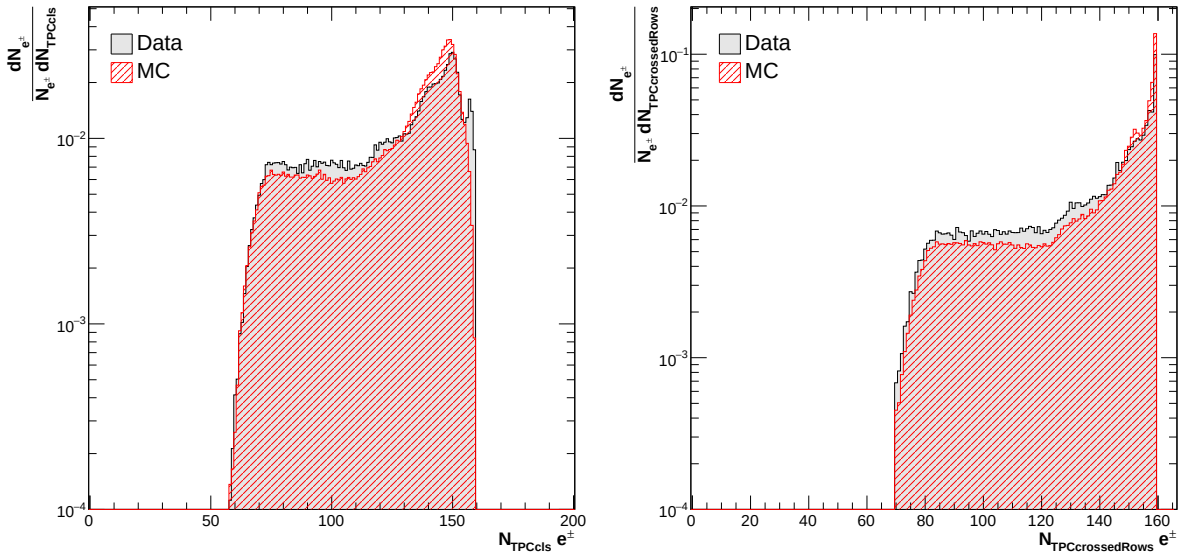

Figure 4.3: Number of TPC clusters (left) and number of TPC crossed rows (right) in p–Pb collisions at $\sqrt{s_{\mathrm{NN}}}$ = 5.02 TeV for Monte Carlo simulations (red) and for data (grey).

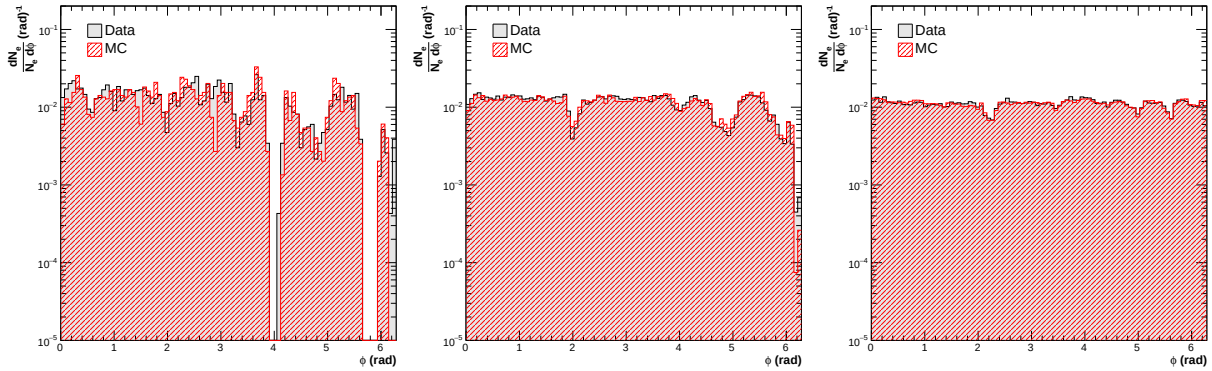

Figure 4.4: Azimuthal angle distribution of electron and positron candidates in pp collisions at $\sqrt{s}$ = 2.76 (left) and at $\sqrt{s}$ = 7 TeV (middle) and in p–Pb collisions at $\sqrt{s_{\mathrm{NN}}}$ = 5.02 TeV (right).

of TPC crossed row pads was required. This is due to fact that the latter is less sensitive to the cluster finding issues, and therefore, it is better reproduced in Monte Carlo simulations. The distribution of the N_{TPCcls} and the distribution of the $N_{TPCcrossedRows}$ are shown in Fig. 4.3 for p–Pb collisions.

ITS clusters: A good χ^2 of the fit between the track and the contributing ITS clusters is required.

4.2.2 Electron Identification

The electron sample can be obtained by combining the particle identification capabilities of the detectors TPC, TOF, TRD and EMCal. However, as it was mentioned previously, in order to collect the largest possible statistics of electrons from the π^0 Dalitz decay and in order to reduce as much as possible the efficiency issues related to the description of the detector responses in Monte Carlo simulations, only the particle identification provided by the TPC $\mathrm{d}E/\mathrm{d}x$ (see section 3.3.3) was used in this analysis. Anyway, a very pure sample of electrons is not essential

since one can exploit the π^0 properties (see section 2.1) to extract a cleaner sample.

To illustrate the particle identification, the specific energy loss in the TPC ($\mathrm{d}E/\mathrm{d}x$) as a function of momentum for all primary track candidates is shown in Fig. 4.5 (left panel). The $\mathrm{d}E/\mathrm{d}x$ for electrons (e), pions (π), kaons (K) and protons (p) is clearly visible in the plot. As it was explained in section 3.3.3, the $\mathrm{d}E/\mathrm{d}x$ for the mentioned particles can be parametrized by the Bethe-Bloch formula. This allows to identify tracks by computing the compatibility between the expected (given by the Bethe-Bloch formula) and the measured $\mathrm{d}E/\mathrm{d}x$ value. The compatibility is expressed in terms of standard deviations, $\mathrm{n}_{\sigma}^{\mathrm{par}}$ with par={e, K, μ, π, p}.

For the selection of the electron candidates two kind of cuts are applied: electron inclusion and pion rejection: The electron inclusion consists of accepting tracks with a measured $\mathrm{d}E/\mathrm{d}x$ compatible with the predicted $\mathrm{d}E/\mathrm{d}x$ for electrons ($\mathrm{n}_{\sigma}^{\mathrm{e}}$). On the other hand, the pion rejection cut consists of rejecting tracks with a measured $\mathrm{d}E/\mathrm{d}x$ compatible with the predicted $\mathrm{d}E/\mathrm{d}x$ for pions ($\mathrm{n}_{\sigma}^{\pi}$). The pion rejection cut is used to decrease the contamination of pions at low momenta. The values used for $n_{\sigma}^{e}[\mathrm{min},\mathrm{max}]$ and for $n_{\sigma}^{\pi}[\mathrm{min},\mathrm{max}]$ in pp and in p–Pb collisions are summarized in Tab. 4.5 (see PID cuts). Note that in p–Pb collisions, the pion rejection is applied in two momentum ranges being tighter at lower momenta. This is done in order to avoid affecting the efficiency of electrons at high momentum. For pp collisions, a test with a loose pion rejection cut for momentum larger than 3.5 GeV/c was performed. No significant impact on the effiency at high momentum was observed, anyway, it is taken into account in the systematic uncertainties (see Tab. 5.3 for the test values).

The n_{σ}^{e} as a function of momentum for tracks that passed the electron inclusion and pion rejection cuts is shown in Fig. 4.5 (right panel) for real data. The cut values used for electron inclusion and pion rejection are kept open in order to be less sensitive to a Monte Carlo issues. Moreover, the large contamination observed (mainly from pions, kaons and protons) can be drastically reduced by a cut on the invariant mass of the electron-positron pairs (see section 4.3.2). The $\mathrm{d}E/\mathrm{d}x$ versus momentum plots for pp collisions at the two energies under study can be seen in Fig. B.5.

4.2.3 Electron efficiency

The electron efficiency was calculated using the Monte Carlo simulations (MC) given in Tab. 4.2. The accurate measurement of the efficiency requires that MC simulations reproduce precisely the experimental data. As a cross-check, a compilation of figures comparing data and MC was produced and it is shown in appendix B. A good agreement is observed between data and MC for different quantities as: pseudorapidity distribution, ϕ distribution, p_{T} distribution, etc. Furthermore, it was shown in Fig. 2.4 that the $M_{\mathrm{e^+e^-}}$ of the electron-positron pair from the π^0 Dalitz decay is well reproduced in Pythia and HIJING generators, which are used for efficiency calculation and corrections.
The efficiency of the electron reconstruction is computed as follows:

$$\epsilon^{e} = \frac{N^{e}_{\mathrm{Rec}}\mathrm{within}|\eta| < 0.9(\text{ validated from } \pi^0 \to e^+e^+\gamma)}{N^{e}_{\mathrm{Gen}}\mathrm{within}|\eta| < 0.9(\text{ validated from } \pi^0 \to e^+e^+\gamma)} \tag{4.3}$$

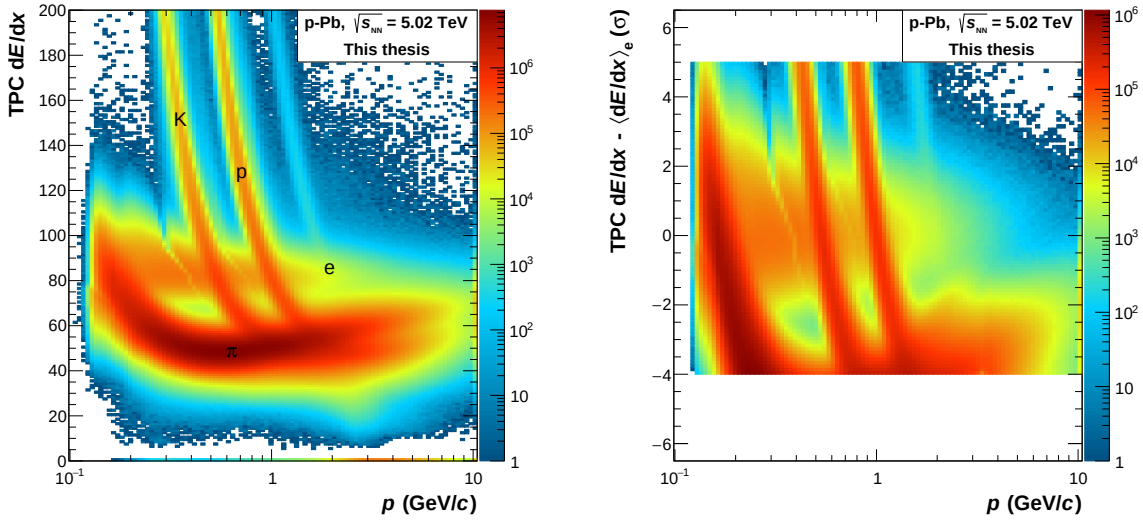

Figure 4.5: Specific energy loss in the TPC ($\mathrm{d}E/\mathrm{d}x$) as a function of momentum for all selected primary tracks (left). Compatibility to the parametrized Bethe-Bloch band for primary electron candidates as a function of momentum (right). The data correspond to p–Pb collisions at $\sqrt{s_{\mathrm{NN}}}$ = 5.02 TeV.

where N^{e}_{Rec} is the number of true reconstructed electrons within the acceptance and N^{e}_{Gen} is the number of electrons generated within the acceptance.
Figure 4.6 shows the efficiency of electrons and positrons from π^0 Dalitz decays for the three collision systems under study. The difference between the efficiencies at different collisions energies is due to the fact that the number of SPD sectors available was different for the three data taking periods (see Fig. 4.4). Since this effect is well reproduced in Monte Carlo no additional correction was needed. On the other hand, the electron efficiency shown in Fig. 4.6 was just used as a cross-check and it was not used for corrections on the π^0 meson production measurement.

4.3 Virtual Photon reconstruction

Virtual photons are reconstructed from all primary electron-positron pairs with both particles inside the acceptance. However, due to the fact that it is no possible to know the pairs that correspond to virtual photons in real data, all the combinations between electrons and positrons are carried out. This results in a large combinatorial background where only a small fraction of the pairs correspond to the desired sample.

Figure 4.7 shows that the two most significant sources of combinatorial background are (1) misidentified electrons (grey) and (2) photon conversions (red) that happen very close to the main vertex. The effect of these two sources of background on the π^0 meson reconstruction is the following: (1) increases the combinatorial background of the $\gamma^*\gamma$ invariant mass distribution and the computing time, making the π^0 signal extraction much harder and (2) represents the main source of background in the π^0 signal as most of the photon conversions come from the 2γ π^0 decay channel.

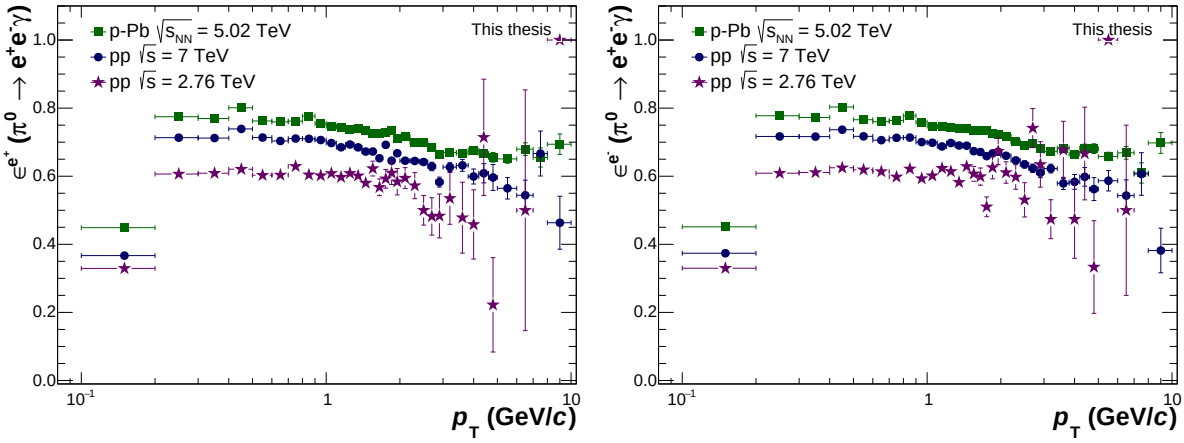

Figure 4.6: Electron efficiency (ϵ^e) as a function of p_{T} for positrons (left) and electrons (right) from π^0 Dalitz decays in pp collisions at $\sqrt{s}$ = 2.76 TeV and $\sqrt{s}$ = 7 TeV and in p–Pb collisions at $\sqrt{s_{\mathrm{NN}}}$ = 5.02 TeV. The ϵ^e has been computed using the Monte Carlo samples given in Tab. 4.2.

Cut	pp and p–Pb
$M_{\mathrm{e^+e^-}}$	< 0.015 GeV/c^2 if $p_{\mathrm{T}}^{e^+e^-\gamma} \leq 1$ GeV/c
	< 0.035 GeV/c^2 if $p_{\mathrm{T}}^{e^+e^-\gamma} > 1$ GeV/c
Ψ_{pair} triangular	$\Phi_0 = 0.0$, $\Phi_1 = 0.12$
Eqs. (4.8) and (4.9)	$\Psi_0 = 0.60$

Table 4.6: Summary of the values used for the $M_{\mathrm{e^+e^-}}$ cut and for the Ψ_{pair} triangular cut in pp and in p–Pb collisions. Φ_0, Φ_1 and Ψ_0 are the parameters of Eqs. (4.8) and (4.9).

To illustrate better how (2) can contaminate the π^0 signal, consider that the two photons from the $\pi^0 \to \gamma\gamma$ decay channel convert inside the central barrel acceptance. If one of them converts closely to the main interaction vertex (by interacting with the material of the beam pipe), it could be reconstructed as a virtual photon if both of its conversion products pass the selection criteria described in Tab. 4.5. If this is the case and if, in addition, the other photon passes the selection criteria for photons described in Tab. 4.7, one will have a $\gamma^*\gamma$-pair with both particles correlated by the same mother (π^0) and, therefore, their invariant mass will fall in the region of interest, the π^0 mass. Consequently, as one want to measured the π^0 meson production through its Dalitz decay channel exclusively, this represents a source of contamination which becomes important due to the large difference between the branching ratios of the two π^0 decay channels (see Tab. 2.1).

From the above reasons, the reduction of the combinatorial background and the rejection of the conversions becomes important. For this, methods based on the kinematic properties of the virtual photons from π^0 Dalitz decays and of photons, like $M_{\mathrm{e^+e^-}}$ and Ψ_{pair} are used. The two methods are described below and the cuts used in each of them are summarized in Tab. 4.6.

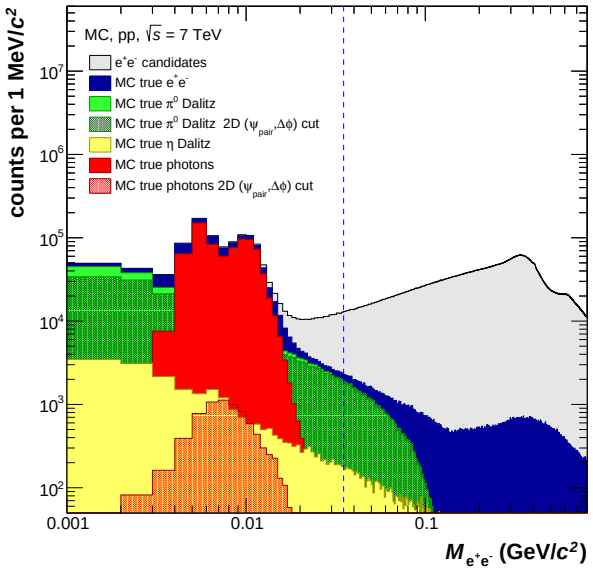

Figure 4.7: Invariant mass distribution of electron-positron candidates ($M_{\mathrm{e^+e^-}}$). The electron-positron pairs validated by MC as real electrons (blue), π^0 meson Dalitz decays (green), photon conversions (red) and η meson (yellow) are shown in the figure. The electron-positron pairs for π^0 meson Dalitz decays and conversion pairs after applying the Ψ_{pair} triangular cut (see Tab. 4.6) are also plotted. The dashed blue line shows the $M_{\mathrm{e^+e^-}}$ cut value for $p_{\mathrm{T}}^{e^+e^-\gamma} > 1$.

4.3.1 Rejection of conversions

The rejection of photon conversions is carried out by using the method described in [139]. This method is based on the effect of the magnetic field over the opening angle and the orientation in the space of the electron-positron pairs. Because of the zero mass property of photons, such effects on photons and virtual photons can be clearly differentiated, and therefore, they can be used to disentangle the two particles.

To illustrate how photons and virtual photons can be distinguished by their opening angle, the following two remarks should be considered. First, the magnetic field acts only in azimuthal direction since it is parallel to the beam direction. Second, electron-positron pairs from conversions have a small opening angle due to the zero mass property of photons while the pairs from virtual photons have a random opening angle as they proceed from a non-zero mass particle, π^0. Consequently, the contribution of the magnetic field to the opening angle of conversions in azimuthal direction (ϕ) will be dominant [139].

From the above, if one defines the $\Delta\phi$ angle as:

$$\Delta\phi = \phi(\mathrm{e}^+) - \phi(\mathrm{e}^-). \tag{4.4}$$

the $\Delta\phi$ distribution for photons will always have the same sign since the magnetic field deflects the electron and the positron in opposite directions. On the other hand, the $\Delta\phi$ distribution for virtual photons will be symmetric around zero as their ϕ angle is dominated by the mass of the π^0. The above is clearly visible in Fig. 4.9, which was obtained using Monte Carlo simulations

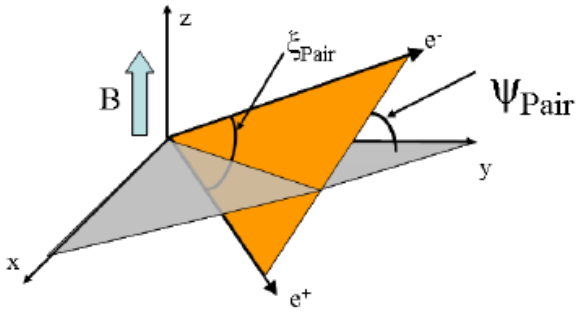

Figure 4.8: Illustration of the angle between the spanned up plane and the plane transverse to the magnetic field [139].

for pp collisions at $\sqrt{s} = 7$ TeV.

Now, it is the turn to explain how the orientation in the space of the pairs can be also used to distinguish conversions from virtual photons. For this, one should consider the following remarks. First, the magnetic field only affects the azimuthal angle, therefore, the polar angle (θ_0) will be always the same. Second, that the plane in which the two electrons (from photon conversions or virtual photos) spanned up is defined by their momentum vectors and the orientation of this plane in azimuthal and in polar direction is defined as follows [139]:

$$\xi_{\text{pair}} = \arccos\left(\frac{\vec{p_{\text{e}^-}} \cdot \vec{p_{\text{e}^+}}}{||\vec{p_{\text{e}^-}}|| \cdot ||\vec{p_{\text{e}^+}}||}\right) \tag{4.5}$$

Taking into account the first consideration and the small opening angle of photons, one could say that the contribution of θ_0 to ξ_{pair} angle will be smaller for conversions. This contribution can be obtained by measuring the angle between the plane transverse to beam direction (x-y) and the spanned up plane as it is shown in Fig. 4.8. This angle is known a Ψ_{pair} and it is defined as follows [139]:

$$\Delta\theta_0 = \theta_0(\text{e}^-) - \theta_0(\text{e}^+) \tag{4.6}$$

$$\Psi_{\text{pair}} = \arcsin \quad \frac{\Delta\theta}{\xi_{\text{pair}}} \tag{4.7}$$

Figure 4.9 shows the Ψ_{pair} distribution (right panel) for all electron-positron candidates (gray), true virtual photons (green) and true photons (red). As it can be seen in the figure, the Ψ_{pair} distribution of conversion is symmetric around zero contrasting with wider distribution for virtual photons.

Now, if one plots the Ψ_{pair} angle against the $\Delta\Phi$ angle as it is shown in Fig. 4.10 (right panel), one can see that it is possible to define a triangular cut (called Ψ_{pair} triangular cut) to reject conversion products in the virtual photons sample. The Ψ_{pair} triangular cut is defined as:

$$\phi_0 < \Delta\phi < \phi_1 \tag{4.8}$$

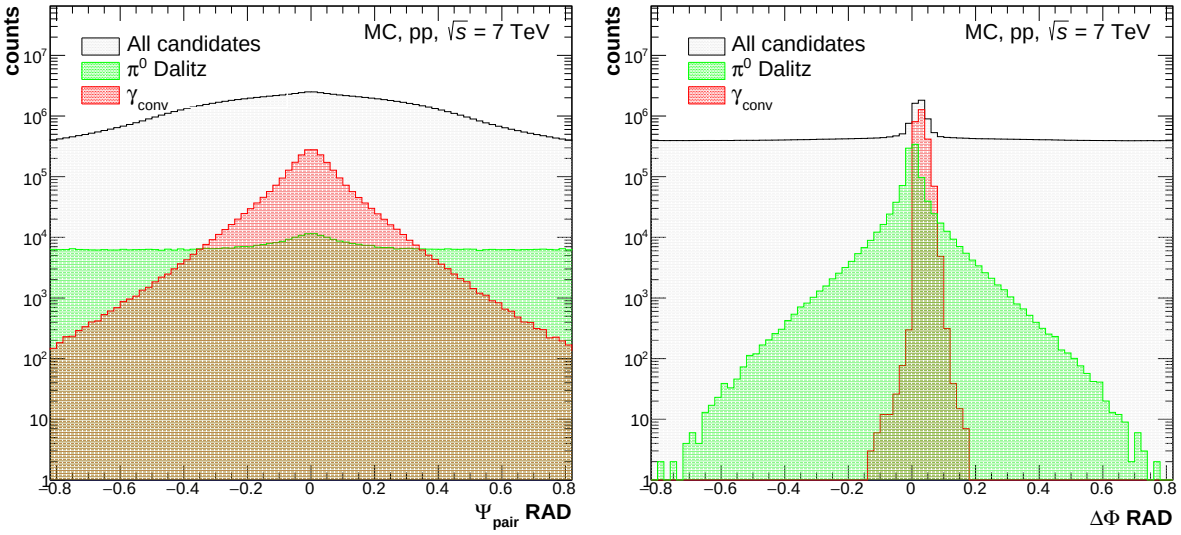

Figure 4.9: Ψ_{pair} angle (left) and $\Delta\phi$ (right) for all e^+e^- pairs candidates (gray), truth e^+e^- pairs from Dalitz (green) and e^+e^- from conversions (red).

$$|\Psi_{\text{pair}}| < (\Psi_0 - \frac{\Psi_0}{\Phi_1}\dot{\Delta}\phi) \tag{4.9}$$

where ϕ_0, ϕ_1 and Ψ_0 are the parameters of the cut. The values used in all systems under study are summarized in Tab. 4.6.

The efficiency of this cut was investigated using Monte Carlo simulations. Figure 4.10 (left panel) shows that the large contamination of conversions in pp collisions at $\sqrt{s}$ =7 TeV is reduced from $\sim$ 70 % to $\sim$ 3 %. The same behaviour was observed for pp collisions at $\sqrt{s}$ = 2.76 TeV and for p–Pb collisions. The remaining contamination will be subtracted at the time of the π^0 meson reconstruction and it is explained in section 5.4.2.

4.3.2 Reduction of the combinatorial background

One property of the electron-positron pairs from virtual photons of the π^0 Dalitz decay channel is that their invariant mass ($M_{e^+e^-}$) follow the Kroll-Wada formula (see Eq. (2.1)). Moreover, one can see in Fig. 4.7 that the maximum value of $M_{e^+e^-}$ for the truth π^0 Dalitz decays is the π^0 mass while the contamination is located at larger mass values. This allows to select the low mass region reducing the background while keeping most of the signal.

As most of the $M_{e^+e^-}$ signal from virtual photons is concentrated at a very low mass region (see Figs. 2.4 and 4.7), one can apply a cut further below of the π^0 mass, 35 MeV/c. Moreover, in order to improve the π^0 signal significance at p_{T} values below 1 GeV/c, the $M_{e^+e^-}$ cut in that p_{T} region is tighter, $\sim$ 15 MeV/c.

The $M_{e^+e^-}$ cut values for the three systems under study are summarized in Tab. 4.6. The effect of the $M_{e^+e^-}$ cut on the π^0 meson reconstruction efficiency is shown in Fig. 4.11. One can see that the efficiency for $p_{\text{T}} > 1$ GeV/c drops $\sim$ 18 % while for $p_{\text{T}} < 1$ GeV/c it falls $\sim$ 40 %. Although the effect of this cut on the efficiency is significant, specially at lower momenta, its

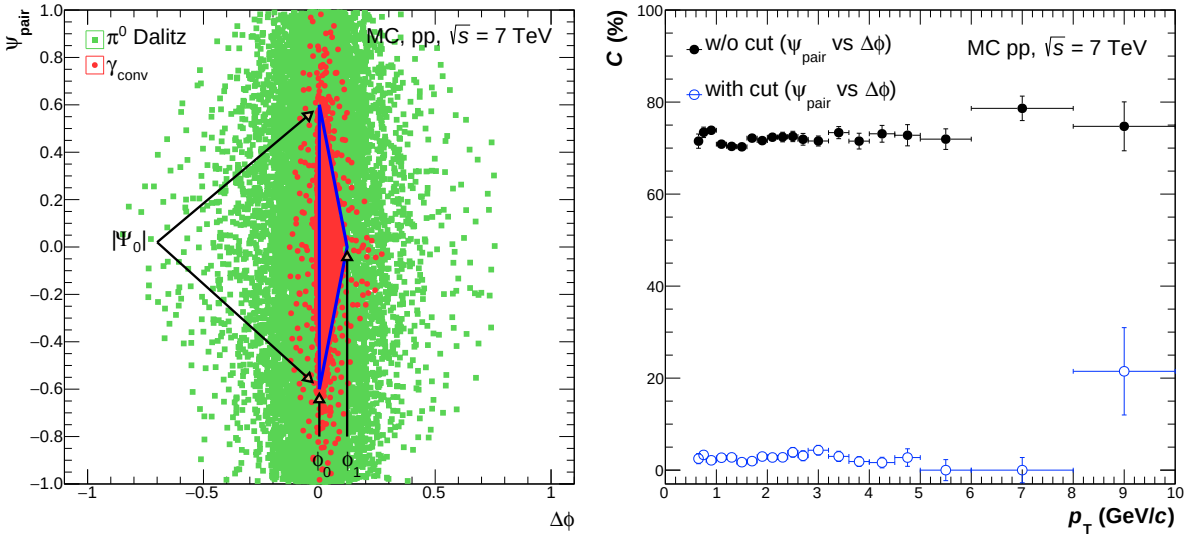

Figure 4.10: Illustration of the Ψ_{pair} triangular cut applied to reject electrons from conversions (right). Contamination fraction in the π^0 signal (C) computed using Eq. (5.6) (left). The contamination from conversion is substantially reduced with the Ψ_{pair} triangular cut.

implementation on the analysis is necessary otherwise a larger combinatorial background will lead to a lower significance affecting importantly the π^0 signal extraction.

4.4 Photon reconstruction

The ALICE detector has the capability to measure photons in three different ways: through the photon conversion into an electron-positron pair in the central barrel (see sections 3.2.3 and 3.2.4), using the PHOS detector (see section 3.2.7) and using EMCal detector (see section 3.2.8). In the slang of ALICE the three methods are known as Photon Conversion Method (PCM), PHOS and EMCal, respectively. The PCM method can reconstruct photons in a pseudo-rapidity range $|\eta| < 0.9$ and full azimuthal coverage $0 < \phi < 360°$ while the acceptances of the PHOS and EMCAL detectors were mentioned in sections 3.2.7 and 3.2.8, respectively. In this thesis photons are reconstructed using the PCM method which will be explained in detail in the following sections.

4.4.1 Photon Conversion Method (PCM)

The topology of a photon conversion can be described by the production of a secondary vertex with a positive track and negative track, forming a V^0 (see section 3.3.2). Therefore, photons that convert into an electron-positron pair in the ALICE central barrel are reconstructed using the two available V^0-finder algorithms: On-the-Fly and Off-line. As it was mentioned in section 3.3.2, the On-the-Fly V^0-finder algorithm is performed during the event reconstruction process, and therefore, it can use the information of the track reconstruction such as clusters to do extra track corrections like track trajectory, p_{T} resolution, etc. On the other hand, the offline algorithm is performed after full event reconstruction, and consequently, corrections to the track parameters are not longer possible. However, since the the offline algorithm does not depend on the track finding process it can be executed without a new event reconstruction. The On-the-Fly

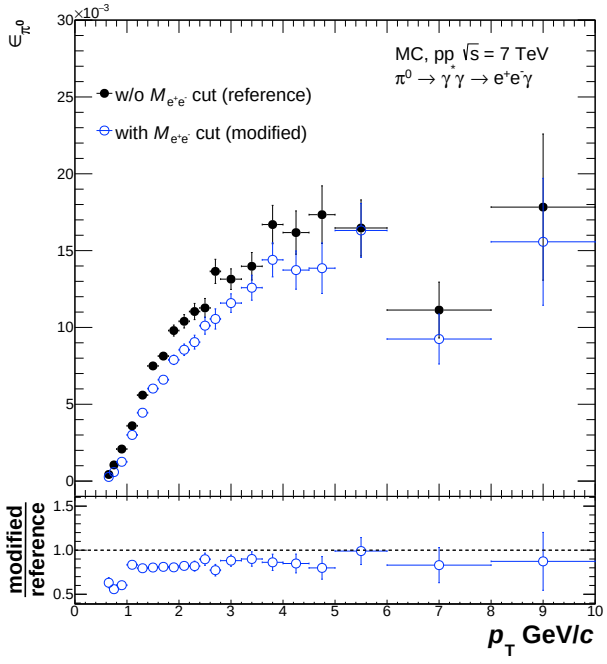

Figure 4.11: π^0 meson reconstruction efficiency for pp collisions at $\sqrt{s} = 7$ TeV. The black circles corresponds to the efficiency without the $M_{e^+e^-}$ cut. The blue open circles corresponds to the efficiency where $M_{e^+e^-}$ cut has been applied. The comparison of the efficiencies is shown in the bottom.

V^0-finder was used as a default in this thesis because of its higher efficiency. Nevertheless, the off-line V^0-finder was taken into account in the calculation of the material budget error [140].

Due to the small opening angle of photons, their conversion products fly through the space almost in the same direction as their photon mother does until the the magnetic field bend the tracks. Because of the above was not taken into account during the V^0 reconstruction, the photon conversion point was re-calculated in this thesis. The method used for this is described in more detail in [140, 141] and it basically consists on re-computing the conversion point under the assumption that the momenta of the two conversion products is parallel to the momentum of their photon mother.

The V^0 candidates sample given by the V^0-finder is composed by photons, K^0_S, Λ, $\bar{\Lambda}$ and combinatorial background. This can be seen in the Armenteros-Podolaski plot that was shown in Fig. 3.10. The idea of the photon selection is to extract the V^0's corresponding to photons from that sample. This implies to apply a set cuts related to the main features of photons as their two electron-positron legs, their zero mass and their small opening angle. Moreover, photons should proceed from the main interaction and should have a good quality. Therefore, the selection criteria can be divided into three categories: tracks and V^0 selection, electron selection and photon selection.

The cuts for the three categories used in pp and p–Pb collisions are summarized in Tab. 4.7 and they will be explained below.

Tracks and V^0 selection

In order to assure the quality of the V^0s, their two secondary tracks have to fullfill similar cuts as the quality cuts used in the primary tracks selection (see section 4.2.1). This includes $N_{\text{TPCcls}}^{\text{found}}/N_{\text{TPCcls}}^{\text{findable}}$, NoKinkDaughters and a minimum p_{T}. Unlike primary tracks selection, here, the ITS refit is not required because photons that convert on the TPC do not leave signals on the ITS, and therefore, there will be a dramatical reduction of the statistics.

In addition to the above cuts, there is a cut on pseudorapidity (η) to selects V^0's reconstructed well inside the acceptance of the ALICE central barrel. The η is related to the orientation of the particle in the detector relative to the beam axis (z). However, as for secondary tracks their starting point is not taken into account for the η calculation, there will be some V^0's that will pass the η cut even if they are outside of the acceptance. For this reason, an extra cut which is equivalent to cutting on η as if the conversion point were located at the nominal center position of the ALICE detector (0,0,0) is used. This cut is called "Line Cut" and it is defined as:

$$R_{\text{conv}} < |Z_{\text{conv}}| * Z_{\text{RSlope}} - Z_0 \tag{4.10}$$

where $Z_{\text{RSlope}} = \tan(2 * \arctan(\exp(-\eta)))$ and $Z_0 = 7$ cm.

Furthermore, the conversion radius (R_{conv}) is required to be between a given interval so that one can reject electron-positron pairs from π^0 Dalitz decays at small conversion radii and to assure the reconstruction of the two tracks in the ALICE central barrel with better accuracy.

Electron selection

The specific energy loss (TPC $\mathrm{d}E/\mathrm{d}x$) as a function of momentum for positive and negative tracks of photon candidates is shown in Fig. 4.12 (left). The purity of the photon candidates sample can be improved by requiring that the two tracks of the photons to be electrons. Like in primary electrons (see section 4.2.2), electron inclusion and pion rejection cuts are also applied using the TPC $\mathrm{d}E/\mathrm{d}x$. The values used in pp and in p–Pb collisions are summarized in Tab. 4.7. The number of standard deviations (n_σ^e) to the predicted $\mathrm{d}E/\mathrm{d}x$ given by the parametrized Bethe-Bloch band for electrons after PID cuts is shown in Fig. 4.12 (right) for p–Pb collisions at $\sqrt{s_{\text{NN}}}$ = 5.02 TeV. The contamination from pions, kaons and protons can be reduced by applying cuts related to the properties of photons on the V^0 candidates sample as it was mentioned previously. This cuts will be described below.

Photon selection

Although the electron selection reduces the contamination of $\mathrm{K}^0_{\mathrm{S}}$s, Λs and $\bar{\Lambda}$s significantly. There is still a remaining background that could be reduced by a applying a cut on the q_{T} of the Armenteros-Podalaski plot. Furthermore, as the photon candidates are reconstructed using an AliRoot class based on the Kalman Filtering algorithm, the AliKFParticle [142], some constrains related to the photon properties as the zero mass and the small opening angle can be imposed. The resulting χ^2_γ/ndf from the Kalman Filtering is considered as the quality of the photon and therefore, a good χ^2_γ/ndf is required. Furthermore, photons are required to be produced at the main interaction point. For this reason the Cosine of the pointing angle that was defined in

Cut	Value
Track and V^0 selection	
V^0 finder	On-the-Fly
$N^{\text{found}}_{\text{TPCcls}}/N^{\text{findable}}_{\text{TPCcls}}$	$>= 0.6$
$p_{\text{T,e}}$	$p_{\text{T,e}} > 0.05$ GeV/c
R_{conv}	$5 < R_{\text{conv}} < 180$ cm
Z_{conv}	$Z_{\text{conv}} < 1000$ cm
η	$\lvert\eta\rvert < 0.9$
Line cut	$R_{\text{conv}} < \lvert Z_{\text{conv}}\rvert * Z_{\text{RSlope}} - Z_0$
	$Z_{\text{RSlope}} = \tan(2 * \arctan(\exp(-\eta)))$
	$Z_0 = 7$ cm
Photon selection	
χ^2_γ/ndf	$<= 30$ ($<= 20$ for pp)
q_{T}	$q_{\text{T}} <= 0.15$ GeV/c
$p_{T,\gamma}$	$p_{T,\gamma} > 0.02$ GeV/c
Cosine of pointing angle	> -1
PID cuts (TPC $\mathrm{d}E/\mathrm{d}x$)	
n^e_σ [min,max]	[-4, 5]
n^π_σ [min,max]	[-∞,+2] $0.5 < p < 3.5$ GeV/c
	[-∞,+0.5] $p > 3.5$ GeV/c

Table 4.7: List of the cuts applied in the photon reconstruction. The same criteria were used in pp and p–Pb collisions.

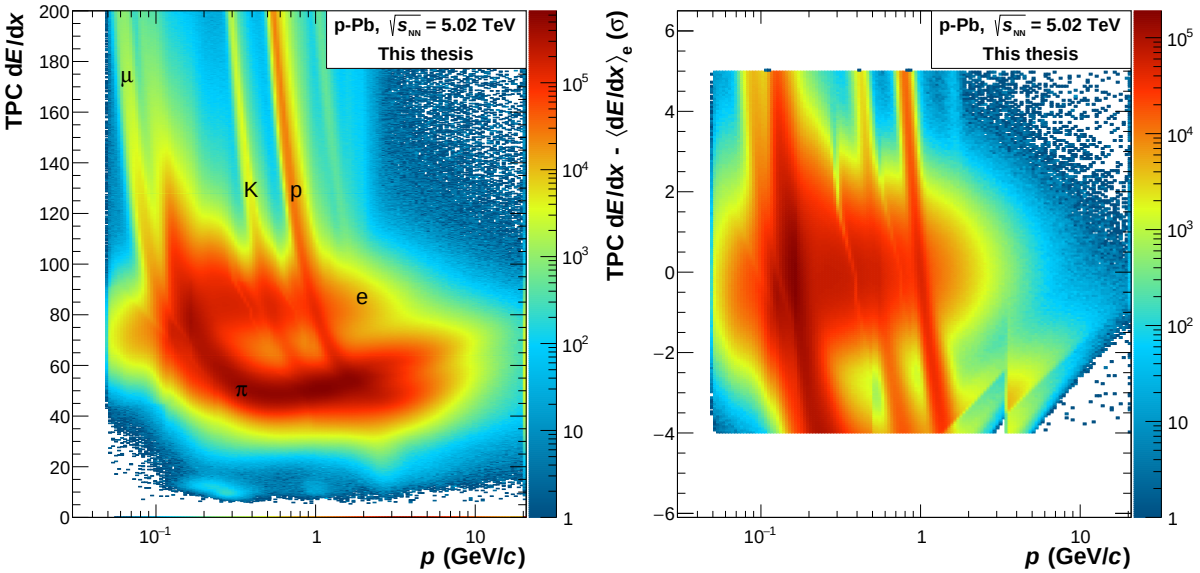

Figure 4.12: Specific energy loss (TPC $\mathrm{d}E/\mathrm{d}x$) as a function of momentum for secondary electron candidates before PID cuts (left). Number of standard deviations (n^e_σ) of the measured $\mathrm{d}E/\mathrm{d}x$ to the parametrized Bethe-Bloch band for secondary electron candidates after PID cuts (right). The data correspond to p–Pb collisions at $\sqrt{s_{\text{NN}}} = 5.02$ TeV.

section 3.3.2 is taken into account. All the photon selection cuts used in pp and in p–Pb are summarized in Tab. 4.7.

4.5 Photon efficiency

The efficiency of the photon reconstruction is obtained as:

$$\epsilon^{\gamma_{conv}} = \frac{N_{Rec}^{\gamma_{conv}} \text{within acceptance}}{N_{Gen}^{\gamma_{conv}} \text{within acceptance}} \tag{4.11}$$

where $N_{Rec}^{\gamma_{conv}}$ is the number of true reconstructed photons and $N_{Gen}^{\gamma_{conv}}$ is the number of true converted photons generated by Monte Carlo. Both inside the acceptance which was defined in section 4.4.1. The photon efficiency as a function of p_{T} and as a function of the conversion radius (R_{conv}) for the three systems under study with open cuts and the applied cuts are shown in Fig. 4.13. The photon efficiency as a function of p_{T} for pp collisions at $\sqrt{s}$ = 2.76 TeV is slightly lower than the rest. This is due tho absence of SDD detector during the data taking at that energy. The efficiency as a function of R_{conv} is clearly lower for pp collisions at $\sqrt{s}$ = 7 TeV in the zone of the TPC drift gas (90 < R_{conv} < 180 cm, see Figs. 4.14b and 4.14c). The larger efficiency was the result of including 1 pad clusters in the tracking and $\mathrm{d}E/\mathrm{d}x$ calculation from period LHC10d on.

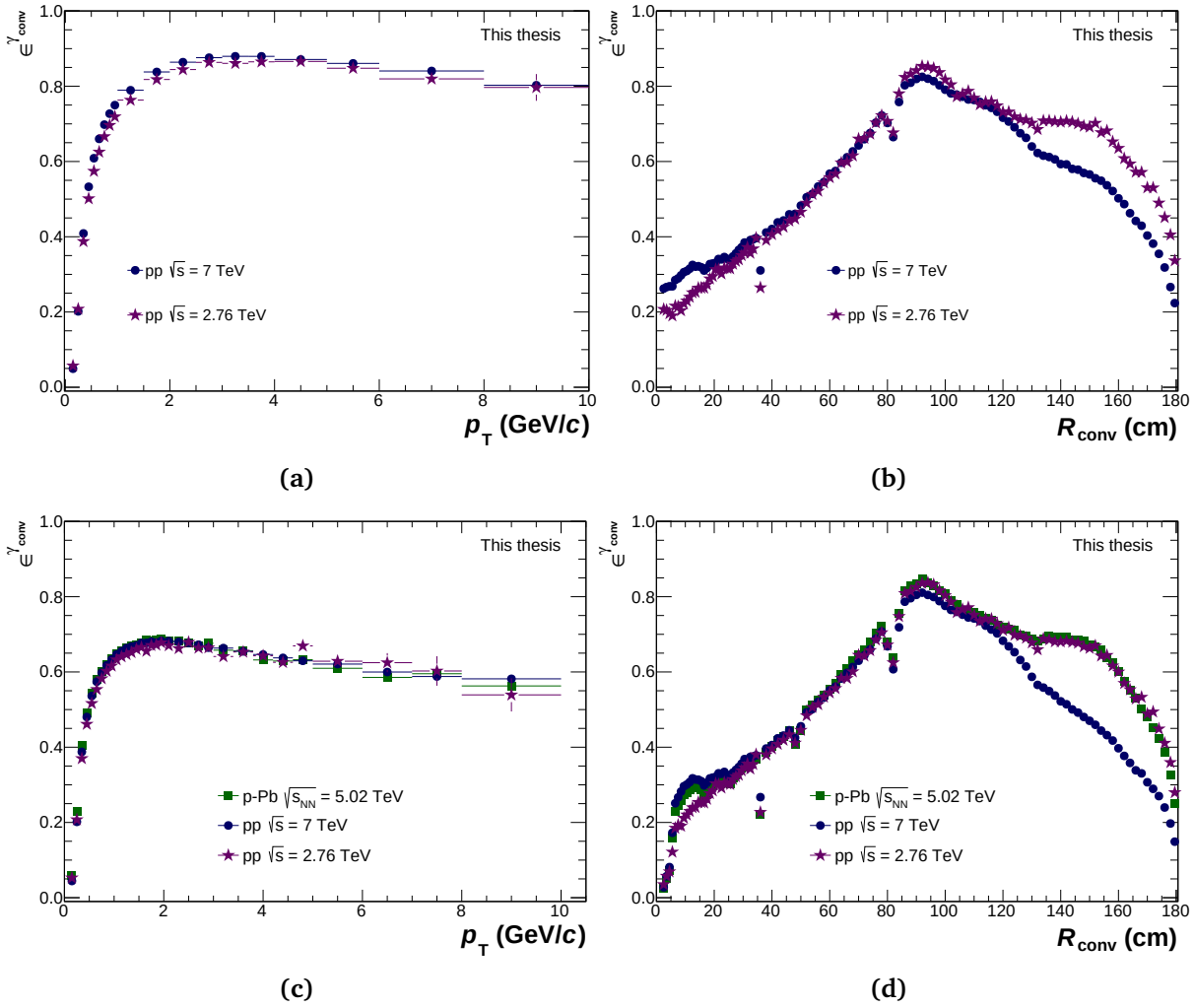

Figure 4.13: (Top) Efficiency versus p_{T} (left) and versus R_{conv} (right) in pp collisions at $\sqrt{s}$ = 2.76 TeV and $\sqrt{s}$ = 7 TeV before photon selection cuts. (Bottom) Efficiency versus p_{T} (left) and versus R_{conv} (right) in pp collisions at $\sqrt{s}$ = 2.76 TeV and $\sqrt{s}$ = 7 TeV and in p–Pb collisions at $\sqrt{s_{\mathrm{NN}}}$ = 5.02 TeV after photon selection cuts. The absence of the SDD detector in pp collisions at $\sqrt{s}$ = 2.76 TeV leading to a lower efficiency.

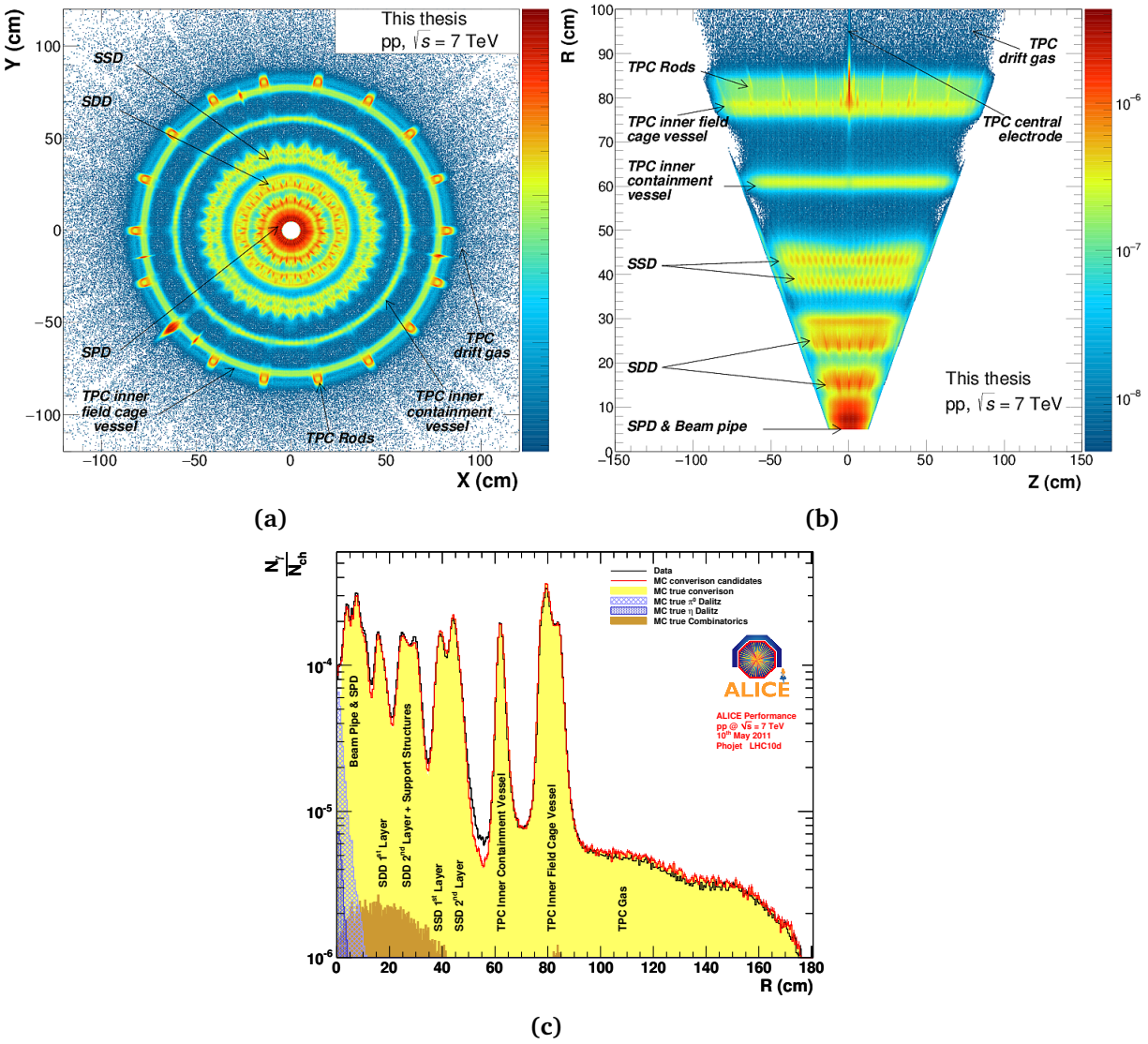

Figure 4.14: (a) Y versus X of the conversion point of gammas. (b) Radius versus Z of the conversion point of gammas. (c) Radius of the conversion point [143].

Chapter 5

π^0 meson analysis

In this chapter a detailed description of all necessary steps in the π^0 analysis from the raw yield extraction until obtaining the π^0 differential invariant yield will be given.

5.1 π^0 meson reconstruction

The π^0 meson is reconstructed by computing the invariant mass of its decay products ($\pi^0 \rightarrow \gamma^*\gamma \rightarrow e^+e^-\gamma$). The invariant mass will be equivalent to the rest mass of the π^0 with an additional width due to the experimental resolution. As it is not possible to distinguish the true $\gamma^*\gamma$-pair from a π^0 meson in real data, the invariant mass is calculated combining all reconstructed virtual photons (γ^*) with all reconstructed real photons (γ) candidates. As a result, an invariant mass distribution composed by correlated and uncorrelated pairs is obtained. The invariant of the $\gamma^*\gamma$ pair is defined as follows:

$$M^2 = (E_\gamma + E_{\gamma^*})^2 - \left\|p_\gamma + p_{\gamma^*}\right\|^2 = \underbrace{{m_\gamma}^2}_{0} + {m_{\gamma^*}}^2 + 2(E_\gamma \cdot E_{\gamma^*} - p_\gamma \cdot p_{\gamma^*}) \tag{5.1}$$

where E_{γ^*} and E_γ represent the energy and p_{γ^*} and p_γ represent the momenta of γ^* and γ, respectively. Figure 5.1 shows an example of invariant mass distribution (black line) of $\gamma^*\gamma$-pairs for pp collisions at $\sqrt{s}$ = 7 TeV (left panel) and for p–Pb collisions at $\sqrt{s_{\rm NN}}$ =5.02 TeV (right panel) where a clear peak at the rest mass of the π^0 is observed. The peak is not symmetric due to the electron bremsstrahlung and extends to lower invariant mass values. The invariant mass distribution plots in all $p_{\rm T}$ bins and for all systems are shown in Figs. C.1 to C.3.

5.2 Combinatorial background estimation

The combinatorial background comes mainly from uncorrelated $\gamma^*\gamma$-pairs. In this thesis the combinatorial background was estimated using the mixed event technique [144]. In this technique photons and virtual photons from different events are paired in order to avoid correlations, and therefore, the uncorrelated combinatorial background can be estimated.

The combinatorial background is better reproduced when events with similar photon multiplicity (N_γ) or with similar charged particle multiplicity ($N_{\rm ch}$) and within the same range in the Z vertex coordinate ($\rm Vtx_Z$) are selected. For this reason, a pool of γ's was created defining bin

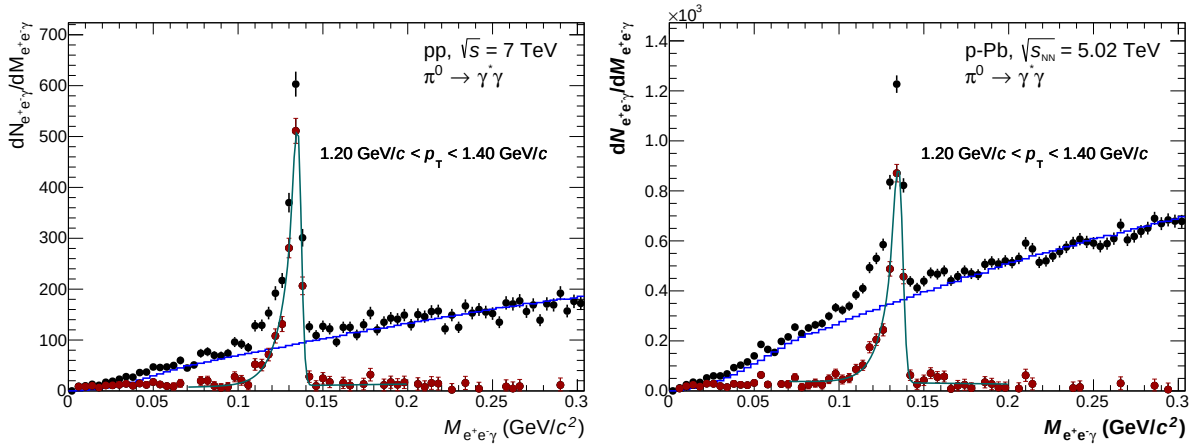

Figure 5.1: Invariant mass distribution (black line) of $\gamma\gamma^*$ ($e^+e^-\gamma$) for pp collisions at $\sqrt{s}$ = 7 TeV (left) and p–Pb collisions at $\sqrt{s_{\rm NN}}$ = 5.02 TeV (right). The blue line corresponds to the estimated combinatorial background using the mixed event technique. The red points represent the signal after combinatorial background subtraction. The green line corresponds to the fit of the π^0 peak after the combinatorial background subtraction using Eq. (5.2).

classes according to N_γ or to $N_{\rm ch}$ and Vtx$_{\rm Z}$. The classes defined for pp collisions and p–Pb collisions are described in Tab. 5.1.

In each event, the reconstructed γ^*'s are combined with reconstructed γ's from previous events with the same bin class ($N_{\rm ch}$(N_γ),Vtx$_{\rm Z}$) as the current one. Afterwards, the reconstructed γ's of the current event are stored in the corresponding bin class of the pool. This is done using the FIFO technique (First in, First out). The maximum number of γ's that can be stored in each bin is set to 80. This number was set larger enough in order to have a good statistical precision in the mixed event background calculation. Moreover, the effect of the size of pool of γ^*'s on the combinatorial background estimation was studied and included it in the systematic errors.

Referring to the bin classes, no significant difference was found in the combinatorial background calculation when used either $N_{\rm ch}$ or N_γ. However, combinatorial background based on $N_{\rm ch}$ was taken as a default in this thesis. Nevertheless, the difference between the two methods was also taken as source of systematic error.

Once the combinatorial background spectrum is obtained, the next step is to normalize it to the $\gamma^*\gamma$ spectrum obtained in the real event. The normalization factor is calculated by integrating the two spectra in a region where the π^0 signal is negligible. The normalization can be done either to the left side or to the right side of the π^0 peak. The default normalization region is chosen to the right side of the π^0 peak to avoid the long tail due the electron bremsstrahlung. The same integration windows are taken for pp collisions and p–Pb collisions (see Tab. 5.2). The difference between the two normalization regions (left and right) was taken into account in the systematic error of Yield extraction (see section 5.5).

The mixed event combinatorial background after normalization in pp collisions at $\sqrt{s}$ = 7 TeV and in p–Pb collisions at $\sqrt{s_{\rm NN}}$ = 5.02 TeV can be seen in Fig. 5.1 (blue line). As it can be seen in the figure, the mixed event technique reproduces the shape of the combinatorial background nicely in both systems. The same result is obtained in pp collisions at $\sqrt{s}$ = 2.76 TeV (see Fig. C.3

Class	Bin	pp	p–Pb
N_γ	1	2	2
	2	3	3
	3	4	4
	4	5	6
	5	> 5	> 6
N_{ch}	1	0 - 9	0 - 7
	2	10 - 16	8 - 16
	3	17 - 27	17 - 29
	4	28 - 200	30 - 500
$\mathrm{Vtx_Z}$	1	-50.00 - -3.375	-50.00 - -5.85
	2	-3.375 - -1.605	-5.85 - -3.35
	3	-1.605 - -0.225	-3.35 - -1.15
	4	-0.225 - 1.065	-1.15 - 0.85
	5	1.065 - 2.445	0.85 - 2.95
	6	2.445 - 4.245	2.95 - 5.55
	7	4.245 - 50	5.55 - 50.00

Table 5.1: Definition of the minimum bias event mixed classes for pp collisions at $\sqrt{s}$ = 7 TeV and $\sqrt{s}$ = 2.76 TeV and for p–Pb collisions at $\sqrt{s_{\mathrm{NN}}}$ = 5.02 TeV.

(top)). The combinatorial background estimated for each bin of p_{T} can be seen in the top panel of Figs. C.1 to C.3 for the three systems under study.

5.3 Signal Extraction

After the combinatorial background subtraction, the π^0 peak is fitted (see Fig. 5.1) using a Gaussian function with an exponential tail to take into account electron (positron) energy loss due to bremsstrahlung [145]. In addition, a linear function is included to take into account a possible remaining background. The fit function is defined as:

$$\frac{\mathrm{d}N_{e^+e^-\gamma}}{\mathrm{d}M_{e^+e^-\gamma}} = A \cdot \quad G(M_{\gamma^*\gamma}) + \exp \quad \frac{M_{\gamma^*\gamma} - M_{\pi^0}}{\lambda} \quad (1 - G(M_{\gamma^*\gamma}))\theta(M_{\pi^0} - M_{\gamma^*\gamma}) \quad + b + c \cdot M_{\gamma^*\gamma} \tag{5.2}$$

where

$$G = \exp \quad -0.5 \quad \frac{M_{\gamma^*\gamma} - M_{\pi^0}}{\sigma_{M_{\gamma^*\gamma}}} \quad ^2 \tag{5.3}$$

The parameter M_{π^0} is the π^0 peak position and it is taken as the measured π^0 mass, $\sigma_{M_{\gamma^*\gamma}}$ corresponds to the width of the π^0 mass and b and c are the parameters of the linear function. The λ parameter corresponds to the inverse slope of the exponential function. The effect of the exponential function at the right side of the π^0 peak is vanished by the heavyside step function $\theta(M_{\pi^0} - M_{\gamma^*\gamma})$. Figure 5.1 shows a nice fit (green line) to the π^0 peak after background subtraction (red dots). Additionally, the fits obtained in each bin of p_{T} are shown in the bottom panel

	π^0
Normalization window	
Right	(0.17,0.3) GeV/c^2
Left	(0.05,0.08) GeV/c^2
Integration range	
Standard	(M_{π^0}-0.035,M_{π^0}+0.010) GeV/c^2
Narrow	(M_{π^0}-0.015,M_{π^0}+0.005) GeV/c^2
Wide	(M_{π^0}-0.055,M_{π^0}+0.025) GeV/c^2

Table 5.2: Compilation of the mass range regions used for the normalization of the combinatorial mixed event background to the same event background and for the π^0 peak integration.

of Figs. C.1 to C.3 for the three systems under study.

The π^0 peak position (M_{π^0}) extracted from the fit is used as a reference for the integration window range. In order to have a good agreement between Data and Monte Carlo, an additional smearing for the real photon is applied in the Monte Carlo. In the smearing procedure, each of the momentum components is multiplied by $(1+\sigma)p_{x,y,z}$, where $\sigma = \sqrt{\sigma_0^2 + \sigma_1^2 \cdot p^2}$. The parameters are the same as in [146], $\sigma_0 = 0.011$ GeV/c and $\sigma_1 = 0.007$. The π^0 peak position (M_{π^0}) and peak width (taken as FWHM/2.35 to convert to an equivalent σ) versus transverse momentum extracted from the data compared to the values obtained in Monte Carlo simulations are shown in Figs. 5.2 and 5.3, respectively. The plots show a good agreement between data and Monte Carlo within the statistical errors.

The raw yield of the π^0 ($N^{\pi^0}_{\rm RAW}$) is computed by integrating the π^0 signal after background subtraction within the integration windows given in Tab. 5.2. The integration windows are estimated around the π^0 peak given by the gaussian fit. However, due to bremsstrahlung tail the integration window is asymmetric around the π^0 mass. Moreover, the possible remaining background estimated from the linear fit is subtracted from the integral.

Additionally, the π^0 peak is integrated by using a narrow and wide integration window to estimate the systematic error due the signal extraction. The obtained $N^{\pi^0}_{\rm RAW}$ is shown for the three analysis in Fig. 5.5.

5.4 Monte Carlo Studies

Monte Carlo simulations using event generators like Pythia 6.4, Pythia 8.1, Phojet, and HIJING (see Tab. 4.2) are used in order to optimize the software, and to extract the acceptance; the reconstruction efficiency; and the contamination from the $\pi^0 \to \gamma\gamma$ channel corresponding to the analysis cuts used for pp collisions at $\sqrt{s}$ = 2.76, 7 TeV and for p–Pb collisions at $\sqrt{s_{\rm NN}}$ = 5.02 TeV.

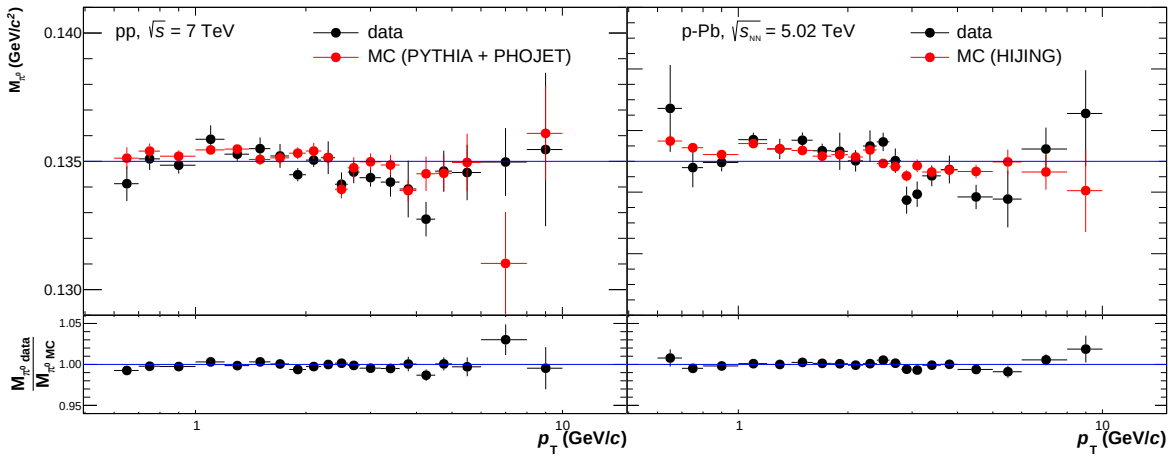

Figure 5.2: π^0 peak position extracted in data (black) compared to the one obtained in Monte Carlo simulations (red) for pp collisions at $\sqrt{s}$ = 7 TeV (left) and for p–Pb collisions at $\sqrt{s_{\rm NN}}$ = 5.02 TeV (right).

5.4.1 π^0 acceptance and efficiency

The geometrical acceptance A_{π^0} is defined as the ratio of π^0 mesons within $|y| < y_{\rm max}$, whose daughter particles are within the fiducial acceptance ($|\eta| < 0.9$), over all π^0 mesons generated in the same rapidity window:

$$A_{\pi^0} = \frac{N_{\pi^0,|y|<y_{\rm max}} \text{ with the daughter particles within } |\eta_{\gamma,e^+,e^-}| < 0.9}{N_{\pi^0,|y|<y_{\rm max}}} \tag{5.4}$$

The efficiency of the π^0 meson is defined as:

$$\epsilon_{\text{reco, }\pi^0} = \frac{\text{verified } N_{\pi^0,\text{rec}}\ (p_{\text{T, rec}})}{N_{\pi^0,|y|<y_{\rm max}} \text{ with the daughter particles within } |\eta_{\gamma,e^+,e^-}| < 0.9 (p_{\text{T, MC}})} \tag{5.5}$$

The π^0 acceptance and the π^0 efficiency as a function of the transverse momentum are shown in Fig. 5.4 for pp collisions at $\sqrt{s}$ = 7 TeV and at $\sqrt{s}$ = 2.76 TeV and for p–Pb collisions at $\sqrt{s_{\rm NN}}$ = 5.02 TeV. The difference observed in the three systems under study is related to the efficiency of the SPD detector (as already observed in the primary electron (positron) and photon efficiencies see Figs. 4.6 and 4.13). In pp collisions at $\sqrt{s}$ = 7 TeV the efficiency for periods LHC10b and LHC10c is different to the periods LHC10d and LHC10e affecting the reconstruction efficiency of primary electron-positron pairs (see section 4.2) because some changes were introduced in the track reconstruction algorithm. For this reason the efficiency used for corrections was computed by merging the two different efficiencies with weights given as in data. For p–Pb collisions, a Monte Carlo simulation using HIJING with modified branching ratios into the Dalitz decay channel Br($\pi^0 \to e^+e^-\gamma$) = 0.1 and $\gamma\gamma$ channel Br($\pi^0 \to \gamma\gamma$) = 0.9 was used in order to reduce the statistical errors with a reasonable computing time.

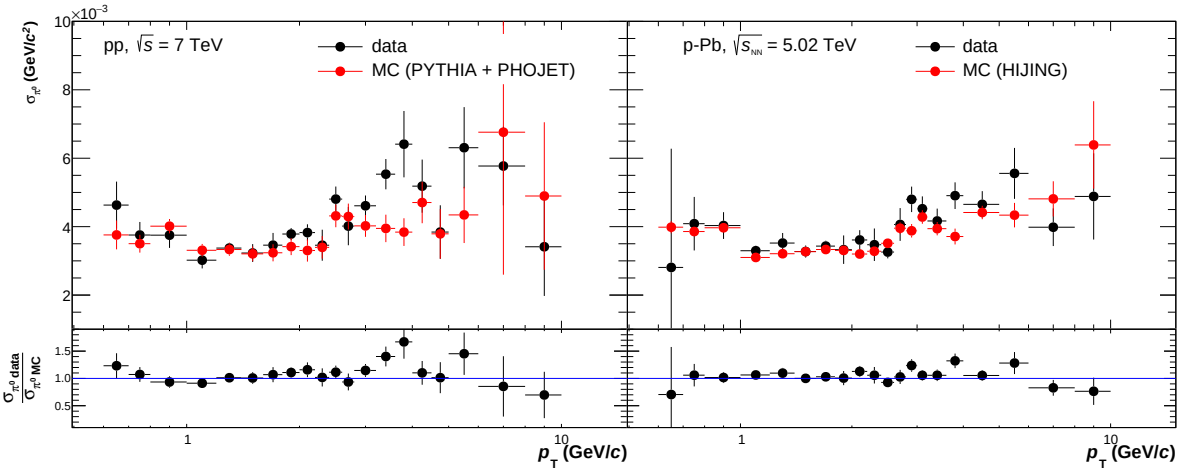

Figure 5.3: σ_{π^0} of the π^0 peak for data (black) and for Monte Carlo simulations (red) for pp collisions at $\sqrt{s}$ = 7 TeV (left) and for p–Pb collisions at $\sqrt{s}$ = 5.02 TeV (right). In Monte Carlo simulations the σ_{π^0} was extracted from validated π^0.

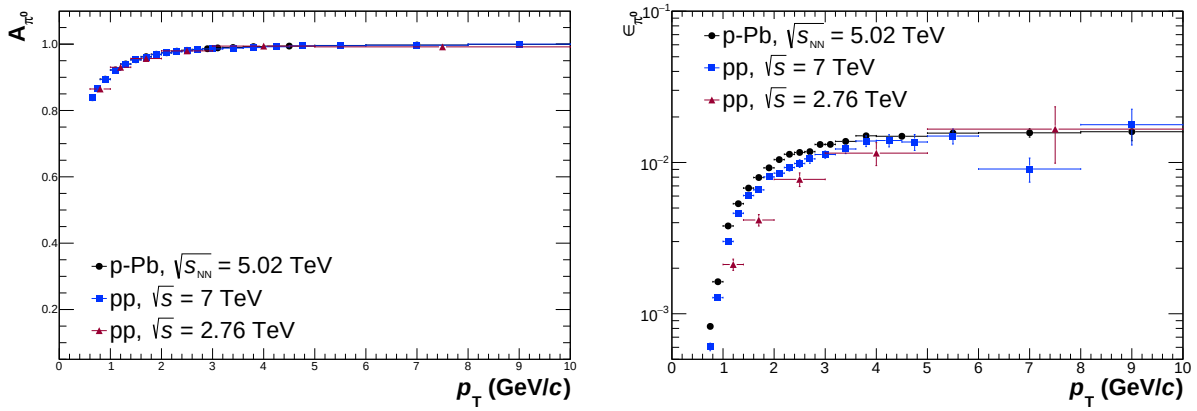

Figure 5.4: π^0 acceptance (left) and efficiency (right) as function of transverse momentum for pp collisions at $\sqrt{s} = 7$ TeV and $\sqrt{s} = 2.76$ TeV and for p-Pb collisions at $\sqrt{s_{\rm NN}} = 5.02$ TeV.

5.4.2 Subtraction of the contamination from $\pi^0 \to \gamma\gamma$ decay channel

Neutral pions decaying into two $\gamma\gamma$ that convert in the detector material can be reconstructed using the method described here if the conversion of one of the photons happens very close to the main vertex. These extra contribution is the main source of contamination. Although the $\Psi_{\rm pair}$ triangular cut (see section 4.3.1 and Tab. 4.6) and the requirement of a hit in any layer of the SPD reduces this contamination substantially, there is still a remaining contamination of about 3 % (see left panel of Fig. 5.5) that should be subtracted. The remaining contamination $C(p_{\rm T})$ is defined using Eq. (5.6) and it is computed using Monte Carlo simulations assuming that it is relatively the same as for real data. A correction factor is applied to the raw yields reconstructed in the two decay channels taking into account the difference between the Br(Dalitz) injected in

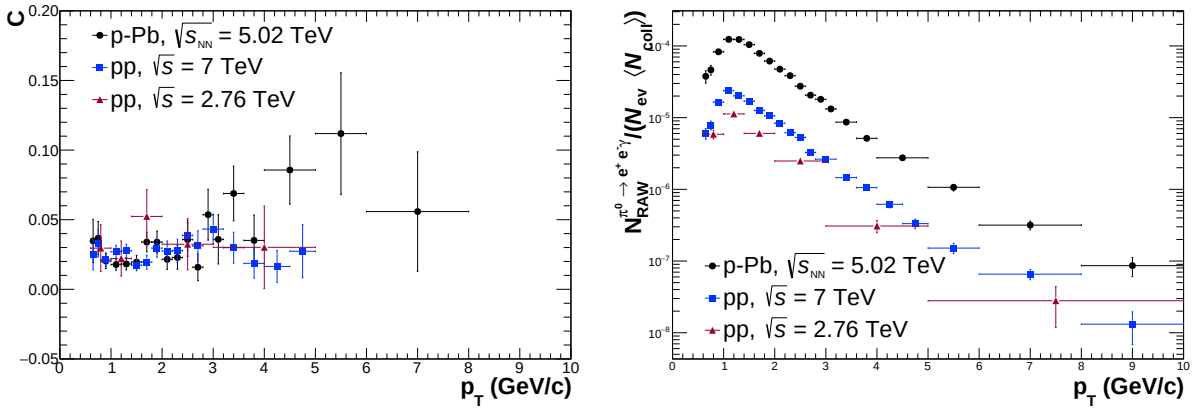

Figure 5.5: (Left): π^0 contamination fraction. (Right): π^0 raw yield in the dalitz channel

Monte Carlo ($\mathrm{Br}_{ee\gamma\mathrm{MC}}$) compared to the Br(Dalitz) from the PDG ($\mathrm{Br}_{\gamma\gamma\mathrm{PDG14}}$, $\mathrm{Br}_{ee\gamma\mathrm{PDG14}}$) [3].

$$C(p_T) = \frac{\frac{\mathrm{Br}_{\gamma\gamma\mathrm{PDG14}}}{\mathrm{Br}_{\gamma\gamma\mathrm{MC}}} \times N_{\mathrm{RAW}}^{\pi^0\to\gamma\gamma}(p_{\mathrm{T}})}{\frac{\mathrm{Br}_{\gamma\gamma\mathrm{PDG14}}}{\mathrm{Br}_{\gamma\gamma\mathrm{MC}}} \times N_{\mathrm{RAW}}^{\pi^0\to\gamma\gamma}(p_{\mathrm{T}}) + \frac{\mathrm{Br}_{ee\gamma\mathrm{PDG14}}}{\mathrm{Br}_{ee\gamma\mathrm{MC}}} \times N_{\mathrm{RAW}}^{\pi^0\to e^+e^-\gamma}(p_{\mathrm{T}})} \tag{5.6}$$

The resulting contamination fraction is subtracted from the real data ($N_{\mathrm{RAW}}^{\pi^0}$) using Eq. (5.7) to obtain $N_{\mathrm{RAW}}^{\pi^0\to e^+e^-\gamma}$.

$$N_{\mathrm{RAW}}^{\pi^0\to e^+e^-\gamma}(p_{\mathrm{T}}) = N_{\mathrm{RAW}}^{\pi^0}(p_{\mathrm{T}}) * (1 - C(p_{\mathrm{T}})) \tag{5.7}$$

The contamination fraction $C(p_{\mathrm{T}})$ and the raw yield $N_{RAW}^{\pi^0\to e^+e^-\gamma}$ as a function of transverse momentum for pp collisions at $\sqrt{s}$ = 7 TeV and $\sqrt{s}$ = 2.76 and for p–Pb collisions at $\sqrt{s_{\mathrm{NN}}}$ = 5.02 TeV are shown in Fig. 5.5.

5.4.3 Correction for finite bin width

The frequency of π^0 meson production becomes lower at higher p_{T}. One consequence of this is the choice of wider p_{T} bins in a region where the π^0 yield is smaller in order to have access to a larger p_{T} range measurement with reasonable statistical errors. The p_{T} value for a given yield is taken at the center of bin (Δx). However, it was shown in [147] that Δx bin does not correspond with the true p_{T} for the given yield and the deviation between the true p_{T} and Δx becomes larger at wider p_{T} bins.

According to [147] the appropriate p_{T} value can be estimated by shifting the data point to the true p_{T} bin, which can be estimated using a model prediction. Another approach is to estimate the yield for the given Δx bin. In this thesis, the p_{T} bin values of the measured pp and p–Pb spectra were shifted following the same procedure as the one used to shift the p_{T} bin values of the published spectra in pp collisions at $\sqrt{s}$ = 2.76 TeV [44] and at $\sqrt{s}$ = 7 TeV [146]. This correction was applied to the measured pp spectra in order to compare them to theoretical models (see section 6.2) and applied to the measured p–Pb spectrum in order to compute the

$R^{\pi^0}_{\mathrm{pPb}}$ (see section 6.3). The shifting procedure used in [44, 146] estimates the true p_{T} values by using the Tsallis function defined as [148]:

$$E\frac{\mathrm{d}^3N}{\mathrm{d}p^3} = \frac{1}{2\pi}A\frac{c\cdot(n-1)(n-2)}{nC[nC+m(n-2)]}\left[1+\frac{m_{\mathrm{T}}-m}{nC}\right]^{-n} \tag{5.8}$$

where A, C and n are the fit parameters.

5.5 Systematic errors

The systematic errors were estimated by studying the deviation of the corrected π^0 meson yield spectrum when varying every cut used during the π^0 meson reconstruction. This includes the cuts used in the virtual photon and the photon reconstruction as well as the ones used in the π^0 meson signal extraction.

To illustrate the calculation of the systematic errors, consider that the π^0 meson yield spectrum obtained using the default cuts summarized in Tabs. 4.5 to 4.7 and 5.1 is called standard and the spectrum obtained by varying only one cut at a time is called modified. Also consider that both the standard and the modified spectra are fully corrected by acceptance, efficiency, number of analyzed events and contamination using Eq. (6.1). On the basis of the above, the contribution of each cut to the total systematic errors is estimated as follows:

1. First, only one cut is varied at a time and the deviation of the modified spectrum from the standard one is computed as follows:

$$\Delta(p_{\mathrm{T}}) = \left.\frac{\mathrm{d}^2N}{\mathrm{d}y\mathrm{d}p_{\mathrm{T}}}\right|_{\text{modified}}(p_{\mathrm{T}}) - \left.\frac{\mathrm{d}^2N}{\mathrm{d}y\mathrm{d}p_{\mathrm{T}}}\right|_{\text{standard}}(p_{\mathrm{T}}) \tag{5.9}$$

   Except for electron selection and track reconstruction, the same variation ranges were used for the analyzed systems and they are summarized in Tab. 5.3. The variations ranges has been chosen in such away that the largest possible deviations can be accessed.

2. Once the deviations of each cut variation are obtained, the largest ones in positive and in negative directions are obtained for each bin of p_{T}. Subsequently, the systematic error is calculated bin by bin of p_{T} as the average between the positive and negative directions.

3. In order to reject contributions of unphysical fluctuations in the systematic errors, a cross-check using the Barlow check method [149] was performed. The Barlow check considers a deviation as a systematic error if $\Delta(p_{\mathrm{T}})/\sigma_{\Delta}(p_{\mathrm{T}}) > 1.0$, where $\sigma_{\Delta}(p_{\mathrm{T}})$ is the statistical error of Eq. (5.9) and it is defined as follows:

$$\sigma_{\Delta}(p_{\mathrm{T}}) = \sqrt{\left|\sigma^2_{\left(\frac{\mathrm{d}^2N}{\mathrm{d}y\mathrm{d}p_{\mathrm{T}}}\right)_{\text{modified}}}(p_{\mathrm{T}}) - \sigma^2_{\left(\frac{\mathrm{d}^2N}{\mathrm{d}y\mathrm{d}p_{\mathrm{T}}}\right)_{\text{standard}}}(p_{\mathrm{T}})\right|} \tag{5.10}$$

4. As the Barlow check only takes into account statistically significant deviations, it may occur that some p_{T} bins have a systematic error equal to zero introducing unphysical fluctuations. Therefore, the systematic error of those p_{T} bins is computed as follows:

- If the p_{T} bin is placed closer to the bottom and top edges of the spectrum, the systematic error is taken as the sum of the weighted errors of its left and right neighbors. This is done because of the low statistics in the top (bottom) edges of the spectrum may lead to an overestimation of the systematic error. The weights used at the bottom edge of the spectrum are W_{left}=0.2 and W_{right} = 0.8 and the ones used at the top edge are W_{left}=0.2 and W_{right} = 0.8
- If the p_{T} bin is located at the intermediate region of the spectrum, the systematic error is taken as the average between its nearest left and right neighbors.

Once one has obtained the systematic errors for each cut, the total systematic error is calculated by adding all the sources in squared roots. For a better understanding, the different sources of systematic errors have been gruped as follows:

Branching ratio

The branching ratio of the π^0 meson into the Dalitz decay channel ($\pi^0 \rightarrow e^+e^-\gamma$) is known with a limited accuracy (see Tab. 2.1). Therefore, the 2.98 % relative error is taken as systematic error.

Material Budget

The contribution of the material budget was taken from [146] and the details of how it was obtained can be found in [140]. According to [140], the material budget error was estimated by varying the photon conversion radius, by using the two different V^0 finder algorithms (see section 3.3.2) and by using different Monte Carlo simulations. The systematic error of the material budget was found in [140] to be constant over the full range of p_{T} with a value of 4.5 %.

Track reconstruction

The track reconstruction groups the contribution of primary and secondary track selections. This includes the number of TPC clusters (N_{TPCcls}) (in the case of p–Pb collisions number of TPC crossed row pads), the single p_{T} cut for primary and secondary electrons, the ratio between the found and findable clusters ($N^{\mathrm{found}}_{\mathrm{TPCcls}}/N^{\mathrm{findable}}_{\mathrm{TPCcls}}$) and the DCA_{xy} cut. The systematic errors obtained for pp collisions at $\sqrt{s}$ =7 TeV and for p–Pb collisions at $\sqrt{s_{\mathrm{NN}}}$ = 5.02 TeV showed fluctuations that seemed to have an unphysical origin. Therefore, the systematic errors of these two energies were calculated by fitting the measured ones with polynomial functions of degree 3 and 4. The systematic error due to track reconstruction was found to be of the same order ($\sim$ 1.5%) for pp collisions at $\sqrt{s}$ = 7 TeV and for p–Pb collisions at $\sqrt{s_{\mathrm{NN}}}$ = 5.03 at low transverse momentum (1.3 GeV/c) while for pp collisions at $\sqrt{s}$ = 2.76 TeV, the obtained systematic was found to be 9 % for p_{T}=1.2 GeV/c and it represents the largest contribution to the total systematic errors in this analyzed system. The above is due to the low statistics of the data sample used in the analysis of pp collisions at $\sqrt{s}$ = 2.76 that makes much harder to disentangle statistical from systematic errors in this system

Reconstruction Efficiency

This group contains the variation of the π^0 meson rapidity (y_{π^0}) and the variation of the pseudorapity of primary and secondary electrons. For pp collisions at $\sqrt{s}$ = 2.76 TeV, the reconstruction efficiency is the largest contribution at intermediate momentum (2.5 GeV/c) with 7.4 %. For pp collisions at $\sqrt{s}$ = 7 TeV the contribution at low momentum (1.3 GeV/c) and at intermediate momentum (5.5 GeV/c) is of the order of 2.0 % and 1.3 %, respectively. In the same regions the systematic errors of p–Pb collisions at $\sqrt{s_{\mathrm{NN}}}$ = 5.02 TeV are 1.6 % and 3.4 %.

Electron selection: primary and secondary tracks

The electron selection group contains the systematic error of the particle identification. This includes the electron inclusion and pion rejection cuts applied in the primary and secondary electron selection. The systematic errors obtained for $\sqrt{s}$ = 7 TeV were calculated in a similar way as in the track reconstruction as they exhibit unphysical fluctuations. For $\sqrt{s}$ = 2.76 TeV and $\sqrt{s_{\mathrm{NN}}}$ = 5.02 TeV this correction was not applied since the fluctuations observed in these two systems are smoother than the ones at $\sqrt{s}$ = 7 TeV. For $\sqrt{s_{\mathrm{NN}}}$ = 5.02 TeV the electron selection is the largest contribution to the total systematic errors at intermediate momentum (5.5 GeV/c) with 7.6 %. The contribution of electron selection for $\sqrt{s}$ = 7 TeV at intermediate momentum (5.5 GeV/c) is of the order of 5.6 % while for $\sqrt{s}$ = 2.76 TeV at p_{T}=2.5 GeV/c is of the order of 6.7 %.

Photon selection

It contains the contribution from the cuts applied in the photon selection as the χ^2 cut and the q_{T} cut and the contribution of the $M_{\mathrm{e^+e^-}}$ cut applied in the γ^* selection. As the contribution of the conversion radius, and the V^0 finder algorithms are already included in the material budget error, they were not taken into account in the photon selection error. The systematic errors for $\sqrt{s}$ = 7 TeV were smoothed with polynomial functions of grade 3 and 4. The systematic errors obtained for $\sqrt{s}$ = 5.02 TeV at low momentum (1.3 GeV/c) and at intermediate momentum (5.5 GeV/c) are of the order of 3.9 % and 4.8 %, respectively. In the same p_{T} bins the systematic errors for $\sqrt{s}$ = 7 TeV are $\sim$ 1.1 % and $\sim$ 6.2 %. On the other hand, the systematic errors obtained for 2.76 TeV are larger than the ones obtained for 7 TeV and 5.02 TeV with 7.73 % (p_{T}=1.2 GeV/c) and 7.4 % (p_{T}=7.4 GeV/c).

Yield extraction

This systematic error was computed by varying the integration window used for the π^0 meson yield extraction (see Tab. 5.2). In the p_{T} region were the signal extraction seems to be more stable (1.1 < p_{T}< 5.5 GeV/c), the largest contribution obtained for 7 TeV and for 5.02 TeV is of the same order 4.5 %. The same value is obtained for 2.76 at the p_{T} region: 1.2 - 2.5 GeV/c.

Rejection of $\pi^0 \to \gamma\gamma$

It contains the contribution of the cuts applied in the rejection of γs from the $\pi^0 \rightarrow \gamma\gamma$ decay channel during the virtual photon reconstruction. The systematic error was computed by varying the SPD cut and the Ψ_{pair}triangular cut. The systematic error obtained in p–Pb collisions (6.1 %) is larger than the ones obtained in pp collisions. It seems that the Monte Carlo simulations do not reproduce precisely the response of the SPD detector in p–Pb collisions.

Combinatorial background calculation

This group contains the contribution of the combinatorial background calculation when varying the number of gammas and when using track multiplicity and γ multiplicity for the event pool filling (see section 5.2). The combinatorial background estimation represents the smaller contribution to the total systematic errors.

Figure 5.6 shows the total systematic error obtained for each bin of p_{T} and the individual contribution of each group described above. The contribution of each group to the total systematic error at low and at intermediate p_{T} are summarized in Tab. 5.4.

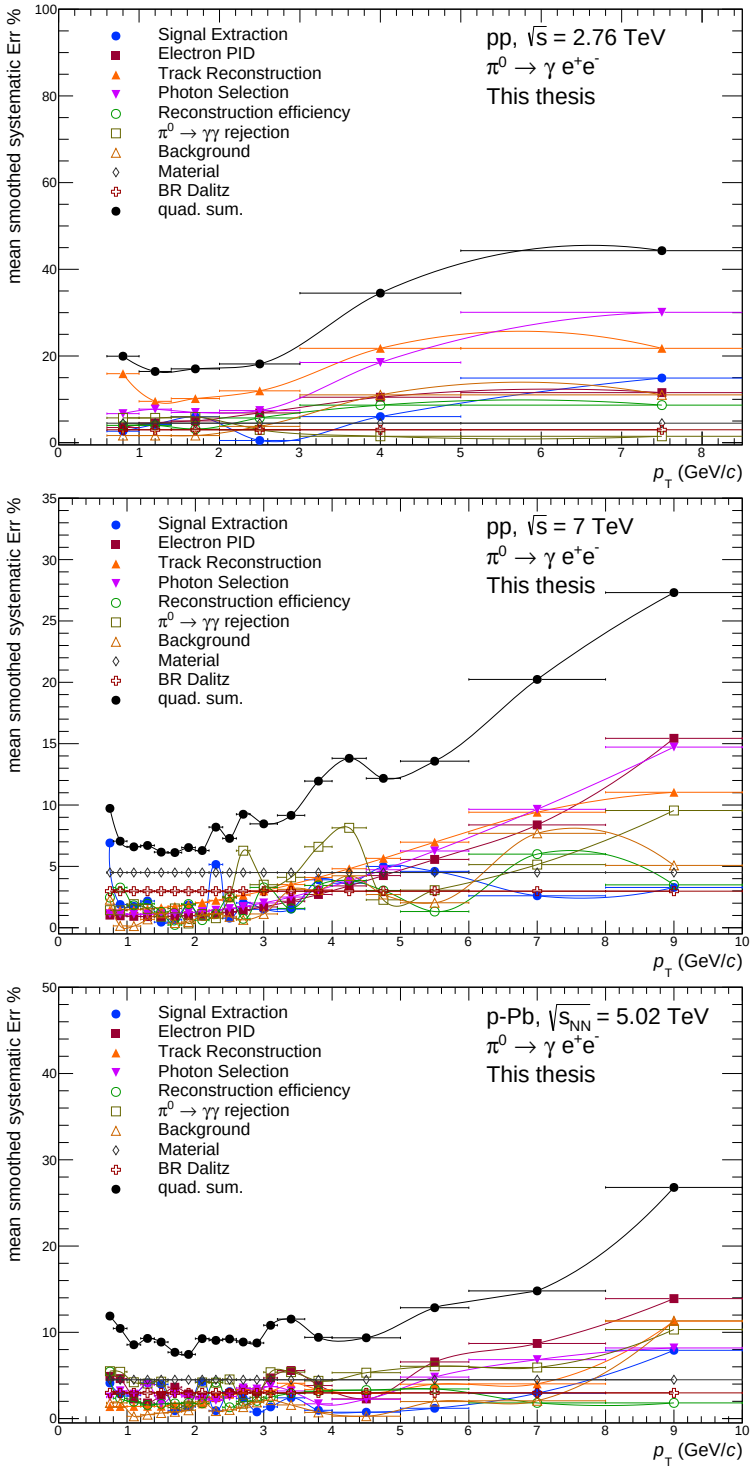

Figure 5.6: Visualization of the systematic errors obtained in pp collisions at $\sqrt{s}$ = 2.76 TeV (top) and at $\sqrt{s}$ = 7 TeV (middle) and in p–Pb collisions at $\sqrt{s_{\mathrm{NN}}}$ = 5.02 TeV (bottom). The different sources of background have been grouped into 8 categories: Track Selection, Electron Selection, Photon Selection Yield Extraction, Background, Reconstruction Efficiency, Contamination, Material Budget and Dalitz Branching Ratio.

Quantitive	nominal	variation
Primaries		
DCA$_{xy}$	p_{T} dependent	$<$ 1 cm
Single p_{T}	$>$ 0.125 GeV	$>$ 0.100 GeV/c, $<$ 0.150 GeV/c
$N_{\mathrm{TPCcls}}^{\mathrm{found}}/N_{\mathrm{TPCcls}}^{\mathrm{findable}}$	$>$ 0.35	$>$ 0.6
N_{TPCcls}	$>$ 70	$>$ 0
Secondaries		
Single p_{T}	$>$ 0.050 GeV	$>$ 0.075 GeV/c, $>$ 0.100 GeV/c
$N_{\mathrm{TPCcls}}^{\mathrm{found}}/N_{\mathrm{TPCcls}}^{\mathrm{findable}}$	$>$ 0.6	$>$ 0.35
dE/dx e-line primaries		
$\sigma_{dE}/dx, e$	-4 $<\sigma<$ 5	-5 $<\sigma<$ 5 ,-3 $<\sigma<$ 5
dE/dx π-line primaries		
p_{min}, π rej	0.5 GeV/c	0.3 GeV/c
p_{max}, π rej	3.5 GeV/c	5.0 GeV/c
π rej. $p_{min} < p < p_{max}$		
$\sigma_{dE}/dx, \pi$	$\sigma <$ 2.0	
π rej. $p > p_{max}$		
$\sigma_{dE}/dx, \pi$	$\sigma <$ 2.0	$\sigma <$ -1.0, $\sigma <$0.0
dE/dx e-line secondaries		
$\sigma_{dE}/dx, e$	-4 $<\sigma<$ 5	-5 $<\sigma<$ 5, -3 $<\sigma<$ 5
dE/dx π-line secondaries		
p_{min}, π rej	0.5 GeV/c	0.3 GeV/c
p_{max}, π rej	3.5 GeV/c	5.0 GeV/c
π rej. $p_{min} < p < p_{max}$		
$\sigma_{dE}/dx, \pi$	$<$ 2.0	
π rej. $p > p_{max}$		
$\sigma_{dE}/dx, \pi$	$<$ 0.5	$<$ 1.0
$\chi^2(\gamma)$	$<$20	$<$15, $<$30, $<$50
$q_{\mathrm{T}}(\gamma)$	$<$0.15	$<$ 0.03, $<$ 0.05, $<$0.07
$M_{\gamma^*\gamma}$	if p_{T} $<$1.0 GeV	
	$<$ 0.015 GeV	$<$ 0.050 GeV
	if $p_{\mathrm{T}} >$ 1.0 GeV	
	$<$ 0.035 GeV	
SPD requirement	Any layer	First layer
$\Psi_{\mathbf{pair}}$	Ψ_{pair} cut = 0.45	Ψ_{pair} cut = 0.60
	$0.0 < \Delta\phi < 0.12$	$0.0 < \Delta\phi < 0.12$
y(π^0)	$<$ 0.8	$<$ 0.75
$\eta(e^+e^-\gamma)$	$<$ 0.9	$<$ 0.8
α **(π^0)**	$<$ 1.0	$<$ 0.7
Background		
Method	Mixed event	Mixed event
	Track Mult	Track Mult
N_γ	80	100

Table 5.3: Cuts variations to computed the systematic errors in pp and p–Pb analysis. In the p–Pb analysis the number of crossed rows was used instead of the number of clusters in the TPC.

Source	Type	pp at $\sqrt{s}$ = 2.76 TeV syst. err. (%)		pp at $\sqrt{s}$ = 7 TeV syst. err. (%)		p–Pb at $\sqrt{s_{\rm NN}}$ = 5.02 TeV syst. err. (%)	
		$p_{\rm T}$ =1.2 GeV/c	$p_{\rm T}$ =2.5 GeV/c	$p_{\rm T}$ =1.3 GeV/c	$p_{\rm T}$ =5.5 GeV/c	p_T =1.3 GeV/c	p_T =5.5 GeV/c
Track selection	A	9.5	6.9	1.5	6.3	1.4	4.0
Electron selection	A	4.6	6.7	0.9	5.6	1.8	7.6
Photon selection	A	7.7	7.4	1.1	6.2	3.9	4.8
Yield Extraction	A	4.2	0.5	2.2	4.6	4.2	1.2
Background subtraction	A	1.6	3.0	0.7	2.0	0.5	2.0
Rec. Efficiency	B	4.0	7.4	2.0	1.3	1.6	3.4
Contamination	B	5.7	3.0	1.5	3.0	4.1	6.1
Material budget	C	4.5	4.5	4.5	4.5	4.5	4.5
Dalitz BR	C	2.98	2.98	2.98	2.98	2.98	2.98

Table 5.4: Summary of the different contributions to the systematic errors for selected $p_{\rm T}$ bins.

Chapter 6

Results and discussion

The differential invariant π^0 meson yields in pp collisions at $\sqrt{s}$ = 2.76 TeV and $\sqrt{s}$ = 7 TeV and in p–Pb collisions at $\sqrt{s_{\rm NN}}$ = 5.02 TeV and the differential π^0 cross sections in pp collisions at the mentioned energies will be presented in this chapter. The calculation of the pp reference at $\sqrt{s}$ = 5.02 TeV and the nuclear modification factor ($R^{\pi^0}_{\rm pPb}$) will also be presented. Furthermore, the results are compared to other measurements available in ALICE and to theoretical model calculations.

6.1 Invariant π^0 meson yields in pp and p–Pb collisions

The differential invariant π^0 meson yields in pp collisions at $\sqrt{s}$ = 2.76 TeV and $\sqrt{s}$ = 7 TeV and in p–Pb collisions at $\sqrt{s_{\rm NN}}$ = 5.02 TeV were obtained using:

$$E\frac{{\rm d}^3N}{{\rm d}p^3} = \frac{{\rm d}^3N}{p_{\rm T}{\rm d}y{\rm d}p_{\rm T}{\rm d}\phi} = \frac{1}{2\pi}\frac{1}{p_{\rm T}}\frac{{\rm d}^2N^{\pi^0}}{{\rm d}y{\rm d}p_{\rm T}} = \frac{1}{2\pi}\frac{1}{N_{\rm evt,norm}}\frac{1}{p_{\rm T}}\frac{1}{\epsilon}\frac{1}{A}\frac{1}{\rm Br(Dalitz)}\frac{N^{\pi^0\to e^+e^-\gamma}_{\rm RAW}}{\Delta y\Delta p_{\rm T}} \tag{6.1}$$

where $N_{\rm evt,norm}$ is the number of events calculated according to Eqs. (4.1) and (4.2), ϵ is the π^0 reconstruction efficiency, A is the acceptance, Br(Dalitz) is the branching ratio of the π^0 meson into the Dalitz ($e^+e^-\gamma$) decay channel, $N^{\pi^0\to e^+e^-\gamma}_{\rm RAW}$ is the transverse momentum in a given Δy and $\Delta p_{\rm T}$ bin after correction for contamination and $p_{\rm T}$ is the transverse momentum within the bin in which the invariant yield has been assigned to. The measurements have been done in the rapidity range of $|y_{\rm cms}| < 0.8$ for pp collisions and $-0.335 < y_{\rm cms} < 1.265$ ($|y_{\rm lab}| < 0.8$) for p–Pb collisions and cover the transverse momentum range $0.65 < p_{\rm T} < 10$ GeV/c.

The obtained differential invariant π^0 meson yields fitted with the Tsallis function (see Eq. (5.8)) are shown in Fig. 6.1a and the ratios of the data to the fit for p–Pb collisions at $\sqrt{s_{\rm NN}}$ = 5.02 TeV, for pp collisions at $\sqrt{s}$ = 7 TeV and at at $\sqrt{s}$ = 2.76 TeV are shown in Fig. 6.1b. The resulting fit parameters (see Tab. 6.1) obtained in this thesis for pp collisions at $\sqrt{s}$ = 2.76 TeV are in agreement within the errors with the ones obtained in [44]. This is not the case for pp collisions at $\sqrt{s}$ = 7 TeV, where the parameters of this thesis are slightly different from the ones shown in [146] and this will be discussed in chapter 7.

System	$\sqrt{s_{\mathrm{NN}}}$ (TeV)	Tsallis function A	T (MeV/c)	n
pp	2.76	1.78 ± 0.84	161 ± 50	9.75 ± 2.75
pp	7	1.93 ± 0.28	164 ± 16	7.36 ± 0.52
p–Pb	5.02	7.31 ± 0.96	193 ± 17	7.96 ± 0.62

Table 6.1: Fit parameters obtained from fits to the invariant differential yields at different energies and collisions systems using the Tsallis function (see Eq. (5.8)). The errors account for systematic and statistical uncertainties.

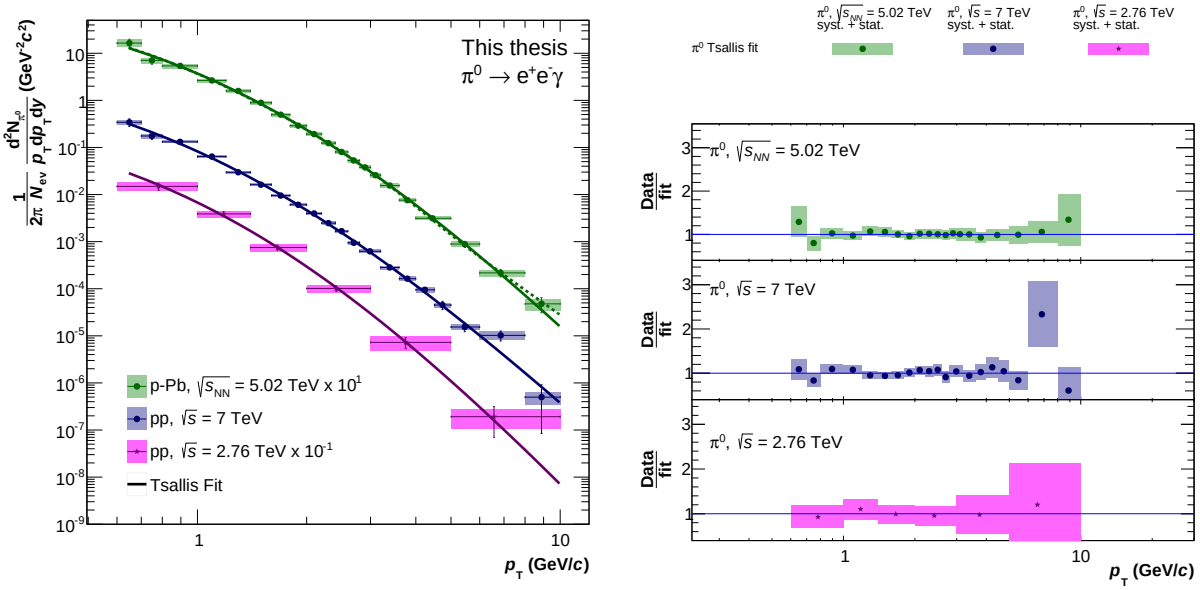

(a) **(b)**

Figure 6.1: (Left) Differential invariant π^0 yields for pp collisions at $\sqrt{s}$ = 2.76 TeV (pink) and at $\sqrt{s}$ =7 TeV (purple) and for p–Pb collisions at $\sqrt{s_{\mathrm{NN}}}$ = 5.02 TeV (green) fitted with the Tsallis function (black line). (Right) Ratio of data to th fit for p–Pb collisions at $\sqrt{s}$ = 5.02 TeV (top) and for pp collisions at $\sqrt{s}$ = 7 TeV (middle) and at $\sqrt{s}$ = 2.76 TeV (bottom).

6.1.1 Comparison to PCM method

The differential invariant π^0 meson yields obtained in this thesis (Dalitz) were compared to the ones obtained by measuring the π^0 meson production through its 2γ decay channel (PCM). The aim of this comparison is two fold: (1) to provide a consistency check of the material budget and its precision estimated using the PCM method and (2) to provide a partially independent measurement that can contribute to the total combined spectrum. The consistency check is performed by computing the ratio between the two measurement as it was shown in Eq. (2.3). Due to the fact that in the case of the Dalitz analysis one photon is reconstructed, the material budget cancels out with one photon of the PCM analysis. Therefore, if the conversion probability is well described in Monte Carlo simulations, the two measurements should be compatible and the ratio equal to one.

System	$\sqrt{s_{\rm NN}}$ (TeV)	p_0	χ^2	χ^2/ndf
pp	7	0.95 ± 0.03	9.23	0.54
pp	2.76	0.99 ± 0.08	1.20	0.4
p–Pb	5.02	0.96 ± 0.03	3.41	0.18

Table 6.2: Parameters from pol0 fits to the ratio of the two π^0 meson measurements, the Dalitz and the 2γ, for the different energies under study.

The PCM results used in this comparison correspond to the published ones in pp collisions at $\sqrt{s}$ = 7 TeV [146] and at $\sqrt{s}$ = 2.76 TeV [44]. The published pp spectrum at $\sqrt{s}$ = 7 TeV was corrected for an extra contribution from pile up events that was found after it was published. The correction factor is shown in Fig. D.2. The material budget error was subtracted from the PCM measurement as $e = \sqrt{e^2 - (2 * m)^2 + m^2}$ and for the Dalitz measurement as $e = \sqrt{e^2 - (m)^2}$, where e corresponds to the total systematic error and m corresponds to the error of the material budget ($\pm$ 4.5 % [146]). Additionally, the $p_{\rm T}$ intervals of the two measurements were adjusted to be compatibles. The value of the $p_{\rm T}$ bins were taken as the center of each bin. Figure 6.2 shows the ratio for the three systems under study. The errors bars account for the systematical and statistical errors added in quadrature. A good agreement for the three systems under study is observed. The results of fits to the ratio with a fit to a constant are summarized in Tab. 6.2. Due to the lack of statistics in pp collisions at $\sqrt{s}$ = 2.76 TeV it was only possible to compare four points. For pp collisions at $\sqrt{s}$ = 7 TeV, the Dalitz measurement is systematically below PCM by 5 % but compatible within the errors. A similar but more stable trend is observed for p–Pb collisions at $\sqrt{s_{\rm NN}}$ = 5.02 TeV. The above can be due to the precision of the description of the SPD response detector in Monte Carlo simulations. Nevertheless, the systematical error of SPD response was calculated and added to the Dalitz measurements.

The above results tell us that the conversion probability is well described in the Monte Carlo simulations used for corrections. The good agreement tells us that our measurements are reliable and can also be used for the total combined result. The π^0 reconstruction using the Dalitz channel was also developed within this thesis for EMCal and PHOS in order to check the consistency of these measurements in p–Pb collisions [150].

6.1.2 Comparison to charged pions and to other π^0 meson measurements

The invariant yields obtained in this thesis have been compared to the invariant yields of charged pions. It is expected that the ratio of π^0 $/(\pi^+ + \pi^-)/2$ is equal to one. Therefore, this comparison is a good cross check for both measurements.

In addition, as it was mentioned in section 4.4.1, apart from the Dalitz method (this thesis) and the PCM method, the ALICE detector can also measure the π^0 meson production trough its 2γ decay channel by the following methods:

- PHOS: In this method the two γ's are reconstructed in the Photon Spectrometer (PHOS) calorimeter. The analysis is described [151].
- EMCal: In this method the two γ's are reconstructed using the Electromagnetic Calorimeter (EMCal). This analysis is described in [152].

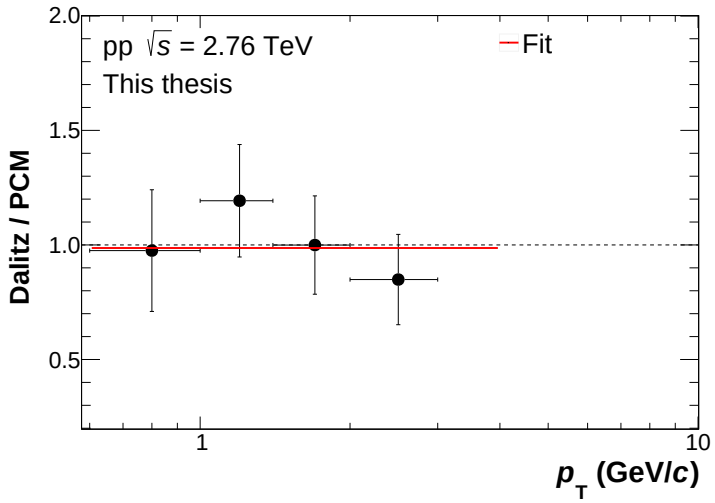

(a)

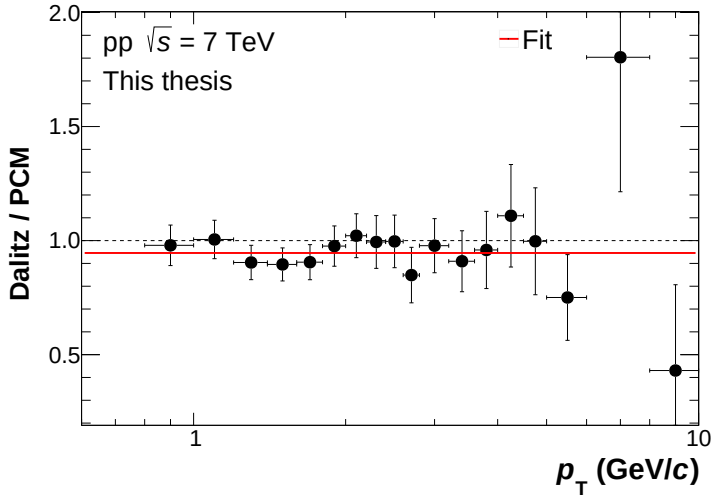

(b)

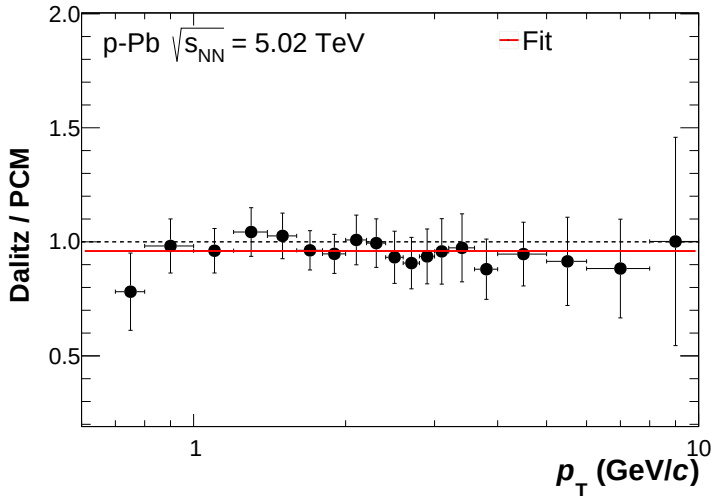

(c)

Figure 6.2: The differential invariant π^0 meson yields obtained in this thesis (Dalitz) compared to the ones obtained with the PCM method at different energies: (top) pp at $\sqrt{s}$ = 2.76 TeV, (middle) pp at $\sqrt{s}$ = 7 TeV, and (bottom) p–Pb at $\sqrt{s}$ = 5.02 TeV. The PCM results for pp collisions correspond to the published papers at $\sqrt{s}$ = 2.76 TeV [44] and at $\sqrt{s}$ = 7 TeV [146] with an extra pile up correction. The errors bars account for systematic and statistic errors added in quadrature. The error of the material budget was canceled out according to Eq. (2.3).

In order to build the ratio between the invariant yields of the π^0 and the charged pions, the p_{T} intervals has to be the same. Therefore, the p_{T} intervals were adjusted to be the same in both measurements. Again, the p_{T} bin value was taken at the center of the p_{T} interval.

Figure 6.3 shows the ratio between the Dalitz measurement and the charged pion invariant yield at the three systems under study. For comparison, the plots also show the ratio between the charged pion and the π^0 meson measurements done by the PCM, PHOS and EMCal methods. The error bars account for systematic and statistical errors added in quadrature. The result of this thesis is in agreement with the charged pion measurement within errors. The ratio for pp collisions at $\sqrt{s}$ = 7 TeV and the ratio for p–Pb collisions show an offset of about $\sim 5\%$ and $\sim 10\%$ respectively. But if one takes into account the systematic errors, both measurement are compatibles.

Figure 6.3 also shows the good agreement between the Dalitz measurement and the PHOS and EMCal measurements at the three energies under study, specially at the $1 < p_{\mathrm{T}} < 5$ GeV/c interval where the statistics are larger.

6.2 Differential invariant π^0 meson cross sections compared to model calculations

The measured differential invariant π^0 meson cross sections in pp collisions at the two energies under study were compared to Next-Leading Order (NLO) perturbative QCD (pQCD) model calculations and to PYTHIA. The pQCD framework can give a quantitative description of hard-scattering process using Parton Distribution Functions (PDFs) and Parton-to-Hadron Fragmentation Functions (FFs) as inputs. The PDFs are defined as $f(x)$ where x is the fraction of the longitudinal momentum carried by a parton inside the proton and the FFs are defined as $D_i^H(z, Q^2)$ where z is the momentum fraction carried by the final-state hadron H taken from parton momentum. In other words, the FFs are the probability that a parton of flavour i fragments into a hadron H taken a fraction of the parton momentum z at the scale Q^2. Both PDFs and FFs are non-perturbative quantities, and they are obtained from global QCD analysis combining different experimental results [153]. The results of this thesis can serve as a test for pQCD models calculations and can also bring new constraints for such models, specially at the gluon-to-pion Fragmentation Functions as gluon fragmentation is the main source of π^0 mesons at high p_{T} at LHC energies [146, 154].

In order to compare to pQCD model calculations, the differential invariant cross sections in pp collisions were obtained as:

$$E\frac{\mathrm{d}^3\sigma}{\mathrm{d}p^3} = \frac{1}{2\pi}\frac{1}{p_{\mathrm{T}}}\frac{\sigma_{\mathrm{MB}}}{N_{\mathrm{evt,norm}}}\frac{1}{\epsilon}\frac{1}{A}\frac{1}{\mathrm{Br(Dalitz)}}\frac{N_{\mathrm{RAW}}^{\pi^0\to e^+e^-\gamma}}{\Delta y \Delta p_{\mathrm{T}}}. \tag{6.2}$$

where σ_{MB} is the cross section taken from Tab. 4.4 and the other variables are define as in Eq. (6.1). The efficiency of the $\mathrm{MB_{OR}}$ trigger is taken into account by the σ_{MB}.

The NLO pQCD predictions compared to the results of this thesis uses MSTW PDFs [155] and DSS14 FFs [153] as Parton-to-hadron Fragmentation Functions and Parton Distribution Functions, respectively. The DSS14 FFs set correspond to the new release of the DSS FFs set [156],

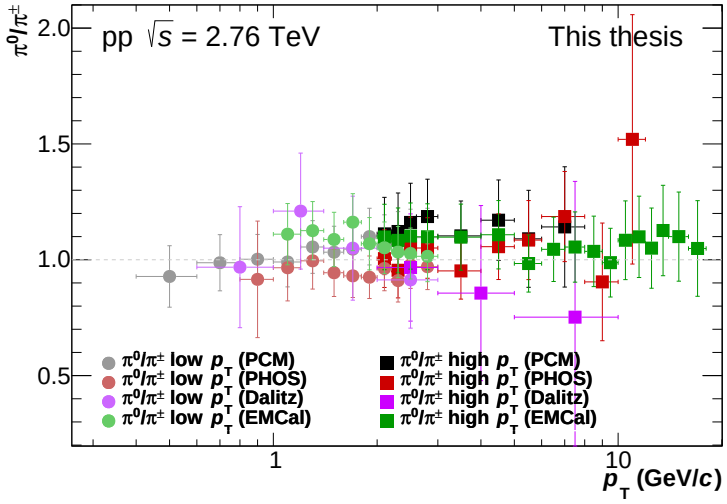

(a)

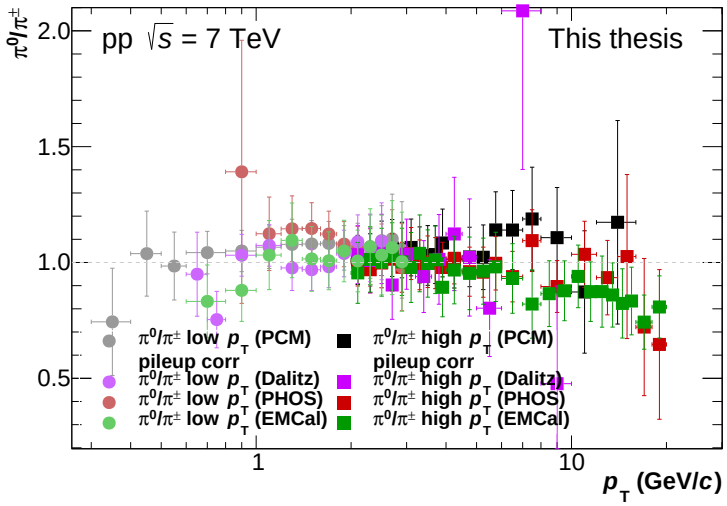

(b)

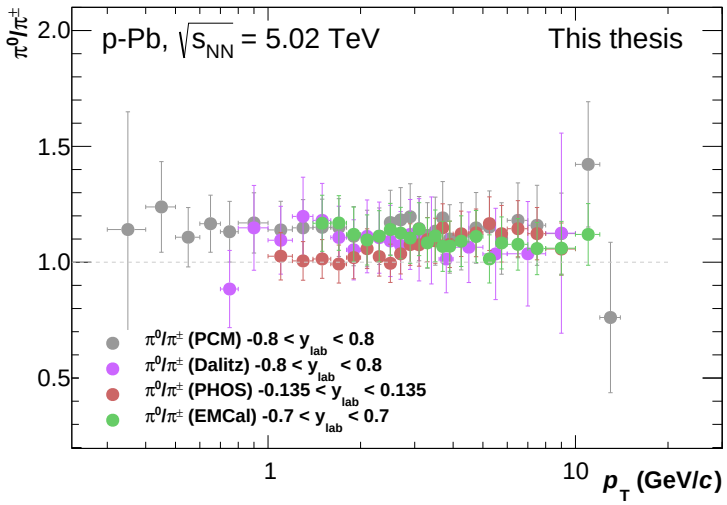

(c)

Figure 6.3: The differential invariant π^0 meson yield obtained in this thesis (Dalitz) compared to charged pions at different energies: (top) pp at $\sqrt{s}$ = 2.76 TeV. (middle) pp at $\sqrt{s}$ = 7 TeV. (bottom) p–Pb at $\sqrt{s}$ = 5.02 TeV. For comparison, the comparison between charged pions and the π^0 meson measurements done with the PCM, PHOS and EMCal methods are also plotted in the figure.

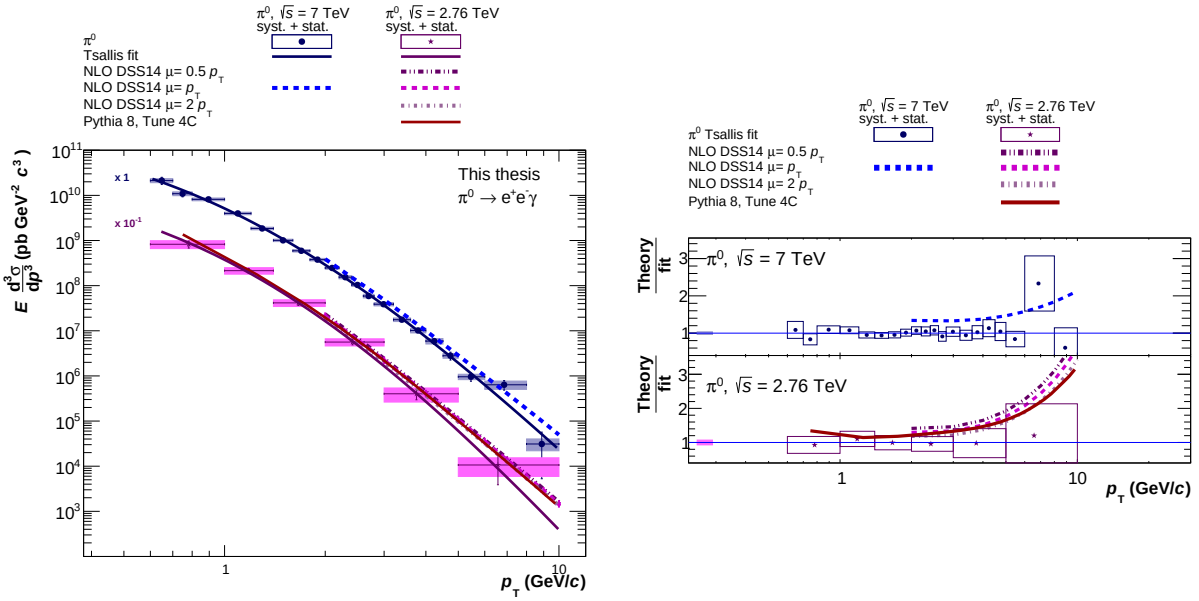

Figure 6.4: (Left) Differential invariant π^0 meson cross sections for pp collisions at $\sqrt{s}$ = 2.76 TeV and at $\sqrt{s}$ =7 TeV fitted with the Tsallis function and compared to pQCD NLO calculations which uses MSTW [155] PDFs and DSS14 [153] as FFs and to PYTHIA 8.176 Tune 4C [161, 162]. (Left) Ratio of model predictions and cross sections to the resulting fits for pp collisions at $\sqrt{s}$ = 7 TeV (top) and at $\sqrt{s}$ = 2.76 TeV (bottom).

which failed to describe the π^0 meson production at $\sqrt{s}$ = 7 TeV [146] and at $\sqrt{s}$ = 2.76 TeV [44]. The DSS14 FFs set apart from incorporate the ALICE results published in [146], they incorporate results of the π^0 meson and charged pions production in pp collisions at $\sqrt{s}$ = 200 GeV measured by STAR [157–159]. The systematic uncertainties of the FFs are computed based on the iterative Hessian approach (IH) [160].

Similarly to the invariant yields shown in Fig. 6.1, the differential invariant π^0 meson cross section spectra were fitted with the Tsallis function in order to compare them with model calculations. The fit was performed to avoid incompatible bins or fluctuations present in the spectra.

Figure 6.4 (left panel) shows the spectra in pp collisions at $\sqrt{s}$ = 7 TeV and at $\sqrt{s}$ = 2.76 TeV fitted with the Tsallis function together with PYTHIA 8.176 Tune 4C (for $\sqrt{s}$ = 2.76 TeV) and to NLO pQCD model prediction bands at different μ scales: $\mu = p_{\mathrm{T}}/2$, $\mu = p_{\mathrm{T}}$ and $\mu = 2p_{\mathrm{T}}$ for pp at $\sqrt{s}$ = 2.76 TeV and $\mu = p_{\mathrm{T}}$ for pp at $\sqrt{s}$ = 7 TeV. The uncertainties of the σ_{MB} for pp at $\sqrt{s}$ = 2.76 TeV ($\pm$ 3.9 %) and for pp at $\sqrt{s}$ = 7 TeV ($\pm$ 2.18 %) are not included in the spectra. The ratios to the fit are shown in the right panel of the figure. As one can see, the NLO pQCD model predictions reproduce the shape of the pp spectra in the the range of 2 < p_{T}< 5 GeV/c and they are in agreement within the errors with $\sqrt{s}$ = 2.76 TeV. A similar trend was observed in the comparison with the combined results using the PCM method and the PHOS method[163]. However, in [163] is also showed that for $p_{\mathrm{T}} > 10$ GeV/c the predictions start to over-predict the π^0 meson production. Unfortunately, due to the lack of statistics one cannot extend the comparison to values $p_{\mathrm{T}} > 10$ GeV. Additionally, PYTHIA seems to reproduce the shape of the spectrum of pp collisions at $\sqrt{s}$ = 2.76 TeV for 0.65 < p_{T}< 5 GeV/c.

6.2.1 Combined π^0 meson results in p–Pb

The combined π^0 meson spectrum in p–Pb collisions at $\sqrt{s_{\rm NN}}$ = 5.02 TeV is obtained as the weighed average of the π^0 meson measurements carried out by the methods Dalitz (this thesis), PCM [164], PHOS[151] and EMCal[152]. The weights are obtained using a correlation matrix that takes into account the systematic and the statistical errors of each measurement and it also takes into account the weak correlation between the Dalitz and PCM methods. Moreover, for each $p_{\rm T}$ bin only those measurements compatible with the $p_{\rm T}$ interval are taken into account. The resulting combined p–Pb spectrum covers the $p_{\rm T}$ range of 0.3 < $p_{\rm T}$< 20 GeV/c.
The combined π^0 meson spectrum is fitted with a two-component function proposed by A. A. Bylinkin and A. A. Rostovtsev (Bylinkin-Rostovtsev) defined as [165]:

$$\frac{1}{2\pi N_{ev}}\frac{{\rm d}^2N}{p_{\rm T}{\rm d}p_{\rm T}{\rm d}y} = A_e * {\rm e}^{-\frac{\sqrt{p_{\rm T}^2+m^2}-m}{T_e}} + \frac{A}{1+\frac{p_{\rm T}^2}{(T^2*n)^{-n}}} \tag{6.3}$$

where m is the π^0 meson mass, A_e and A are the normalization factors, T_e and T are the QCD analogy to the thermodynamic temperature, n is related to the slope of the spectrum. The obtained invariant π^0 meson yield fitted with the Bylinkin-Rostovtsev function can be seen in Fig. 6.5. The ratio of the combined π^0 meson spectrum to the Bylinkin-Rostovtsev fit is shown in Fig. 6.6 (top). As it can be observed the Bylinkin-Rostovtsev reproduces the shape of the combined π^0 meson spectrum in most of the $p_{\rm T}$ region (except the last 2 $p_{\rm T}$ bins).

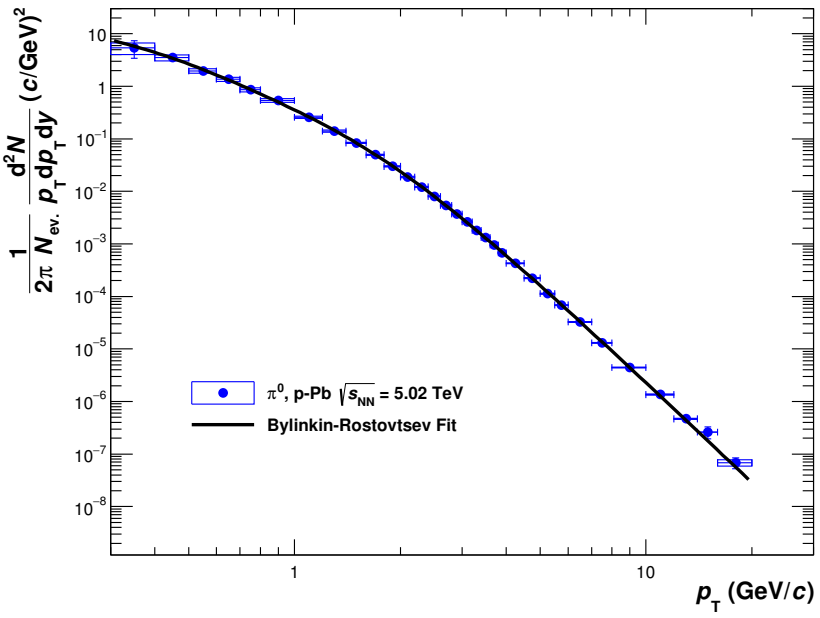

Figure 6.5: Combined π^0 meson spectrum fitted with the Bylinkin-Rostovtsev function.

For consistency check, the ratio of the individual measurements to the fit to the combined spectrum is shown in Fig. 6.6 (bottom). A good agreement is observed. The combined spectrum paper is in preparation and it will include the combined $R_{\rm pPb}^{\pi^0}$ that is calculated as the weighed average of the individual $R_{\rm pPb}^{\pi^0}$ (Dalitz, PCM, PHOS, EMCal).

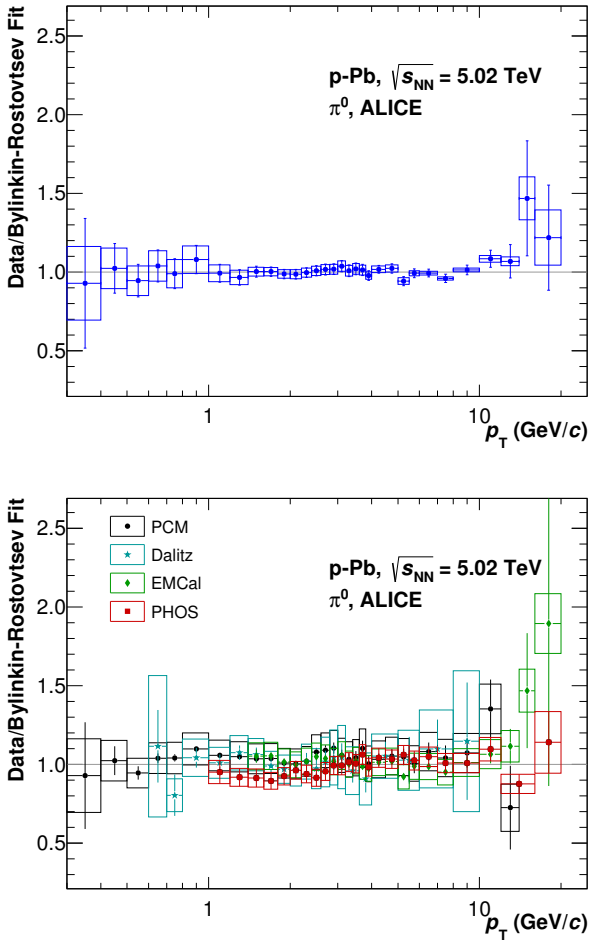

Figure 6.6: (Top) Ratio of the combined invariant π^0 meson yield in p–Pb collisions to the Bylinkin-Rostovtsev fit. (Bottom) Ratio of the individual π^0 meson yields (Dalitz, PCM, PHOS and EMCal) to the fit to the combined spectrum.

6.3 Nuclear modification factor ($R^{\pi^0}_{\rm pPb}$)

As it was mentioned in section 1.6, the p–Pb collisions provide a good test to check whether the suppression observed in Pb–Pb collisions [44] is due to the creation of the Quark-Gluon Plasma or due to the cold nuclear matter effects described in section 1.6. This can be studied by the so-called nuclear modification factor defined as:

$$R^{\pi^0}_{\rm pPb}(p_{\rm T}) = \frac{{\rm d}^2N^{\rm pPb}_{\pi^0}/{\rm d}y{\rm d}p_{\rm T}}{\langle T_{\rm pPb}\rangle \cdot {\rm d}^2\sigma^{\rm pp}_{\pi^0}/{\rm d}y{\rm d}p_{\rm T}} \tag{6.4}$$

where ${\rm d}^2N^{\rm pPb}_{\pi^0}/{\rm d}y{\rm d}p_{\rm T}$ is the invariant π^0 meson yield in p–Pb collisions and $d^2\sigma^{\rm pp}_{\pi^0}/{\rm d}y{\rm d}p_{\rm T}$ is the invariant π^0 meson cross section in pp collisions; both at the same collision center of mass energy. The $\langle T_{\rm pPb}\rangle$ is the average nuclear overlap function calculated as:

$$\langle T_{\rm pPb}\rangle = \langle N_{\rm coll}\rangle/\sigma_{NN} = 0.0983 \pm 0.0035{\rm mb}^{-1} \tag{6.5}$$

with $\langle N_{\rm coll}\rangle = 6.9 \pm 0.7$ and σ_{NN} = 70±5 mb [45].

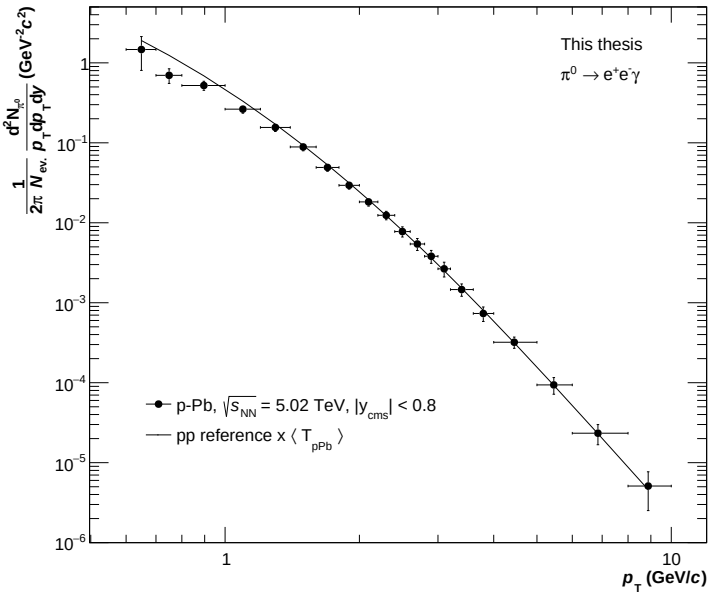

Figure 6.7: Invariant π^0 meson yield in p–Pb collisions at $\sqrt{s_{\rm NN}}$ = 5.02 TeV and the pp reference scaled by the average nuclear overlap $\langle T_{\rm pPb} \rangle$.

In the absence of nuclear effects, the $R^{\pi^0}_{\rm pPb}$ should be equal to unity for $p_{\rm T} > 2$ GeV/c, since hard partons are the main source of hadrons in that region of transverse momentum. Remember that hard partons are only created at the initial-state of the collision (section 1.5.2).

As at the time of this thesis the pp collisions at $\sqrt{s}$ = 5.02 TeV were recently taken at the LHC Run2, the pp reference was obtained by interpolation between the measured spectra in $\sqrt{s}$ = 2.76 TeV and $\sqrt{s}$ = 7 TeV. The description of the interpolation method will be given below.

6.3.1 pp reference at $\sqrt{s}$ = 5.02 TeV

Similarly to the published $R_{\rm p\text{–}Pb}$ of charged pions [166], the pp reference at $\sqrt{s}$ = 5.02 TeV was calculated bin by bin in $p_{\rm T}$ assuming a power law behaviour defined as:

$$\frac{d^2\sigma(\sqrt{s})}{dydp_{\rm T}} \propto \sqrt{s}^{n} \tag{6.6}$$

The pp spectra at $\sqrt{s}$ = 2.76 TeV and $\sqrt{s}$ = 7 TeV were taken as inputs of Eq. (6.6). Unfortunately, the pp spectra measured by this thesis were not used for the interpolation since they have low statistics, specially at the transverse momentum range of interest. Instead, the published pp spectra at $\sqrt{s}$ = 2.76 [44] TeV and at $\sqrt{s}$ = 7 [146] (both measured using the PCM method) were used. This is not that bad since they were measured at the same rapidity range ($y < 0.8$) than the one of p–Pb collisions and since part of the systematic errors of the material budget will cancel in the calculation of $R^{\pi^0}_{\rm pPb}$ in the same way as in the ration between the two measurements (see section 2.2). The extra pile-up contribution found in the pp spectrum at $\sqrt{s}$ = 7 TeV (already mentioned in section 6.1.1) was substracted.

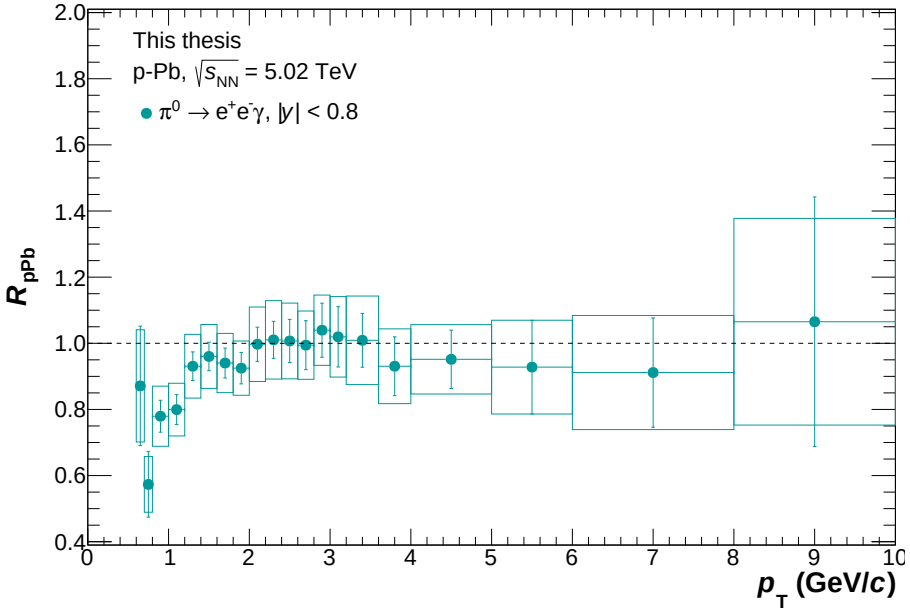

Figure 6.8: Nuclear modification factor ($R^{\pi^0}_{\rm pPb}$) measured in this thesis as a function of transverse momentum.

As a pre-requisite for the interpolation method the two input spectra should have the same $p_{\rm T}$ values. The same is required for the $R^{\pi^0}_{\rm pPb}$ calculation. However, due to the different statistics, the published pp spectrum at $\sqrt{s}$ = 2.76 TeV and the published one at $\sqrt{s}$ = 7 TeV do not agree in some intervals of transverse momentum. In order the fix the above and in order to derive one reference spectrum with the same $p_{\rm T}$ values as the measured one in p–Pb collisions at $\sqrt{s_{\rm NN}}$ = 5.02 TeV, the input pp spectra at $\sqrt{s}$ = 2.76 TeV and at $\sqrt{s}$ = 7 TeV were calculated. This was done by fitting the published ones with the Tsallis function. The systematic errors of the new $p_{\rm T}$-values (those from the calculated spectra) were obtained from the nearest one in value from the old ones (published spectra). The statistical errors were obtained by fitting the published spectra with only statistical errors.

Having calculated the two input spectra with the same $p_{\rm T}$-values, the pp reference was obtained with Eq. (6.6). The systematic errors of the pp reference for each $p_{\rm T}$ value were taken as the largest one between the two input spectra in the same $p_{\rm T}$ interval. The statistical errors were obtained by evaluating Eq. (6.6) with the calculated spectra that contain only statistical errors. As a quality check for the interpolation method, plots that show the α-dependence on $p_{\rm T}$ and the pp reference in different $p_{\rm T}$ bins can be seen in appendix D. Both show a good behaviour.

The pp reference at $\sqrt{s}$ = 5.02 TeV together with the invariant π^0 meson yield in p–Pb collisions at the same energy are shown in 6.7. For comparison, the pp reference has been scaled by the number of binary collisions ($\langle T_{\rm pPb}\rangle$). By eye, both spectra seem to be compatible for momenta $p_{\rm T} > 2$ GeV/c as expected, but this has to be confirmed when computing the $R^{\pi^0}_{\rm pPb}$.

With the obtained pp reference and the measured invariant π^0 spectrum in p–Pb collisions, one computes the $R^{\pi^0}_{\rm pPb}$ using Eq. (6.6). As it was mentioned previously, in the $R^{\pi^0}_{\rm pPb}$ one error of the material budget from the pp reference spectrum was cancelled out with the corresponding one of the invariant p–Pb π^0 yield. Moreover, the error of the $\langle T_{\rm pPb}\rangle$ was added to the systematic

errors in quadrature.

The obtained $R^{\pi^0}_{\rm pPb}$ can be seen in Fig. 6.8. The statistical errors are shown in error bars and the systematic errors are shown in error boxes. The systematic errors account for the systematic errors shown in Tab. 5.4 for the π^0 meson reconstruction in p–Pb collisions and for the systematic errors of pp reference given in [44, 146]. The $R^{\pi^0}_{\rm pPb}$ is compatible with the unity for $p_{\rm T} > 2$ GeV/c as expected in absence of medium effects. The above result reinforces the idea that the suppression observed in Pb–Pb collisions [44] at $p_{\rm T}$ >2 GeV/c is due to the Quark-Gluon Plasma formation and not to so some cold nuclear matter effects.

6.3.2 Comparison to other measurements

Comparisons to the nuclear modification factor of charged particles ($R^{\rm h}_{\rm pPb}$) [167], charged pions ($R^{\pi^\pm}_{\rm pPb}$) [166] and to the $R_{\rm RdAu}$ of the π^0 meson measured by PHENIX [168] are shown in Fig. 6.9. The $R^{\pi^0}_{\rm pPb}$ measured by this thesis agrees within the errors with the $R^{\rm h}_{\rm pPb}$ in spite that the latter shows an enhancement in the region $2\ \mathrm{GeV}/c < p_{\rm T} < 7\ \mathrm{GeV}/c$ which is due mainly to the contribution of the nuclear modification factor of protons [166]. Moreover, at larger values of transverse momenta where the contribution of the nuclear modification factor of protons becomes less significant ($p_{\rm T} \gg 7\ \mathrm{GeV}/c$), the $R^{\pi^0}_{\rm pPb}$ is closer to $R^{\rm h}_{\rm pPb}$; both compatibles with unity.

The comparison to $R^{\pi^\pm}_{\rm pPb}$ is shown in the panel (c) of the Fig. 6.9. A good agreement between the two nuclear modification factors is observed. Moreover, both $R^{\pi^0}_{\rm pPb}$ and $R^{\pi^\pm}_{\rm pPb}$ are clearly compatibles with unity for transverse momenta higher than 2 GeV/c. At $p_{\rm T} < 2\ \mathrm{GeV}/c$ the $R^{\pi^\pm}_{\rm pPb}$ is systematically below than the $R^{\pi^0}_{\rm pPb}$ but still compatible within the errors. A similar trend was observed in the comparison of the invariant yield shown in Fig. 6.3c. In the panel (c) of the Fig. 6.9 the comparison to $R_{\rm RdAu}$ of the π^0 meson measured by PHENIX at $\sqrt{s_{\rm NN}} = 200$ GeV is shown. Although the difference in energy and the collision system, both results are compatible within the errors. The $R_{\rm RdAu}$ of PHENIX does no include the error of the normalization of factor. Similarly to $R_{\rm RdAu}$, the $R^{\pi^0}_{\rm pPb}$ seems not to be significantly affected by the Cronin Effect (see section 1.6.1), however with the systematic errors, it is difficult to conclude something in that subject.

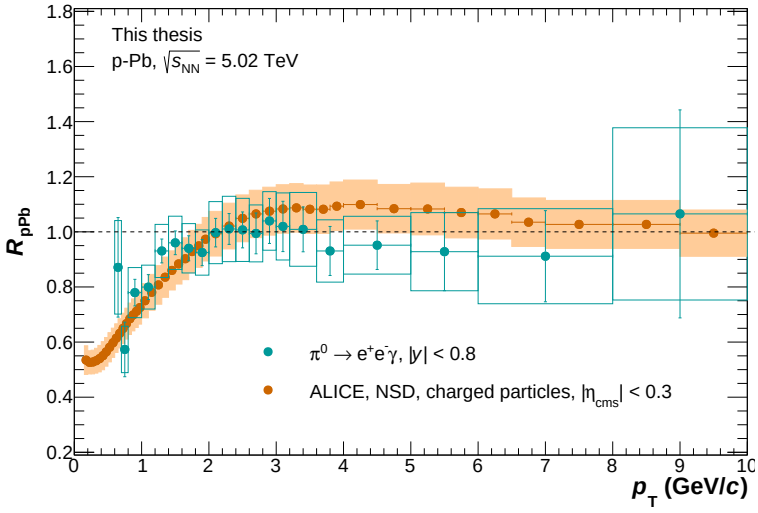

(a)

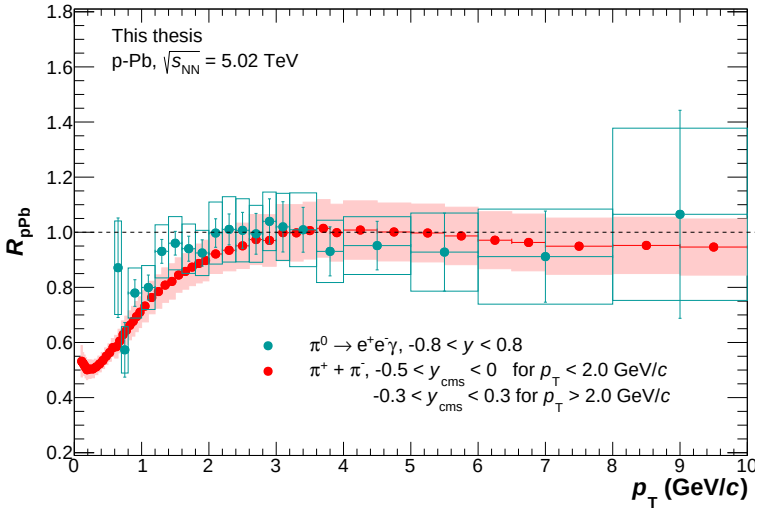

(b)

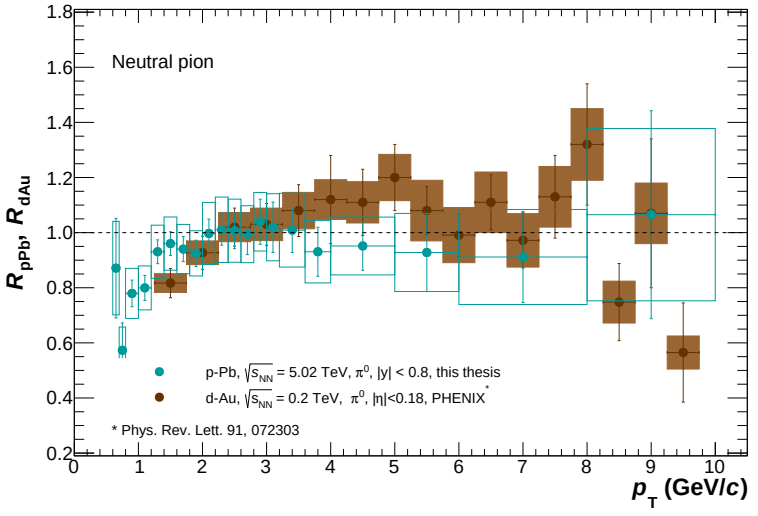

(c)

Figure 6.9: Nuclear modification factor of the π^0 meson ($R^{\pi^0}_{\mathrm{pPb}}$) measured by this thesis as a function of the transverse momentum in minimum bias compared to the nuclear modification factor of charged particles ($R^{\mathrm{h}}_{\mathrm{pPb}}$) [167] (top), compared to the nuclear modification factor of charged pions ($R^{\pi^{\pm}}_{\mathrm{pPb}}$) [166] (middle), and compared to π^0 $R_{\text{d-Au}}$ of Phenix [168] (bottom).

6.3.3 Comparison to model calculations

The $R^{\pi^0}_{\rm pPb}$ obtained in this thesis was compared to NLO pQCD EPS09s predictions [169]. The nuclear Parton Distribution Functions (nPDFs) EPS09s calculations are the result of introducing the impact-parameter dependence to the global fits EPS09 [170]. Such dependence was estimated by studying the sensibility of the nPDFs EPS09 to the nucleus A. The framework used to compute EPS09s defines nPDFs as:

$$f_i^A(x,Q^2) \equiv R_i^A(x,Q^2) f_i^p(x,Q^2) \tag{6.7}$$

where $R_i^A(x,Q^2)$ represents the nuclear modification and $f_i^p(x,Q^2)$ is the Parton Distribution Function (PDF) for a free proton which uses CTEQ6.1M set [171]. At the initial scale Q_0^2, nuclear corrections for valence quark distributions, sea quarks and for gluons are applied. Those corrections are parametrized as [170]:

$$R_i^A(x) = \begin{cases} a_0 + (a_1 + a_2 x)[\exp(-x) - \exp(-x_a)] & x \le x_a \\ b_0 + b_1 x + b_2 x^2 + b_3 x^3 & x_a \le x \le x_e \\ c_0 + (c_1 - c_2 x)(1-x)^{-\beta} & x_e \le x \le < 1 \end{cases} \tag{6.8}$$

where a_i, b_i, c_i, β, x_a and x_e are the free parameters and they are nucleus (A) dependent. The corrections take into account the cold nuclear matter effects mentioned in section 1.6: shadowing, anti-shadowing, EMC-effect, and Fermi-motion. The value of Q^2 at the initial scale was set as $Q_0^2 \equiv m_c^2 = 1.69$ GeV^2, which is the quark mass threshold. The further evolution of the nPDFs in the scale Q^2 is computed using DGLAP evolution equations.

The impact-parameter dependence of the nuclear modification to the nPDF of each parton type i en each nucleus A at each x and Q^2 in terms of a power series of the standard nuclear thickness functions T_A. The coefficients of each power of T_A are obtained by studying the dependence of the framework to A.

The comparison of the obtained $R^{\pi^0}_{\rm pPb}$ with EPS09s NL0 can be seen Fig. 6.10 for three different Fragmentation Functions (FFs). As it is observed the EPS09s agrees with the $R^{\pi^0}_{\rm pPb}$ obtained in this thesis. This can tell us that the suppression observed in [44] is not due to the initial-conditions like shadowing, anti-shadowing, EMC effect and fermi motion described in section 1.6.2.

Additionally, the $R^{\pi^0}_{\rm pPb}$ has been compared the Color-Glass Condensate (CGC) predictions [172]. The CGC allows to study saturation effects at low values of the Bjorken-x scale as the gluon recombination described in section 1.6.3. The model predictions in [172] where obtained by fitting the reduced cross-section (σ_r) data measured by Hera [173]. The CGC framework defines σ_r as [172]:

$$\sigma_r(y,x,Q^2) \equiv F_2(x,Q^2) - \frac{y^2}{1+1(1-y)^2} F_L(x,Q^2) \tag{6.9}$$

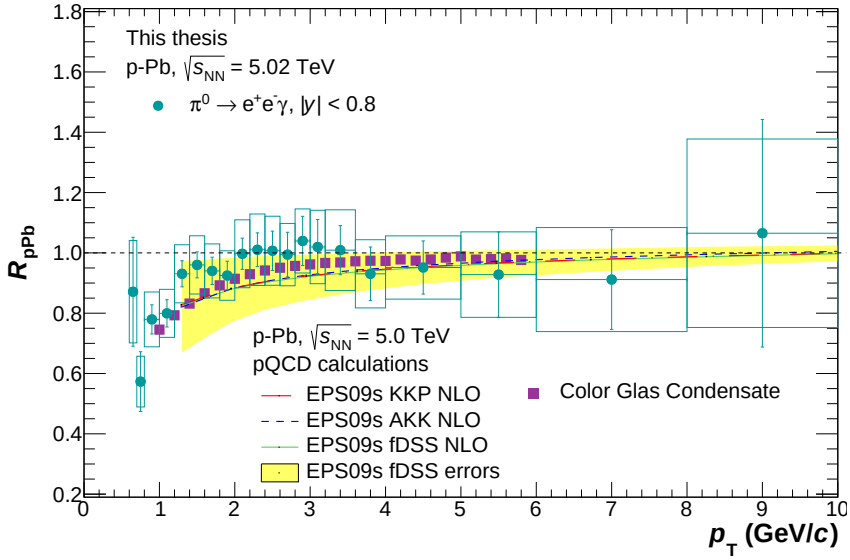

Figure 6.10: R_{pPb} from π^0 meson compared to model calculations.

where $y = Q^2/(sx)$ with $\sqrt{s}$ as the center of mass energy and F_2 and F_L are the proton structure functions defined as [172]:

$$F_2(x,Q^2) = \frac{Q^2}{4\pi^2\alpha_{em}}(\sigma_T^{\gamma^* p} + \sigma_L^{\gamma^* p}) \tag{6.10}$$

$$F_L(x,Q^2) = \frac{Q^2}{4\pi^2\alpha_{em}}\sigma_L^{\gamma^* p} \tag{6.11}$$

$$\sigma_{T,L}^{\gamma^* p}(x,Q^2) = 2 \sum_f \int dz \int \mathrm{d}^2\mathrm{b}_T |\Psi_{T,L}^{\gamma^* \to f\bar{f}}|^2 \mathcal{N}(\mathrm{b}_T, \mathrm{r}_T, x) \tag{6.12}$$

were b_T is the impact parameter and r_T is the transverse separation of the quark anti-quark. The $\mathcal{N}(\mathrm{b}_T, \mathrm{r}_T, x)$ function corresponds to the dipole-proton amplitude and it contains the QCD dynamics. The $\mathcal{N}$ is non-perturbative quantity but its evolution can be described by the Bk equation. The proton-amplitude at the initial scale ($x = x_0$) is obtained by the following parametrization based on the McLerran-Venugopalan model [174]:

$$\mathcal{N}(\mathrm{r}_T) = 1 - \exp\left[-\frac{(\mathrm{r}_T^2 Q_{s0}^2)^\gamma}{4} \ln\left(\frac{1}{|\mathrm{r}_T|\Lambda_{\rm QCD}} + e_c \cdot e \right) \right] \tag{6.13}$$

The dipole nucleus targeting:

$$\mathcal{N}^A(\mathrm{r}_T, \mathrm{b}_T) = \left[1 - \exp\left(-\frac{A T_A(\mathrm{b}_T)}{2} \sigma_{\rm p}^{\rm dip} \right) \right] \tag{6.14}$$

The comparison with Color-Glass Condesate is shown in Fig. 6.10. A good agreement is observed.

Chapter 7

Summary and Outlook

In this thesis, the differential invariant π^0 meson yield spectra in pp collisions at $\sqrt{s}$ = 2.76 TeV and at $\sqrt{s}$ = 7 TeV and in p–Pb collisions at $\sqrt{s_{\rm NN}}$ = 5.02 TeV were presented. The differential invariant π^0 meson cross section spectra in pp collisions at $\sqrt{s}$ = 2.76 TeV and at $\sqrt{s}$ = 7 TeV were also presented and compared to model calculations. The measured spectrum at $\sqrt{s_{\rm NN}}$ = 5.02 TeV was used to compute the nuclear modification factor ($R^{\pi^0}_{\rm pPb}$). The pp reference at $\sqrt{s}$ = 5.02 TeV needed for $R^{\pi^0}_{\rm pPb}$ was obtained by interpolation.

The measurement of the π^0 meson production has been carried out by detecting the final-state products of its Dalitz decay channel ($\pi^0 \rightarrow \gamma^*\gamma \rightarrow e^+e^-\gamma$) in the ALICE central barrel. The two primary electrons were reconstructed using the TPC and ITS detectors. The particle identification was carried out by using the specific energy loss ($\mathrm{d}E/\mathrm{d}x$) in the TPC detector. On the other hand, photons (γ) were reconstructed using the Photon Conversion Method (PCM) which detects photons through their conversion products in the ALICE central barrel. The PCM requires the reconstruction of a secondary vertex, commonly known as V^0. The V^0s were reconstructed using the On-the-Fly V^0 finder algorithm. The secondary electrons were identified using the ($\mathrm{d}E/\mathrm{d}x$) measurement in the TPC, similarly to primary electrons.

The π^0 meson was obtained by computing the invariant mass distribution of the $\gamma^*\gamma$ pairs. The combinatorial background was estimated using the mixed event technique which combines virtual photons with photons from different events. After background subtraction, the π^0 meson signal was fitted with a gaussian function convoluted with an exponential and a linear function. The exponential function was included to take into account the long bremsstrahlung tail at the left side of the π^0 meson signal peak. The linear function was included to subtract a possible residual background below the π^0 meson signal. The π^0 meson raw yield spectra at the three energies under study were obtained by integrating the π^0 meson signal. The integration windows were obtained from the obtained fit parameters.

Using Monte Carlo simulations that implements PYTHIA, PHOJET and HIJING as particle generators, the π^0 meson raw yield spectra were corrected by acceptance and efficiency. Moreover, the contamination from the 2γ decay case in the π^0 was computed and subtracted from the raw yield spectra. The systematic errors were computed by varying each cut used in the virtual photon and in the photon reconstruction and in the π^0 meson signal extraction.

The measured spectra were fitted with the Tsallis function. A nice agreement was observed in the three analyzed systems. The fit parameters obtained in pp collisions at $\sqrt{s}$ = 2.76 TeV are in agreement whitin the errors with the ones published by ALICE in pp at the same center of mass energy. For pp collisions at $\sqrt{s}$ = 7 TeV sligly different fit parameters were obtained with respect to the published ones by ALICE at the same collision system. However, the fit parameters published by ALICE were obtained before an extra pile up contribution was found in the pp spectrum, therefore, it would be interesting to compare with the updated one.

As a consistency check, the measured π^0 meson spectra were compared to the others independent methods for π^0 meson reconstruction existing in ALICE: PCM, PHOS and EMCal. A good agreement was observed at the three energies under study. The π^0 meson spectra were also compared to the charged pion spectra. For pp collisions at $\sqrt{s}$ = 7 TeV, the comparison shows a good agreement for 0.8 $\mathrm{GeV}/c < p_{\mathrm{T}} <$ 7 GeV/c. For pp collisions at $\sqrt{s}$ = 2.76 TeV a good agreement is observed in the p_{T} range of 0.8 $\mathrm{GeV}/c < p_{\mathrm{T}} <$ 2 GeV/c where the spectrum has enough statistics. On the other hand, in p–Pb collisions at $\sqrt{s_{\mathrm{NN}}}$ = 5.02 TeV a good agreement was observed for 0.8 $\mathrm{GeV}/c < p_{\mathrm{T}} <$ 10 GeV/c. However, in the p_{T} range $1.0 < p_{\mathrm{T}} < 3.0$ GeV/c, our p–Pb spectrum is systematically above $\sim$ 10 % from the charged pion spectrum but compatible within the systematic errors.

The differential invariant π^0 meson cross section in pp collisions at the two energies under study were compared with pQCD model calculations that uses MSTW PDFs with the new release of DSS14 FFs. For both energies, the theory seems to reproduce the shape of the spectra in 2 < p_{T} < 5 GeV/c. Moreover, in that region of p_{T}, the measured spectrum in pp collisions at $\sqrt{s}$ = 2.76 TeV is in agreement with the theory although in the limit of the systematic errors. Additionally, the pp spectrum at $\sqrt{s}$ = 2.76 TeV was also compared to PYTHIA 8 Tune 4C obtaining similar results to the ones obtained with pQCD models in the p_{T} region of 0.8 < p_{T} < 5 GeV/c.

In order to disentangle cold nuclear matter effects from final effects in the π^0 meson suppression observed for momenta higher than 2 GeV/c in Pb–Pb collisions at $\sqrt{s}$ = 2.76 TeV, the nuclear modification factor ($R^{\pi^0}_{\mathrm{pPb}}$) was obtained using the measured p–Pb spectrum. The obtained ($R^{\pi^0}_{\mathrm{pPb}}$) is compatible with unity at $p_{\mathrm{T}} >$ 2 GeV/c implying that the observed suppression in Pb–Pb collisions is due to the formation of the Quark-Gluon Plasma. Moreover, the obtained $R^{\pi^0}_{\mathrm{pPb}}$ was compared to the ones for charged particles and charged pions showing a good agreement with them. Additionally, EPS09s and Color-Glass Condensate model reproduce the $R^{\pi^0}_{\mathrm{pPb}}$ obtained in this thesis.

Appendix A

List of runs

A.1 Run list for pp collisions at $\sqrt{s}$ = 2.76 TeV

Data
146746, 146747, 146748, 146801, 146802, 146803, 146804, 146805, 146806, 146807
146817, 146824, 146856, 146858, 146859, 146860

MC (LHC12f1a)
146746, 146747, 146748, 146801, 146802, 146803, 146804, 146805, 146806, 146807
146817, 146824, 146856

MC (LHC12f1b)
146746, 146747, 146748, 146801, 146802, 146803, 146804, 146805, 146806, 146807
146817, 146824, 146856

A.2 Run list for pp collisions at $\sqrt{s}$ = 7 TeV

Data LHC10b pass2
114931, 115186, 115193, 115310, 115318, 115322, 115328, 115393, 115401, 116102
116288, 116402, 116403, 116562, 116571, 116574, 116643, 116645, 117048, 117050
117052, 117053, 117059, 117060, 117063, 117092, 117099, 117109, 117112, 117116
117220, 117222

Data LHC10c pass2
119159, 119161, 119163, 119841, 119844, 119845, 119846, 119849, 119853, 119856
119859, 119862, 120067, 120069, 120072, 120073, 120076, 120079, 120244, 120503
120505, 120616, 120617, 120671, 120741, 120750, 120758, 120820, 120821, 120822
120823, 120824, 120825, 120829

Data LHC10d pass2
122374, 122375, 124751, 125023, 125085, 125097, 125100, 125101, 125134, 125296
125628, 125630, 125632, 125633, 125842, 125843, 125844, 125847, 125848, 125849
125850, 125851, 125855, 126004, 126007, 126008, 126073, 126078, 126081, 126082
126088, 126090, 126097, 126158, 126160, 126168, 126283, 126284, 126285, 126351

126352, 126359, 126403, 126404, 126405, 126406, 126407, 126408, 126409, 126422
126424, 126425, 126432, 126437

Data LHC10e pass2
127712, 127714, 127718, 127822, 127933, 127935, 127936, 127937, 127940, 127941
127942, 128185, 128186, 128189, 128191, 128192, 128260, 128366, 128452, 128483
128486, 128494, 128495, 128503, 128504, 128507, 128582, 128605, 128609, 128611
128615, 128677, 128678, 128777, 128778, 128820, 128823, 128824, 128835, 128836
128843, 128850, 128853, 128855, 128913, 129512, 129513, 129514, 129520, 129523
129527, 129528, 129540, 129586, 129587, 129599, 129639, 129641, 129647, 129650
129652, 129653, 129654, 129659, 129666, 129667, 129723, 129725, 129726, 129729
129735, 129736, 129738, 129742, 129744, 129959, 129960, 129961, 129983, 130149
130157, 130158, 130172, 130178, 130179, 130342, 130343, 130354, 130356, 130375
130480, 130517, 130519, 130696, 130704, 130793, 130795, 130798, 130799, 130834
130840, 130844, 130847, 130848

MC (LHC10d1)
115186, 115310, 115318, 115322, 115328, 115393, 115401, 116102, 116288, 116402
116403, 116562, 116571, 116574, 116643, 116645, 117048, 117050, 117052, 117053
117059, 117060, 117063, 117092, 117099, 117109, 117112, 117116, 117220, 117222

MC (LHC10d2)

114931, 115186, 115193, 115310, 115318, 115322, 115328, 115393, 115401, 116102
116288, 116402, 116403, 116562, 116571, 116574, 116643, 116645, 117048, 117050
117052, 117053, 117059, 117060, 117063, 117092, 117099, 117109, 117112, 117116
117220, 117222

MC (LHC10d4)

119159, 119161, 119163, 119841, 119844, 119845, 119846, 119853, 119856, 119859
119862, 120067, 120069, 120072, 120073, 120076, 120079, 120244, 120503, 120505
120616, 120617, 120671, 120741, 120750, 120758, 120820, 120821, 120822, 120823
120825, 120829

MC (LHC10d4a)

119159, 119161, 119163, 119841, 119842, 119844, 119845, 119846, 119849, 119853
119856, 119859, 119862, 120067, 120069, 120072, 120073, 120076, 120079, 120244
120503, 120504, 120505, 120616, 120617, 120671, 120741, 120750, 120758, 120820
120821, 120822, 120823, 120825

MC (LHC10e20)

127719, 127940, 128913, 129599, 129639, 129641, 129654, 129659, 129666, 129667
129723, 129725, 129726, 129729, 129735, 129736, 129738, 129742, 129744, 129959
129960, 129961, 129983, 130149, 130157, 130158, 130172, 130178, 130179, 130342

130343, 130354, 130356, 130375, 130480, 130517, 130519, 130520, 130601, 130608
130696, 130704

MC (LHC10e21)

128263, 128778, 128913, 129599, 129639, 129641, 129654, 129659, 129666, 129667
129723, 129725, 129726, 129729, 129735, 129736, 129738, 129742, 129744, 129959
129960, 129961, 129983, 130149, 130157, 130158, 130172, 130178, 130179, 130342
130343, 130354, 130356, 130375, 130480, 130517, 130519, 130520, 130601, 130608
130696, 130704, 130793, 130795, 130798, 130799, 130834, 130840, 130842, 130844
130847, 130848

MC (LHC10f6)

122374, 122375, 124751, 125023, 125085, 125097, 125100, 125101, 125134, 125849
125850, 125851, 125855, 126004, 126007, 126073, 126078, 126081, 126082, 126160
126168, 126283, 126284, 126285, 126351, 126407, 126422, 126424, 126425, 126432
126437

MC (LHC10f6a)

122374, 122375, 124751, 125023, 125085, 125097, 125100, 125101, 125134, 125296
125628, 125630, 125632, 125633, 125842, 125843, 125844, 125847, 125848, 125849
125850, 125851, 125855, 126004, 126007, 126008, 126073, 126078, 126081, 126082
126088, 126090, 126097, 126158, 126160, 126168, 126283, 126284, 126285, 126359
126403, 126404, 126405, 126406, 126407, 126408, 126409, 126422, 126424, 126425
126432, 126437

A.3 Run list for p–Pb collisions at $\sqrt{s}$ = 5.023 TeV

Data LHC13b pass3

195344, 195351, 195389, 195391, 195478, 195479, 195480, 195481, 195482, 195483

Data LHC13c pass2

195529, 195531, 195566, 195567, 195568, 195592, 195593, 195596, 195633, 195635
195644, 195673, 195675, 195677

MC LHC14b2

195344, 195351, 195389, 195391, 195478, 195479, 195480, 195481, 195482, 195483
195529, 195531, 195566, 195567, 195568, 195592, 195593, 195596, 195633, 195635
195644, 195673, 195675, 195677

Appendix B

QA plots

For a better comparison, the quantities shown in this appendix (except Fig. B.5) correspond to electron and positron candidates that contribute to the π^0 meson signal. This means, that only those candidates with $0.1 < M_{e^+e^-\gamma} < 0.145$ GeV/c were taken into account.

B.1 Primary electrons

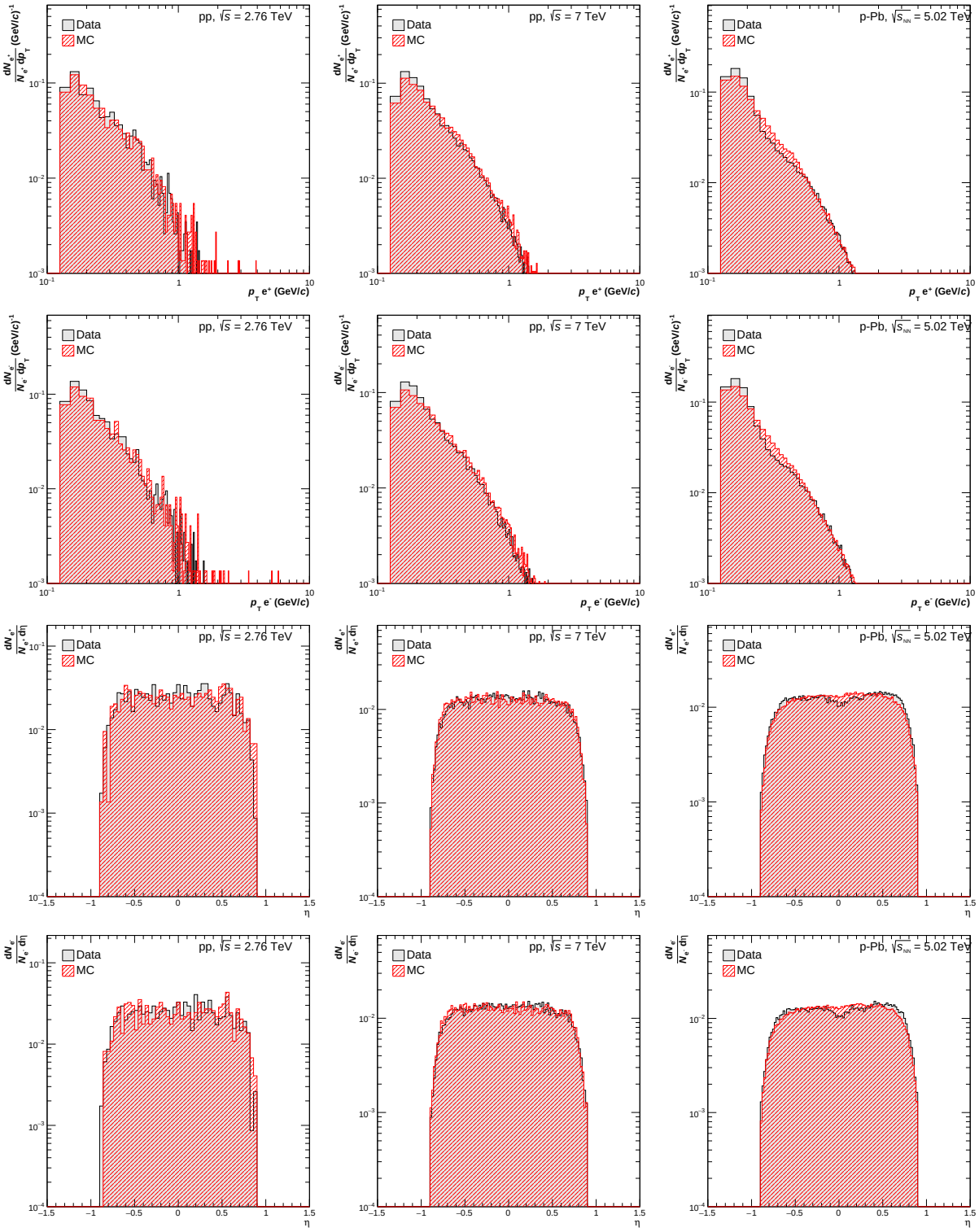

Figure B.1: Distribution of p_{T} and η variables of primary electrons and positrons candidates for Monte Carlo simulations (red) and data (gray). These variables are used for primary track selection.

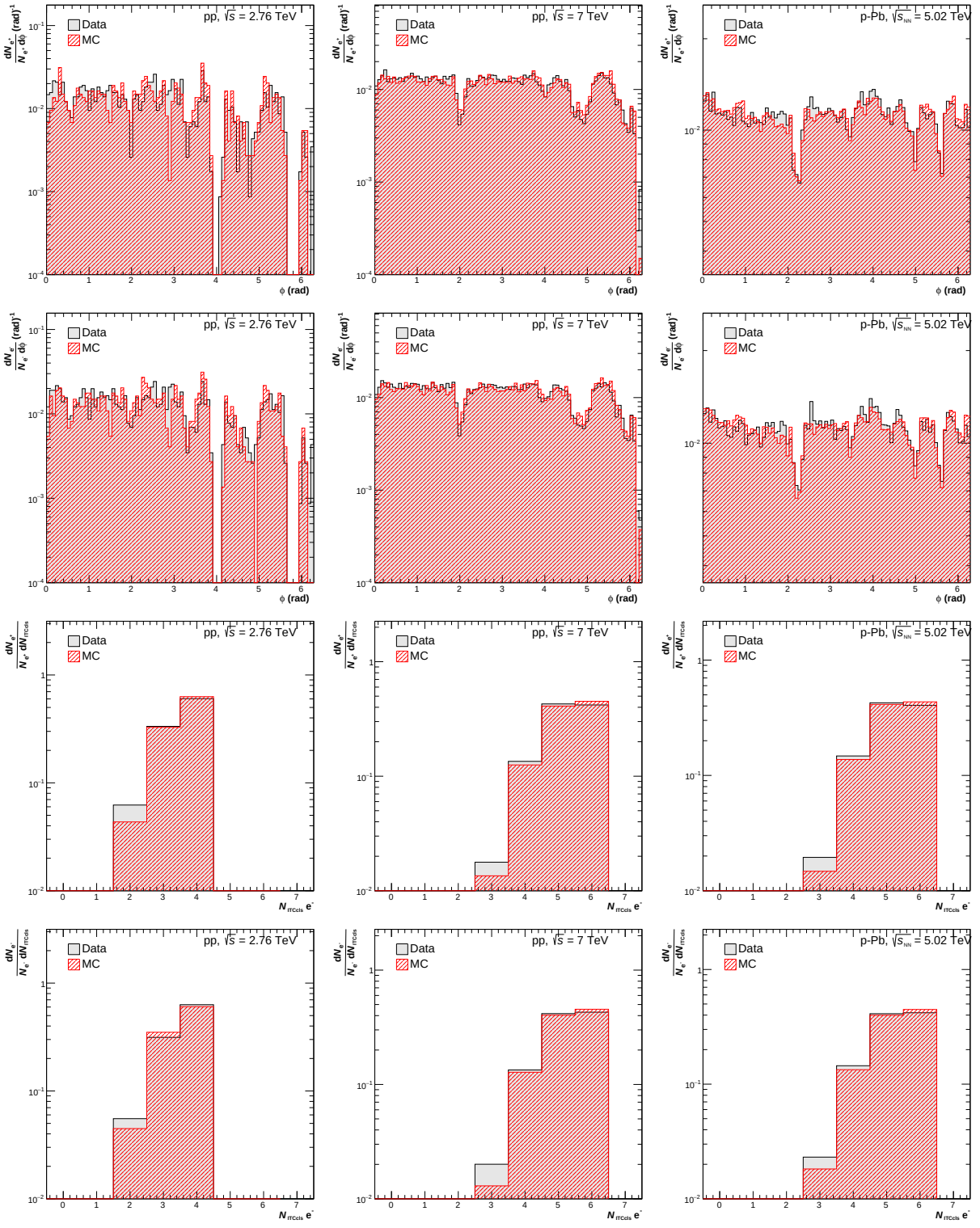

Figure B.2: Distribution of ϕ and N_{ITScls} variables of primary electron and positrons candidates for Monte Carlo simulations (red) and data (gray). These variables are used for primary track selection.

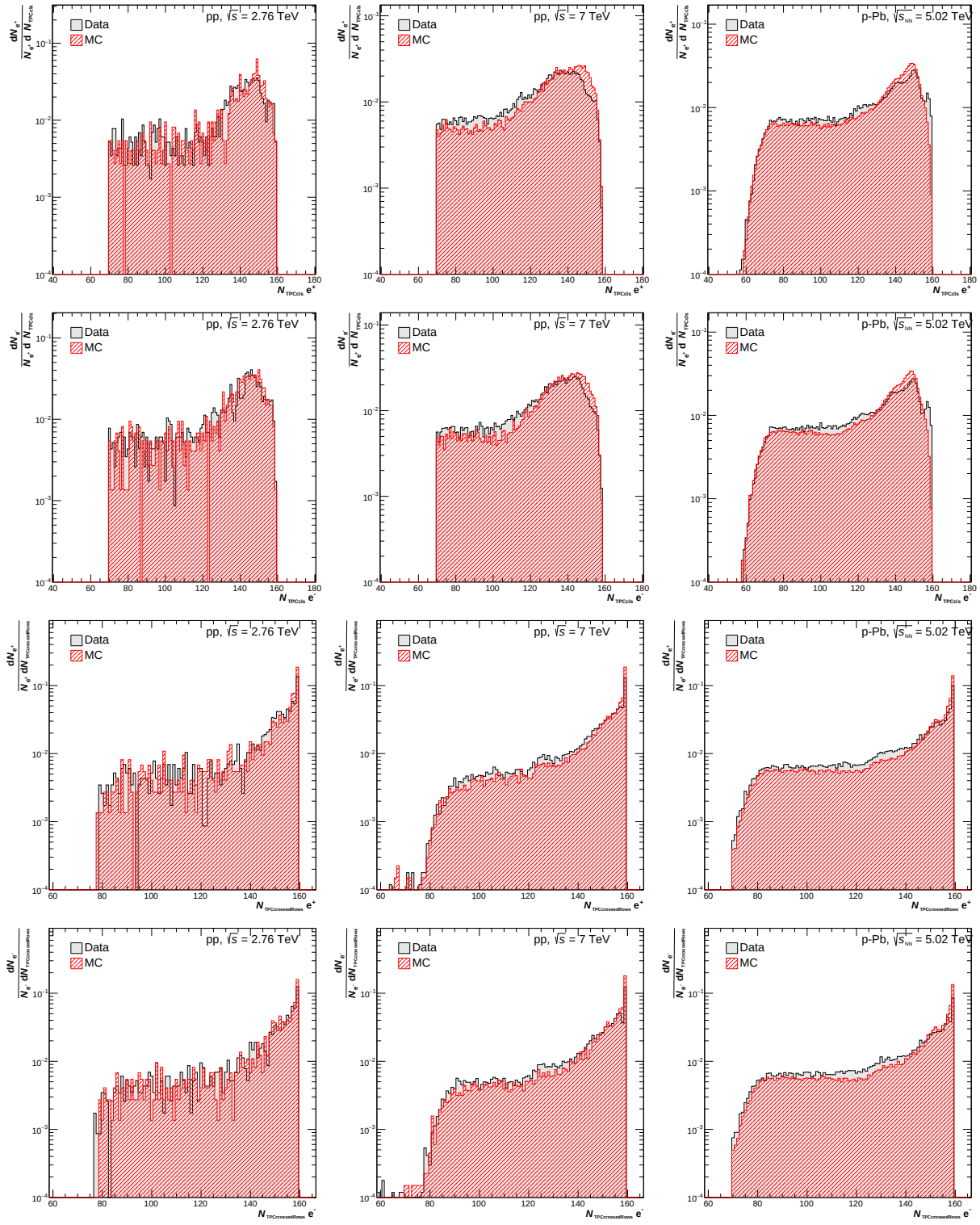

Figure B.3: Distribution of the N_{TPCcls} and $N_{\mathrm{TPCcrossedRows}}$ variables of primary electrons and positrons candidates for Monte Carlo simulations (red) and data (gray). These variables are used for primary track selection.

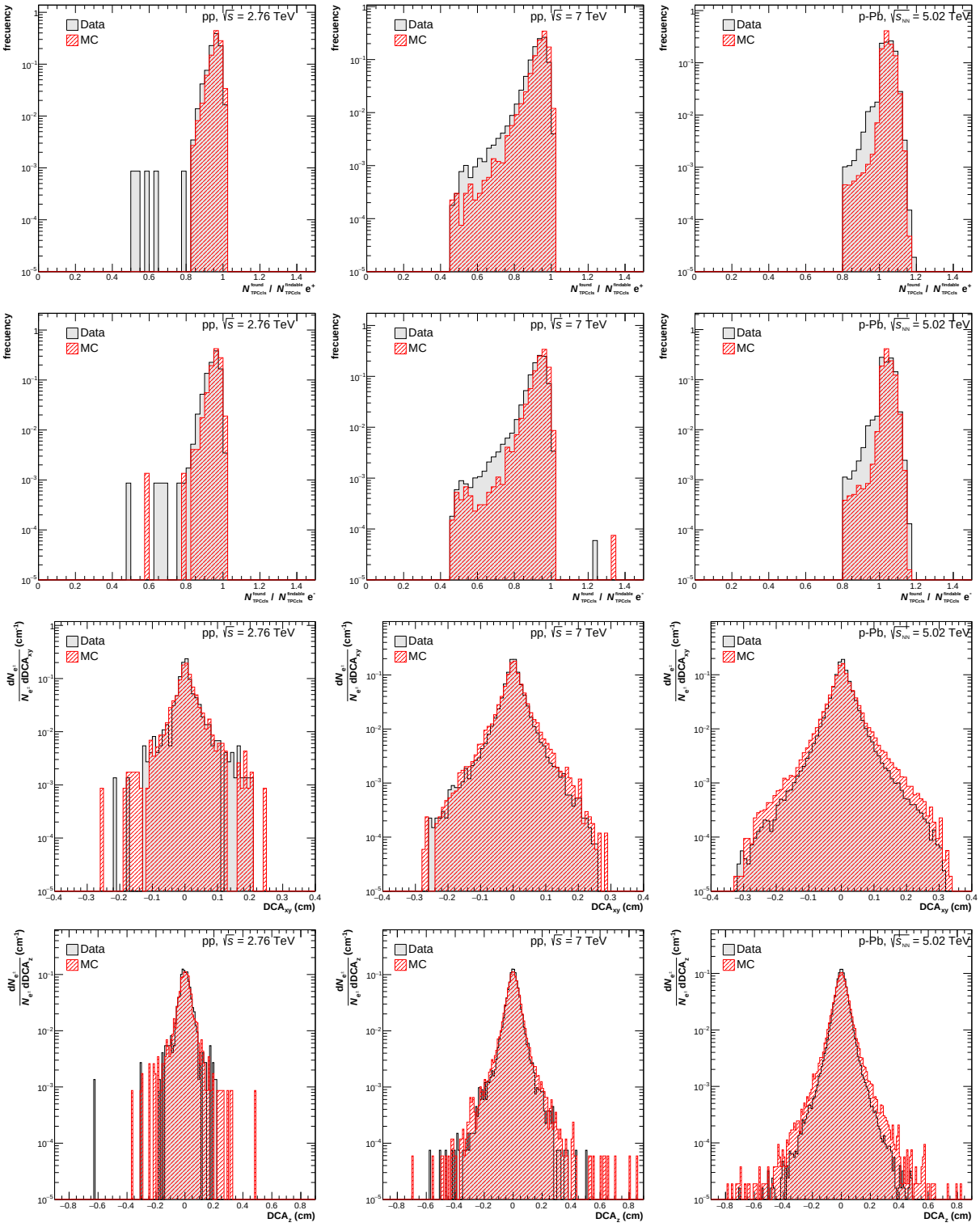

Figure B.4: Distribution of $N_{\mathrm{TPCcls}}^{\mathrm{findable}}$, DCA$_{xy}$ and DCA$_z$ variables of primary tracks for Monte Carlo simulations (red) and data (gray). These variables are used for primary track selection. The DCA$_{xy}$ and DCA$_z$ are filled with electrons and positrons.

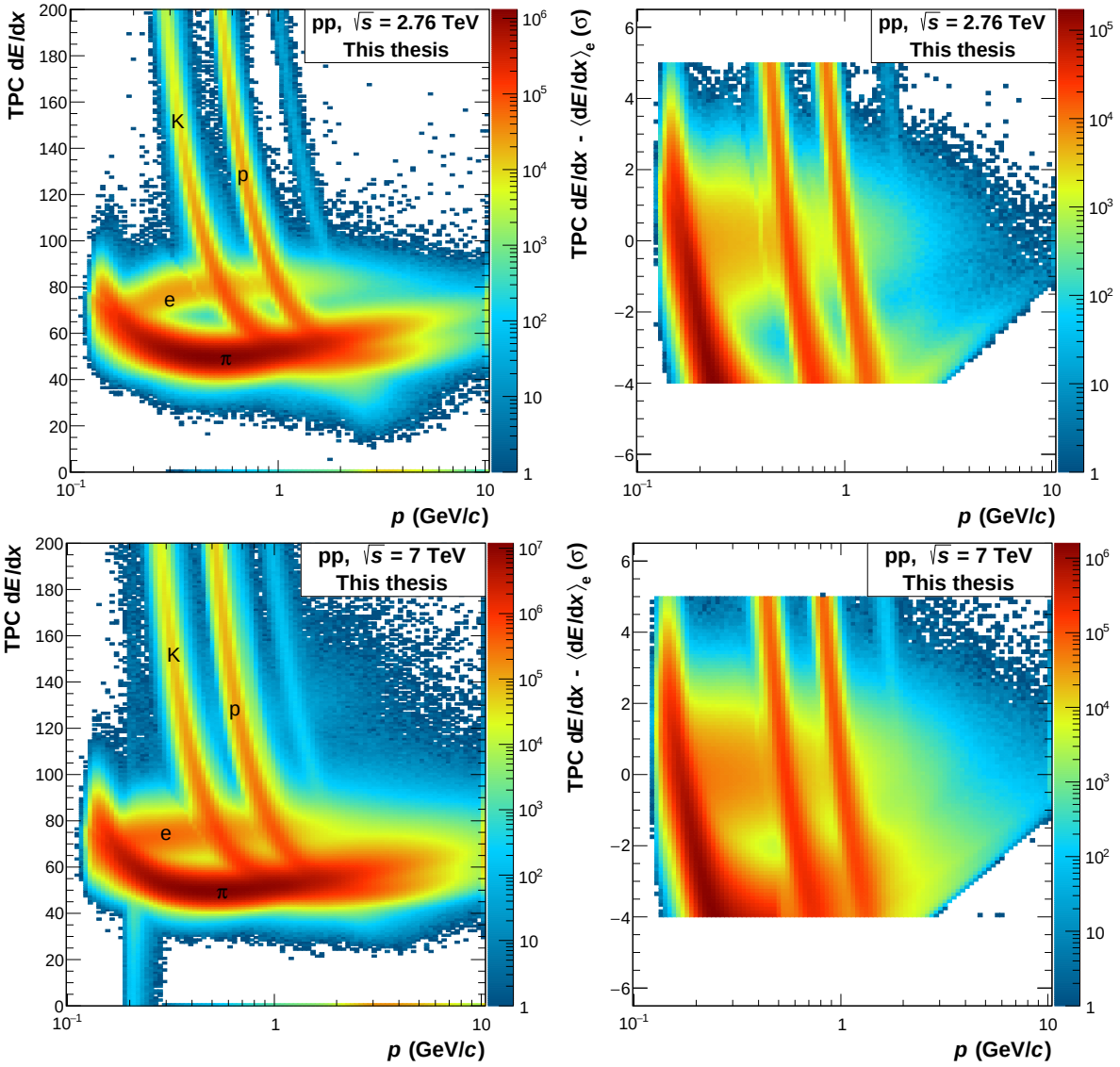

Figure B.5: Compatibility of the measured $\mathrm{d}E/\mathrm{d}x$ to the parametrized Bethe-Bloch band of electrons (expresed in number of standard deviations) as a function of momentum for pp collisions at $\sqrt{s}$ = 2.76 TeV (top) and at $\sqrt{s}$ = 7 TeV (bottom).

B.2 Secondary electrons

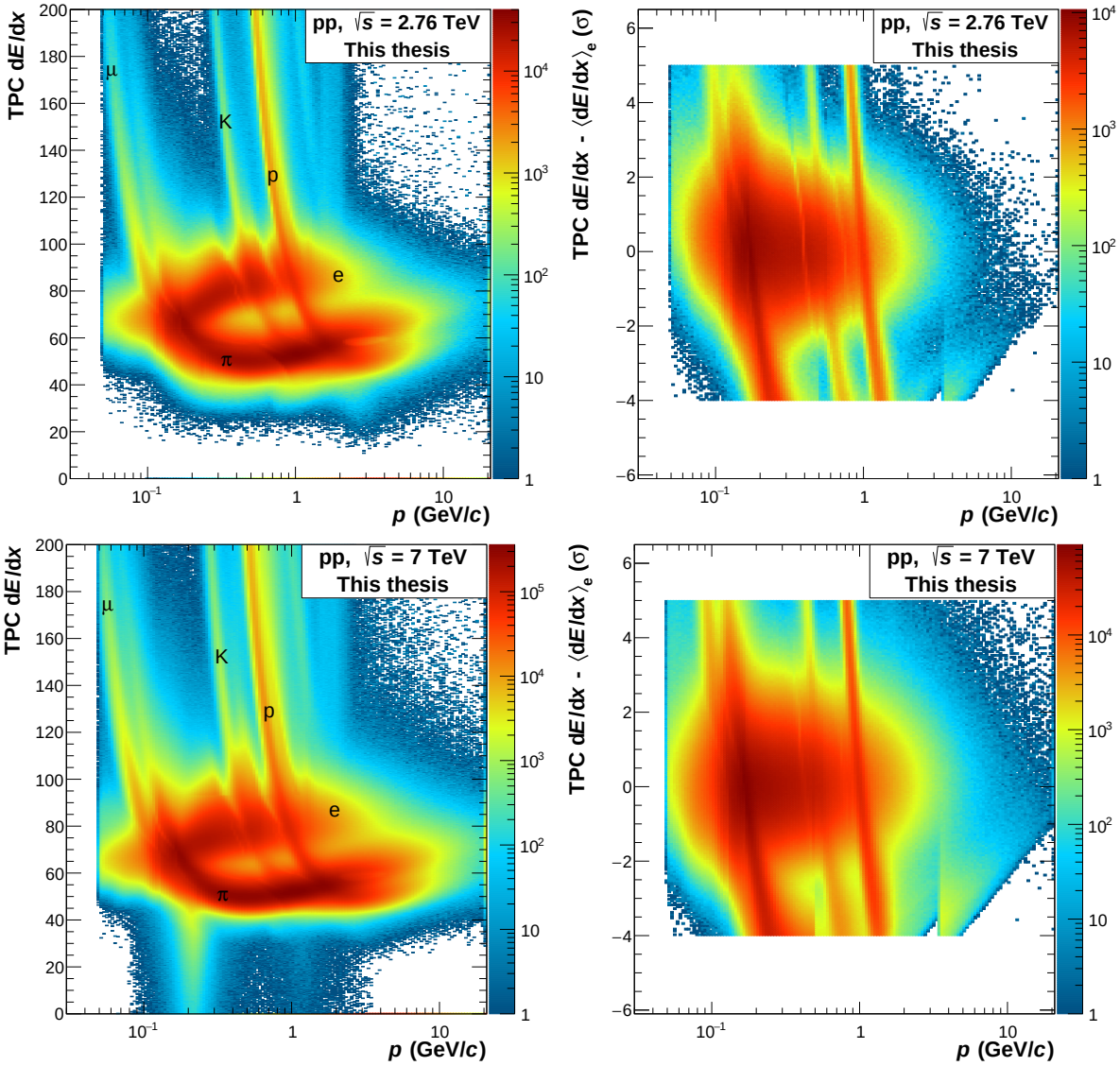

Figure B.6: Specific energy loss as a function of momentum for positive and negative tracks from V^0 candidates before PID cuts (left). Compatibility of the measured $\mathrm{d}E/\mathrm{d}x$ to the parametrized Bethe-Bloch band of electrons from V^0 candidates as a function of momentum after PID cuts (right). The data correspond to pp collisions at $\sqrt{s} = 2.76$ TeV (top) and at $\sqrt{s} = 7$ TeV (bottom).

Appendix C

C. Neutral Meson analysis plots

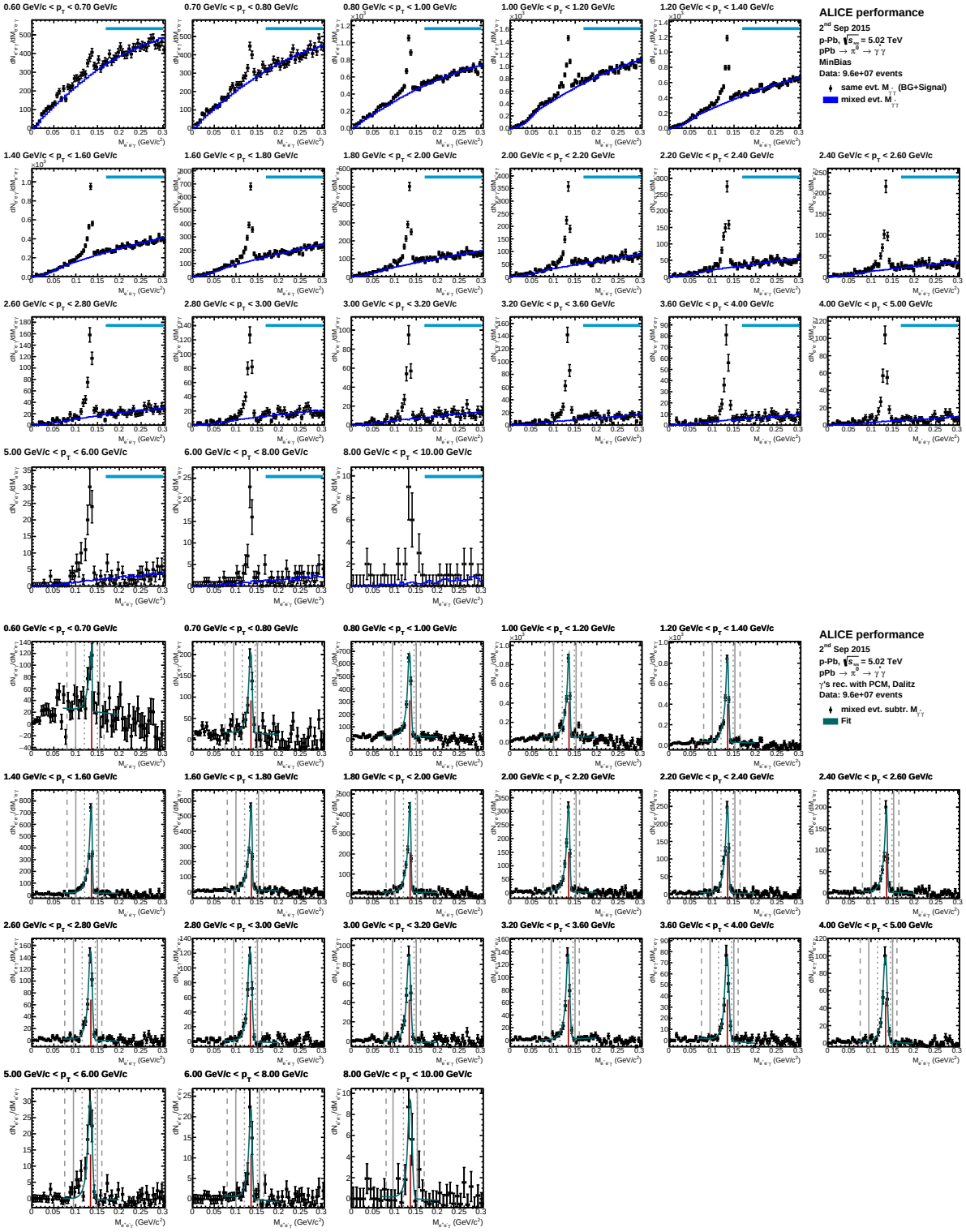

Figure C.1: Invariant mass distribution $M_{e^+e^-\gamma}$ with background (top) and after background subtraction (bottom) for p–Pb at $\sqrt{s_{\mathrm{NN}}} = 5.02$ TeV.

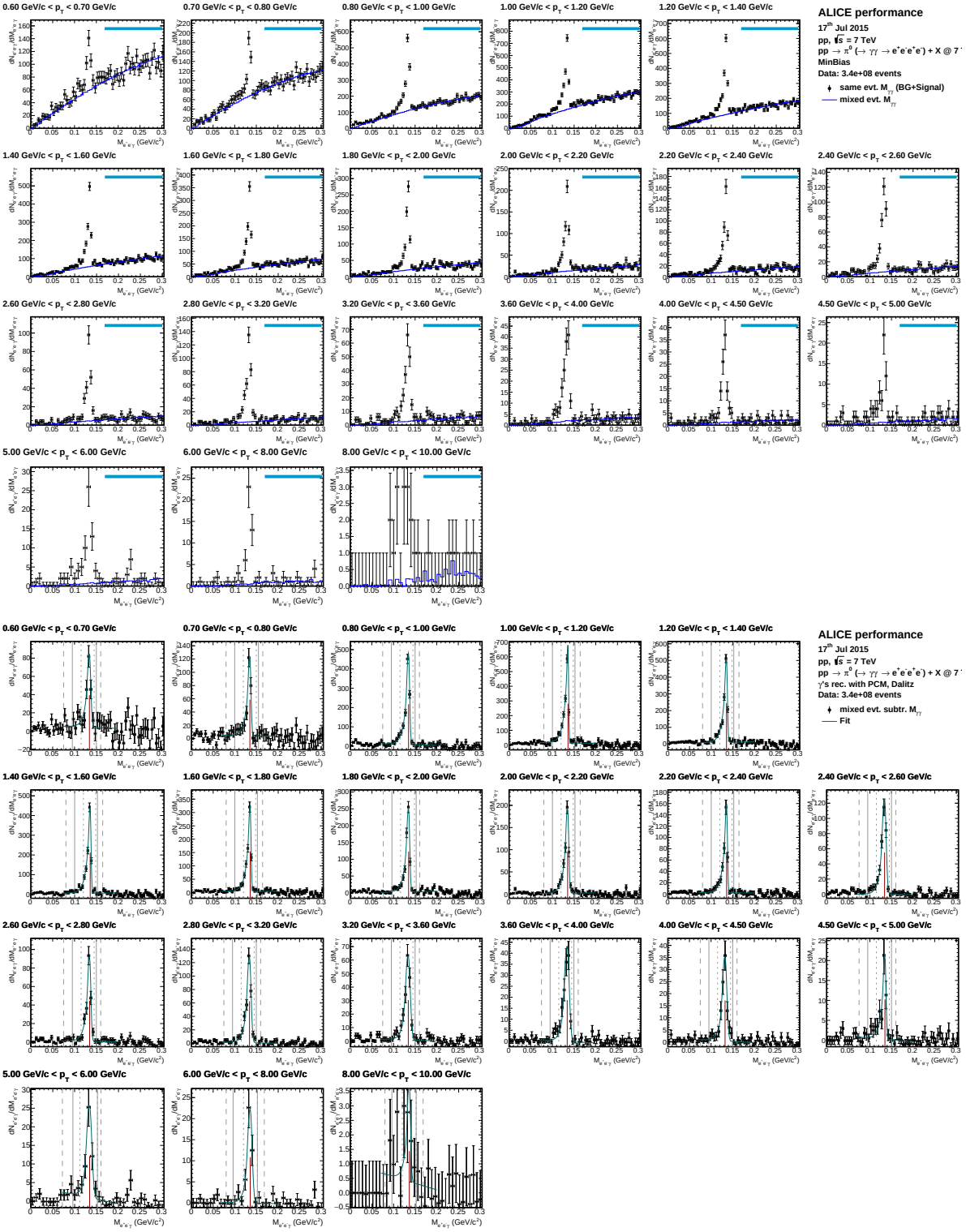

Figure C.2: Invariant mass distribution $M_{e^+e^-\gamma}$ with background (top) and after background subtraction (bottom) for pp at $\sqrt{s} = 7$ TeV.

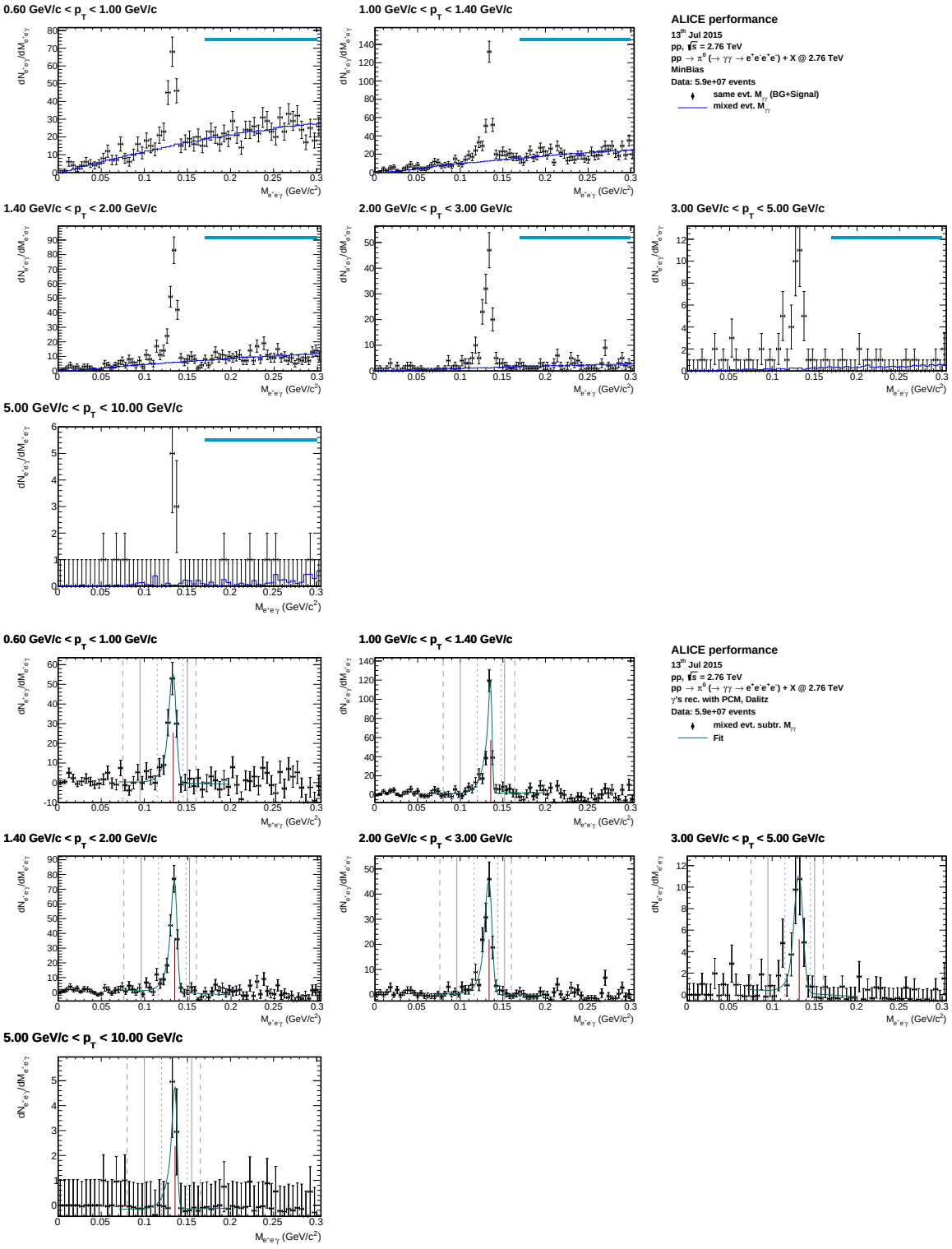

Figure C.3: Invariant mass distribution $M_{e^+e^-\gamma}$ with background (top) and after background subtraction (bottom) for pp at $\sqrt{s} = 2.76$ TeV.

Appendix D

D. Interpolation plots

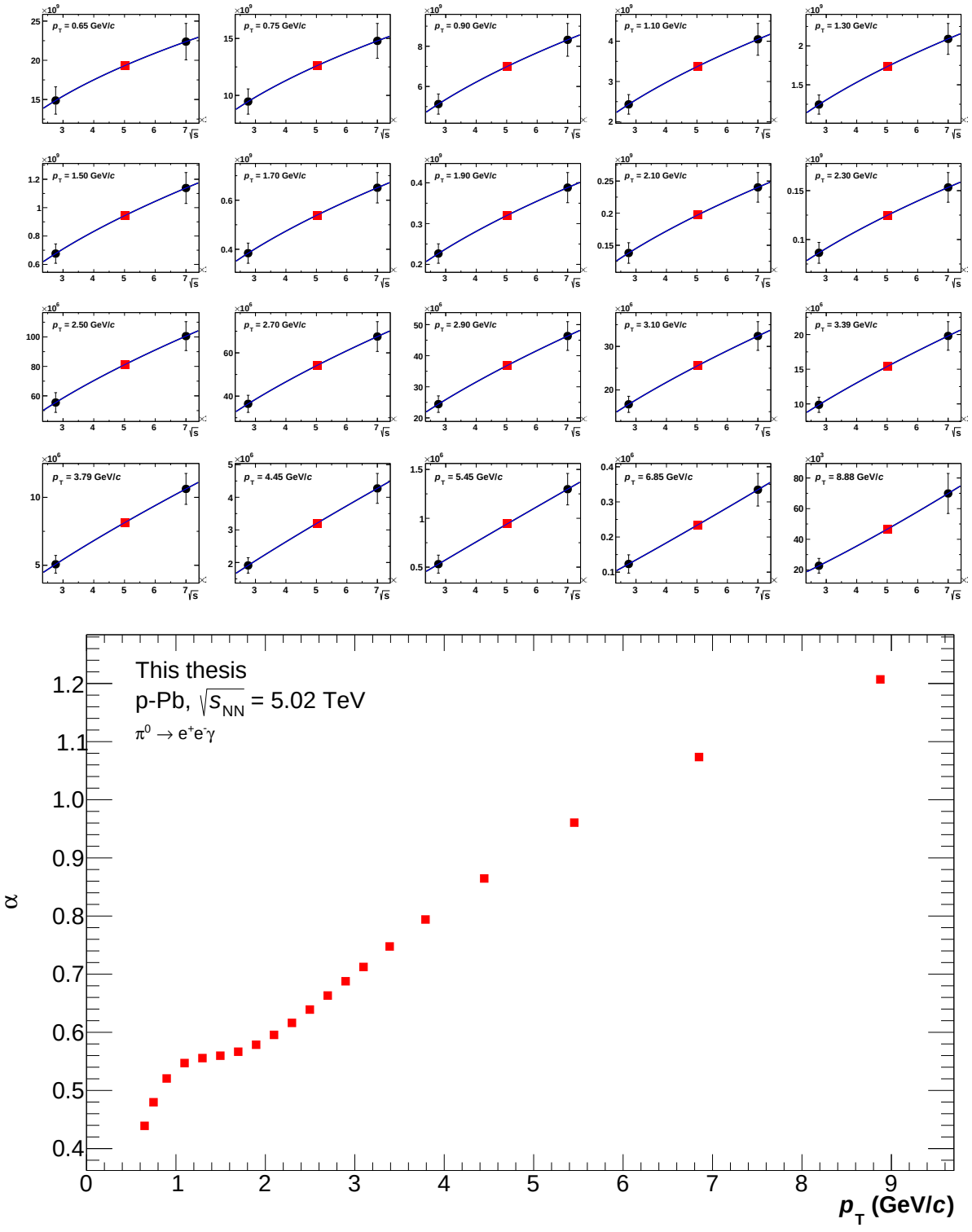

Figure D.1: (Top) Power law fits in different bins of p_{T}. (Botton) exponent α obtained for each p_{T} bin during the calculation of the pp reference at $\sqrt{s}$=5.02 TeV.

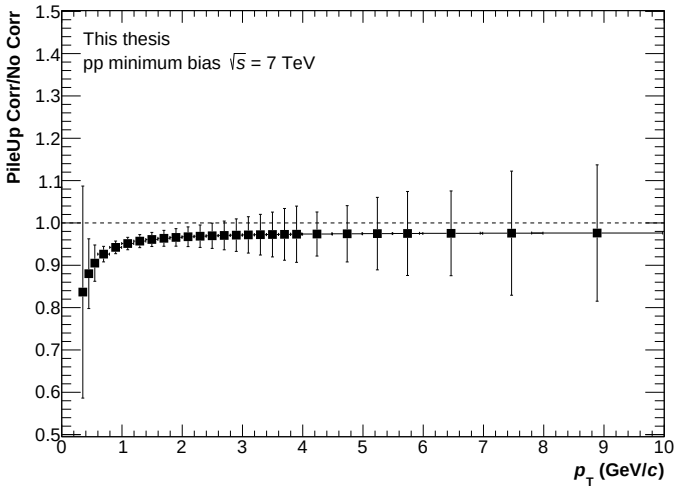

Figure D.2: Ratio between the published pp spectrum at $\sqrt{s}$ = 7 TeV before pile-up correction and after correction.

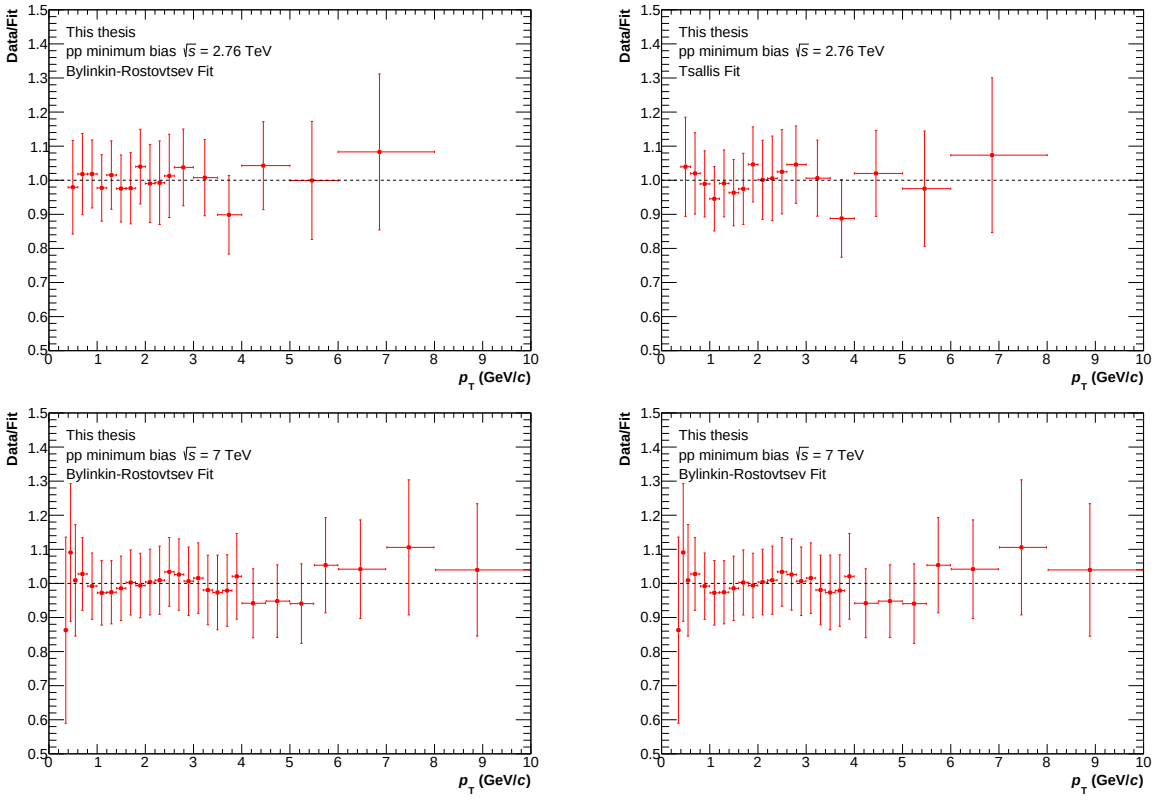

Figure D.3: (Top) Ratio to fit of the published π^0 spectrum in pp collisions at $\sqrt{s}$ = 2.76 TeV. (Botton) Ratio to fit of the published π^0 spectrum at $\sqrt{s}$ = 7 TeV. The resulting fits were used to calculate the pp spectra with the same p_{T} intervals. Bylinkin-Rostovtsev were used as a default.

Bibliography

[1] Fayyazuddin and Riazuddin. *Modern introduction to particle physics*. River Edge, N.J: World Scientific, 2012. ISBN: 9789814338837. URL: http://www-spires.fnal.gov/spires/find/books/www?cl=QC793.2.F39::2012.

[2] W. N. Cottingham and D. A. Greenwood. *An introduction to the standard model of particle physics*. Cambridge University Press, 2007. ISBN: 9780511271366, 9780521852494.

[3] K. A. Olive et al. "Review of Particle Physics". In: *Chin. Phys.* C38 (2014), p. 090001. DOI: 10.1088/1674-1137/38/9/090001.

[4] *The standard package*. http://public-archive.web.cern.ch/public-archive/en/Science/StandardModel-en.html.

[5] F. Englert and R. Brout. "Broken Symmetry and the Mass of Gauge Vector Mesons". In: *Phys. Rev. Lett.* 13 (1964), pp. 321–323. DOI: 10.1103/PhysRevLett.13.321.

[6] Peter W. Higgs. "Broken symmetries, massless particles and gauge fields". In: *Phys. Lett.* 12 (1964), pp. 132–133. DOI: 10.1016/0031-9163(64)91136-9.

[7] Peter W. Higgs. "Broken Symmetries and the Masses of Gauge Bosons". In: *Phys. Rev. Lett.* 13 (1964), pp. 508–509. DOI: 10.1103/PhysRevLett.13.508.

[8] Serguei Chatrchyan et al. "Observation of a new boson at a mass of 125 GeV with the CMS experiment at the LHC". In: *Phys. Lett.* B716 (2012), pp. 30–61. DOI: 10.1016/j.physletb.2012.08.021. arXiv:1207.7235 [hep-ex].

[9] Georges Aad et al. "Observation of a new particle in the search for the Standard Model Higgs boson with the ATLAS detector at the LHC". In: *Phys. Lett.* B716 (2012), pp. 1–29. DOI: 10.1016/j.physletb.2012.08.020. arXiv:1207.7214 [hep-ex].

[10] Steven Carlip et al. "Quantum Gravity: A Brief History of Ideas and Some Prospects". In: *Int. J. Mod. Phys.* D24.11 (2015), p. 1530028. DOI: 10.1142/S0218271815300281. arXiv:1507.08194 [gr-qc].

[11] *The Standard Model of elementary particles*. https://en.wikipedia.org/wiki/Standard_Model.

[12] Jerzy Bartke. *Introduction to relativistic heavy ion physics*. 2009.

[13] J. Beringer et al. "Review of Particle Physics*". In: *Phys. Rev. D* 86 (1 2012), p. 010001. DOI: 10.1103/PhysRevD.86.010001. URL: http://link.aps.org/doi/10.1103/PhysRevD.86.010001.

[14] Sahap Aybat Mert. “Studies in perturbative QCD”. PhD thesis. Stony Brook Univertity, 2007.

[15] K. Yagi, T. Hatsuda, and Y. Miake. “Quark-gluon plasma: From big bang to little bang”. In: *Camb. Monogr. Part. Phys. Nucl. Phys. Cosmol.* 23 (2005), pp. 1–446.

[16] David J. Gross and Frank Wilczek. “Ultraviolet Behavior of Nonabelian Gauge Theories”. In: *Phys. Rev. Lett.* 30 (1973), pp. 1343–1346. DOI: 10.1103/PhysRevLett.30.1343.

[17] H. David Politzer. “Reliable Perturbative Results for Strong Interactions?” In: *Phys. Rev. Lett.* 30 (1973), pp. 1346–1349. DOI: 10.1103/PhysRevLett.30.1346.

[18] Gines Martinez. “Advances in Quark Gluon Plasma”. In: 2013. arXiv:1304.1452 [nucl-ex].

[19] A. Bazavov et al. “The chiral and deconfinement aspects of the QCD transition”. In: *Phys. Rev.* D85 (2012), p. 054503. DOI: 10.1103/PhysRevD.85.054503. arXiv:1111.1710 [hep-lat].

[20] Tanmoy Bhattacharya et al. “QCD Phase Transition with Chiral Quarks and Physical Quark Masses”. In: *Phys. Rev. Lett.* 113.8 (2014), p. 082001. DOI: 10.1103/PhysRevLett.113.082001. arXiv:1402.5175 [hep-lat].

[21] F. Karsch. “Lattice QCD at high temperature and density”. In: *Lect. Notes Phys.* 583 (2002), pp. 209–249. DOI: 10.1007/3-540-45792-5_6. arXiv:hep-lat/0106019 [hep-lat].

[22] F. Karsch and E. Laermann. “Thermodynamics and in medium hadron properties from lattice QCD”. In: (2003). arXiv:hep-lat/0305025 [hep-lat].

[23] John C. Collins and M. J. Perry. “Superdense Matter: Neutrons Or Asymptotically Free Quarks?” In: *Phys. Rev. Lett.* 34 (1975), p. 1353. DOI: 10.1103/PhysRevLett.34.1353.

[24] Alberica Toia. “Participants and spectators at the heavy-ion fireball”. In: *CERN courier* 583 (2013). URL: http://cerncourier.com/cws/article/cern/53089.

[25] Michael L. Miller et al. “Glauber modeling in high energy nuclear collisions”. In: *Ann. Rev. Nucl. Part. Sci.* 57 (2007), pp. 205–243. DOI: 10.1146/annurev.nucl.57.090506.123020. arXiv:nucl-ex/0701025 [nucl-ex].

[26] F. Gelis. “Color Glass Condensate and Glasma”. In: *Int. J. Mod. Phys.* A28 (2013), p. 1330001. DOI: 10.1142/S0217751X13300019. arXiv:1211.3327 [hep-ph].

[27] Reinhard Stock. “Relativistic Nucleus-Nucleus Collisions and the QCD Matter Phase Diagram”. In: (2008). DOI: 10.1007/978-3-540-74203-6_7. arXiv:0807.1610 [nucl-ex].

[28] Peter Braun-Munzinger and Johanna Stachel. “The quest for the quark-gluon plasma”. In: *Nature* 448 (2007), pp. 302–309. DOI: 10.1038/nature06080.

[29] K. Adcox et al. “Formation of dense partonic matter in relativistic nucleus-nucleus collisions at RHIC: Experimental evaluation by the PHENIX collaboration”. In: *Nucl. Phys.* A757 (2005), pp. 184–283. DOI: 10.1016/j.nuclphysa.2005.03.086. arXiv:nucl-ex/0410003 [nucl-ex].

[30] Yves Schutz and Urs Achim Wiedemann. "Quark matter. Proceedings, 22nd International Conference on Ultra-Relativistic Nucleus-Nucleus Collisions, Quark Matter 2011, Annecy, France, May 23-28, 2011". In: *J. Phys.* G38 (2011), p. 120301. DOI: 10.1088/0954-3899/38/12/120301.

[31] Thomas Ullrich, Bolek Wyslouch, and John W. Harris. "Proceedings, 23rd International Conference on Ultrarelativistic Nucleus-Nucleus Collisions : Quark Matter 2012 (QM 2012)". In: *Nucl. Phys.* A904-905 (2013), pp. 1c–1092c.

[32] Peter Braun-Munzinger, Bengt Friman, and Johanna Stachel. "Proceedings, 24th International Conference on Ultra-Relativistic Nucleus-Nucleus Collisions (Quark Matter 2014)". In: *Nucl. Phys.* A931 (2014), pp.1–1266.

[33] Jaroslav Adam et al. "Anisotropic flow of charged particles in Pb-Pb collisions at $\sqrt{s_{\mathrm{NN}}} = 5.02$ TeV". In: *Phys. Rev. Lett.* 116.13 (2016), p. 132302. DOI: 10.1103/PhysRevLett.116.132302. arXiv:1602.01119 [nucl-ex].

[34] S. Voloshin and Y. Zhang. "Flow study in relativistic nuclear collisions by Fourier expansion of Azimuthal particle distributions". In: *Z. Phys.* C70 (1996), pp. 665–672. DOI: 10.1007/s002880050141. arXiv:hep-ph/9407282 [hep-ph].

[35] Raimond Snellings. "Elliptic Flow: A Brief Review". In: *New J. Phys.* 13 (2011), p. 055008. DOI: 10.1088/1367-2630/13/5/055008. arXiv:1102.3010 [nucl-ex].

[36] K Aamodt et al. "Elliptic flow of charged particles in Pb-Pb collisions at 2.76 TeV". In: *Phys. Rev. Lett.* 105 (2010), p. 252302. DOI: 10.1103/PhysRevLett.105.252302. arXiv:1011.3914 [nucl-ex].

[37] Richard P. Feynman. "Very high-energy collisions of hadrons". In: *Phys. Rev. Lett.* 23 (1969), pp. 1415–1417. DOI: 10.1103/PhysRevLett.23.1415.

[38] Sourav Sarkar, Helmut Satz, and Bikash Sinha. "The physics of the quark-gluon plasma". In: *Lect. Notes Phys.* 785 (2010), pp. 369. DOI: 10.1007/978-3-642-02286-9.

[39] J. F. Owens, E. Reya, and M. Gluck. "Detailed Quantum Chromodynamic Predictions for High p(T) Processes". In: *Phys. Rev.* D18 (1978), p. 1501. DOI: 10.1103/PhysRevD.18.1501.

[40] R. Baier et al. "Induced gluon radiation in a QCD medium". In: *Phys. Lett.* B345 (1995), pp. 277–286. DOI: 10.1016/0370-2693(94)01617-L. arXiv:hep-ph/9411409 [hep-ph].

[41] Xin-Nian Wang and Miklos Gyulassy. "Gluon shadowing and jet quenching in A + A collisions at s**(1/2) = 200-GeV". In: *Phys. Rev. Lett.* 68 (1992), pp. 1480–1483. DOI: 10.1103/PhysRevLett.68.1480.

[42] K. Adcox et al. "Suppression of hadrons with large transverse momentum in central Au+Au collisions at $\sqrt{s_{NN}}$ = 130-GeV". In: *Phys. Rev. Lett.* 88 (2002), p. 022301. DOI: 10.1103/PhysRevLett.88.022301. arXiv:nucl-ex/0109003 [nucl-ex].

[43] C. Adler et al. "Centrality dependence of high p_T hadron suppression in Au+Au collisions at $\sqrt{s}_{NN}$ = 130-GeV". In: *Phys. Rev. Lett.* 89 (2002), p. 202301. DOI: 10.1103/PhysRevLett.89.202301. arXiv:nucl-ex/0206011 [nucl-ex].

[44] Betty Bezverkhny Abelev et al. "Neutral pion production at midrapidity in pp and Pb-Pb collisions at $\sqrt{s_{\rm NN}} = 2.76\,\rm TeV$". In: *Eur. Phys. J.* C74.10 (2014), p. 3108. DOI: 10.1140/epjc/s10052-014-3108-8. arXiv:1405.3794 [nucl-ex].

[45] Betty Abelev et al. "Transverse momentum distribution and nuclear modification factor of charged particles in p-Pb collisions at $\sqrt{s_{NN}} = 5.02$ TeV". In: *Phys. Rev. Lett.* 110.8 (2013), p. 082302. DOI: 10.1103/PhysRevLett.110.082302. arXiv:1210.4520 [nucl-ex].

[46] T. Matsui and H. Satz. "J/ψ Suppression by Quark-Gluon Plasma Formation". In: *Phys. Lett.* B178 (1986), p. 416. DOI: 10.1016/0370-2693(86)91404-8.

[47] Helmut Satz. "Quarkonium Binding and Dissociation: The Spectral Analysis of the {QGP}". In: *Nuclear Physics A* 783.1–4 (2007). Proceedings of the 2nd International Conference on Hard and Electromagnetic Probes of High-Energy Nuclear CollisionsHard Probes 2006, pp. 249 –260. ISSN: 0375-9474. DOI: http://dx.doi.org/10.1016/j.nuclphysa.2006.11.026. URL: http://www.sciencedirect.com/science/article/pii/S0375947406008256.

[48] N. Brambilla et al. "Heavy quarkonium: progress, puzzles, and opportunities". In: *Eur. Phys. J.* C71 (2011), p. 1534. DOI: 10.1140/epjc/s10052-010-1534-9. arXiv:1010.5827 [hep-ph].

[49] A. Adare et al. "J/ψ suppression at forward rapidity in Au+Au collisions at $\sqrt{s_{NN}} = 200$ GeV". In: *Phys. Rev.* C84 (2011), p. 054912. DOI: 10.1103/PhysRevC.84.054912. arXiv:1103.6269 [nucl-ex].

[50] A. Andronic et al. "Statistical hadronization of charm in heavy ion collisions at SPS, RHIC and LHC". In: *Phys. Lett.* B571 (2003), pp. 36–44. DOI: 10.1016/j.physletb.2003.07.066. arXiv:nucl-th/0303036 [nucl-th].

[51] Jaroslav Adam et al. "Differential studies of inclusive J/ψ and ψ(2S) production at forward rapidity in Pb-Pb collisions at $\sqrt{s_{\rm NN}}$ = 2.76 TeV". In: (2015). arXiv:1506.08804 [nucl-ex].

[52] Betty Bezverkhny Abelev et al. "Centrality, rapidity and transverse momentum dependence of J/ψ suppression in Pb-Pb collisions at $\sqrt{s_{\rm NN}}$=2.76 TeV". In: *Phys. Lett.* B734 (2014), pp. 314–327. DOI: 10.1016/j.physletb.2014.05.064. arXiv:1311.0214 [nucl-ex].

[53] J. W. Cronin et al. "Production of Hadrons with Large Transverse Momentum at 200-GeV and 300-GeV." In: *Phys. Rev. Lett.* 31 (1973), pp. 1426–1429. DOI: 10.1103/PhysRevLett.31.1426.

[54] J. W. Cronin et al. “Production of hadrons with large transverse momentum at 200, 300, and 400 GeV”. In: *Phys. Rev.* D11 (1975), pp. 3105–3123. DOI: 10.1103/PhysRevD.11.3105.

[55] M. Lev and B. Petersson. “Nuclear Effects at Large Transverse Momentum in a QCD Parton Model”. In: *Z. Phys.* C21 (1983), p. 155. DOI: 10.1007/BF01648792.

[56] Michele Arneodo. “Nuclear effects in structure functions”. In: *Physics Reports* 240.5 (1994), pp. 301 –393. ISSN: 0370-1573. DOI: http://dx.doi.org/10.1016/0370-1573(94)90048-5. URL: http://www.sciencedirect.com/science/article/pii/0370157394900485.

[57] Nestor Armesto. “Nuclear shadowing”. In: *J. Phys.* G32 (2006), R367–R394. DOI: 10.1088/0954-3899/32/11/R01. arXiv:hep-ph/0604108 [hep-ph].

[58] Institute for Subatomic Physics. *Color-Glass Condensate*. http://www.uu.nl/en/research/institute-for-subatomic-physics/research/color-glass-condensate.

[59] A. L. S. Angelis et al. “A Comparison of the Production of π^0 Mesons in $p\bar{p}$ and pp Interactions at the CERN ISR”. In: *Phys. Lett.* B118 (1982), pp. 217–220. DOI: 10.1016/0370-2693(82)90631-1.

[60] C. Kourkoumelis et al. “Inclusive π^0 Production at Very Large p_T at the ISR”. In: *Phys. Lett.* B84 (1979), pp. 271–276. DOI: 10.1016/0370-2693(79)90301-0.

[61] A. L. S. Angelis et al. “A Measurement of Inclusive pi0 Production at Large p(T) from p p Collisions at the CERN ISR”. In: *Phys. Lett.* B79 (1978), pp. 505–510. DOI: 10.1016/0370-2693(78)90416-1.

[62] K. Eggert et al. “A Study of High Transverse Momentum pi0’s at ISR Energies”. In: *Nucl. Phys.* B98 (1975), pp. 49–72. DOI: 10.1016/0550-3213(75)90199-6.

[63] F. W. Busser et al. “A Study of High Transverse Momentum eta and pi0 Mesons at the CERN ISR”. In: *Phys. Lett.* B55 (1975), pp. 232–236. DOI: 10.1016/0370-2693(75)90450-5.

[64] A. Adare et al. “Measurement of neutral mesons in p+p collisions at $\overline{(}s)$= 200 GeV and scaling properties of hadron production”. In: *Phys. Rev.* D83 (2011), p. 052004. DOI: 10.1103/PhysRevD.83.052004. arXiv:1005.3674 [hep-ex].

[65] A. Adare et al. “Inclusive cross section and double helicity asymmetry for π^0 production in p^+p collisions at $\sqrt{s} = 62.4$ GeV”. In: *Phys. Rev.* D79 (2009), p. 012003. DOI: 10.1103/PhysRevD.79.012003. arXiv:0810.0701 [hep-ex].

[66] J. J. Sakurai. “Theory of strong interactions”. In: *Annals Phys.* 11 (1960), pp. 1–48. DOI: 10.1016/0003-4916(60)90126-3.

[67] G Tel-Zur. “Electron pair production in p-Be and p-Au collisions at 450 GeV/c”. PhD thesis. The weizmann Institute of Sicience, 1996. URL: http://cds.cern.ch/record/465996?ln=es.

[68] Norman M. Kroll and Walter Wada. "Internal pair production associated with the emission of high-energy gamma rays". In: *Phys. Rev.* 98 (1955), pp. 1355–1359. DOI: 10.1103/PhysRev.98.1355.

[69] L. G. Landsberg. "Electromagnetic Decays of Light Mesons". In: *Phys. Rept.* 128 (1985), pp. 301–376. DOI: 10.1016/0370-1573(85)90129-2.

[70] Lyndon Evans and Philip Bryant. "LHC Machine". In: *JINST* 3 (2008), S08001. DOI: 10.1088/1748-0221/3/08/S08001.

[71] The ATLAS Collaboration, G Aad, et al. "The ATLAS Experiment at the CERN Large Hadron Collider". In: *Journal of Instrumentation* 3.08 (2008), S08003. URL: http://stacks.iop.org/1748-0221/3/i=08/a=S08003.

[72] The CMS Collaboration, S Chatrchyan, et al. "The CMS experiment at the CERN LHC". In: *Journal of Instrumentation* 3.08 (2008), S08004. URL: http://stacks.iop.org/1748-0221/3/i=08/a=S08004.

[73] The LHCb Collaboration, A Augusto Alves Jr, et al. "The LHCb Detector at the LHC". In: *Journal of Instrumentation* 3.08 (2008), S08005. URL: http://stacks.iop.org/1748-0221/3/i=08/a=S08005.

[74] K. Aamodt et al. "The ALICE experiment at the CERN LHC". In: *JINST* 3 (2008), S08002. DOI: 10.1088/1748-0221/3/08/S08002.

[75] The TOTEM Collaboration et al. "The TOTEM Experiment at the CERN Large Hadron Collider". In: *Journal of Instrumentation* 3.08 (2008), S08007. URL: http://stacks.iop.org/1748-0221/3/i=08/a=S08007.

[76] James Pinfold et al. "Technical Design Report of the MoEDAL Experiment". In: (2009).

[77] The LHCf Collaboration et al. "The LHCf detector at the CERN Large Hadron Collider". In: *Journal of Instrumentation* 3.08 (2008), S08006. URL: http://stacks.iop.org/1748-0221/3/i=08/a=S08006.

[78] *The CERN accelerator complex*. http://cds.cern.ch/record/2119882/files/?ln=es.

[79] E. Abbas et al. "Centrality dependence of the pseudorapidity density distribution for charged particles in Pb–Pb collisions at". In: *Physics Letters B* 726.4–5 (2013), pp. 610–622. ISSN: 0370-2693. DOI: http://dx.doi.org/10.1016/j.physletb.2013.09.022. URL: http://www.sciencedirect.com/science/article/pii/S0370269313007399.

[80] K. Aamodt et al. "Charged-Particle Multiplicity Density at Midrapidity in Central Pb-Pb Collisions at $\sqrt{s_{NN}} = 2.76$ TeV". In: *Phys. Rev. Lett.* 105 (25 2010), p. 252301. DOI: 10.1103/PhysRevLett.105.252301. URL: http://link.aps.org/doi/10.1103/PhysRevLett.105.252301.

[81] ALICE Collaboration, J. Allen, et al. *ALICE DCal: An Addendum to the EMCal Technical Design Report Di-Jet and Hadron-Jet correlation measurements in ALICE*. Tech. rep. CERN-LHCC-2010-011. CERN, 2008. URL: http://cds.cern.ch/record/1272952/?ln=es.

[82] E. Abbas et al. “Performance of the ALICE VZERO system”. In: *JINST* 8 (2013), P10016. DOI: 10.1088/1748-0221/8/10/P10016. arXiv:1306.3130 [nucl-ex].

[83] A. Maevskaya. “Start and trigger detector t0 of the ALICE experiment”. In: *PoS* Baldin-ISHEPP-XXI (2012), p. 110.

[84] K Aamodt et al. “Alignment of the ALICE Inner Tracking System with cosmic-ray tracks”. In: *JINST* 5 (2010), P03003. DOI: 10.1088/1748-0221/5/03/P03003. arXiv:1001.0502 [physics.ins-det].

[85] Federico Antinori and Urs Wiedemann. “ALICE: Physics Performance Report, Volume II”. In: *Journal of Physics G: Nuclear and Particle Physics* 32.10 (2006). URL: http://stacks.iop.org/0954-3899/32/i=10/a=E01.

[86] J. Alme et al. “The ALICE TPC, a large 3-dimensional tracking device with fast readout for ultra-high multiplicity events”. In: *Nucl. Instrum. Meth.* A622 (2010), pp. 316–367. DOI: 10.1016/j.nima.2010.04.042. arXiv:1001.1950 [physics.ins-det].

[87] A. Alici. “Particle identification with the ALICE Time-Of-Flight detector at the LHC”. In: *Nucl. Instrum. Meth.* A766 (2014), pp. 288–291. DOI: 10.1016/j.nima.2014.05.059.

[88] D. De Gruttola. “Particle IDentification with the ALICE Time-Of-Flight detector at the LHC”. In: *JINST* 9.10 (2014), p. C10019. DOI: 10.1088/1748-0221/9/10/C10019.

[89] ALICE Collaboration, P. Cortese, et al. *ALICE transition-radiation detector : Technical Design Report*. Tech. rep. CERN-LHCC-2001-021. CERN, 2001. URL: https://cds.cern.ch/record/519145?ln=en.

[90] Jochen Klein. “Jet Physics with A Large Ion Collider Experiment at the Large Hadron Collider”. PhD thesis. Heidelberg U., 2014. URL: https://inspirehep.net/record/1339771/files/CERN-THESIS-2014-186.pdf.

[91] ALICE Collaboration, G. Dellacasa, et al. *ALICE Photon Spectrometer (PHOS) : Technical Design Report*. Tech. rep. CERN-LHCC-99-004. CERN, 1999. URL: https://cds.cern.ch/record/381432?ln=es.

[92] ALICE Collaboration, P. Cortese, et al. *ALICE Electromagnetic Calorimeter Technical Design Report*. Tech. rep. CERN-LHCC-2008-014. CERN, 2008. URL: http://cds.cern.ch/record/1121574/?ln=es.

[93] J. Allen et al. “Performance of prototypes for the ALICE electromagnetic calorimeter”. In: *Nucl. Instrum. Meth.* A615 (2010), pp. 6–13. DOI: 10.1016/j.nima.2009.12.061. arXiv:0912.2005 [physics.ins-det].

[94] ALICE Collaboration. "*AliRoot, ALICE Off-line framework for simulation, reconstruction and analysis*". http://aliweb.cern.ch/Offline/.

[95] Rene Brun and Fons Rademakers. “{ROOT} — An object oriented data analysis framework”. In: *Nuclear Instruments and Methods in Physics Research Section A: Accelerators, Spectrometers, Detectors and Associated Equipment* 389.1–2 (1997). New Computing Techniques in Physics Research V, pp. 81 –86. ISSN: 0168-9002. DOI: http://dx.doi.org/10.1016/S0168-9002(97)00048-X. URL: http://www.sciencedirect.com/science/article/pii/S016890029700048X.

[96] ALICE Collaboration, P. Cortese, et al. *ALICE computing: Technical Design Report*. Tech. rep. CERN-LHCC-2005-018. CERN, 2005. URL: http://aliceinfo.cern.ch/Documents/TDR/Computing.html.

[97] Torbjorn Sjostrand, Stephen Mrenna, and Peter Z. Skands. “PYTHIA 6.4 Physics and Manual”. In: *JHEP* 05 (2006), p. 026. DOI: 10.1088/1126-6708/2006/05/026. arXiv:hep-ph/0603175 [hep-ph].

[98] Ralph Engel. *PHOJET Manual*. http://physik.unileipzig.de/eng/phojet.html.

[99] Xin-Nian Wang and Miklos Gyulassy. “HIJING: A Monte Carlo model for multiple jet production in p p, p A and A A collisions”. In: *Phys. Rev.* D44 (1991), pp. 3501–3516. DOI: 10.1103/PhysRevD.44.3501.

[100] Stefan Roesler, Ralph Engel, and Johannes Ranft. “The Monte Carlo event generator DPMJET-III”. In: *Advanced Monte Carlo for radiation physics, particle transport simulation and applications. Proceedings, Conference, MC2000, Lisbon, Portugal, October 23-26, 2000*. 2000, pp. 1033–1038. DOI: 10.1007/978-3-642-18211-2_166. arXiv:hep-ph/0012252 [hep-ph]. URL: http://www-public.slac.stanford.edu/sciDoc/docMeta.aspx?slacPubNumber=SLAC-PUB-8740.

[101] Rene Brun, Federico Carminati, and Simone Giani. “GEANT Detector Description and Simulation Tool”. In: (1994).

[102] S. Agostinelli et al. “GEANT4: A Simulation toolkit”. In: *Nucl. Instrum. Meth.* A506 (2003), pp. 250–303. DOI: 10.1016/S0168-9002(03)01368-8.

[103] Alfredo Ferrari et al. “FLUKA: A multi-particle transport code (Program version 2005)”. In: (2005).

[104] Betty Bezverkhny Abelev et al. “Performance of the ALICE Experiment at the CERN LHC”. In: *Int. J. Mod. Phys.* A29 (2014), p. 1430044. DOI: 10.1142/S0217751X14300440. arXiv:1402.4476 [nucl-ex].

[105] B. S. Nilsen, Luigi Vannucci, and N. Bustreo. “Finding the vertex position using the SPD in stand alone mode and the effects of the off-axis vertexm pt.1”. In: (2001).

[106] Pierre Billoir. “Progressive track recognition with a Kalman like fitting procedure”. In: *Comput. Phys. Commun.* 57 (1989), pp. 390–394. DOI: 10.1016/0010-4655(89)90249-X.

[107] ALICE Collaboration. *ALICE figure repository*. https://aliceinfo.cern.ch/Figure/node/4354.

[108] ALICE Collaboration. *ALICE figure repository*. https://aliceinfo.cern.ch/Figure/node/1147.

[109] J. Podolanski and R. Armenteros. "Analysis of v-events". In: *Phil. Mag.* 7 (1954).

[110] Jaroslav Adam et al. "Particle identification in ALICE: a Bayesian approach". In: (2016). arXiv:1602.01392 [physics.data-an].

[111] ALICE Collaboration. *ALICE figure repository*. https://aliceinfo.cern.ch/Figure/node/942.

[112] *MonALISA Repository for ALICE*. http://alimonitor.cern.ch/map.jsp.

[113] Ian Foster and Carl Kesselman, eds. *The Grid: Blueprint for a New Computing Infrastructure*. San Francisco, CA, USA: Morgan Kaufmann Publishers Inc., 1999. ISBN: 1-55860-475-8.

[114] *The MONARC Project*. http://www.cern.ch/MONARC.

[115] ALICE Collaboration. *MonALISA Repository for ALICE*. http://alimonitor.cern.ch/map.jsp.

[116] P. Saiz et al. "AliEn—ALICE environment on the {GRID}". In: *Nuclear Instruments and Methods in Physics Research Section A: Accelerators, Spectrometers, Detectors and Associated Equipment* 502.2–3 (2003). Proceedings of the {VIII} International Workshop on Advanced Computing and Analysis Techniques in Physics Research, pp. 437 –440. ISSN: 0168-9002. DOI: http://dx.doi.org/10.1016/S0168-9002(03)00462-5. URL: http://www.sciencedirect.com/science/article/pii/S0168900203004625.

[117] Yves Schutz. *Quality Assurance*. http://aliweb.cern.ch/Offline/Activities/QA.html.

[118] Gerhard A. Schuler and Torbjorn Sjostrand. "Hadronic diffractive cross-sections and the rise of the total cross-section". In: *Phys. Rev.* D49 (1994), pp. 2257–2267. DOI: 10.1103/PhysRevD.49.2257.

[119] H. L. Lai et al. "Global QCD analysis of parton structure of the nucleon: CTEQ5 parton distributions". In: *Eur. Phys. J.* C12 (2000), pp. 375–392. DOI: 10.1007/s100529900196. arXiv:hep-ph/9903282 [hep-ph].

[120] T. Sjostrand and Peter Z. Skands. "Transverse-momentum-ordered showers and interleaved multiple interactions". In: *Eur. Phys. J.* C39 (2005), pp. 129–154. DOI: 10.1140/epjc/s2004-02084-y. arXiv:hep-ph/0408302 [hep-ph].

[121] B. Andersson et al. "Parton fragmentation and string dynamics". In: *Physics Reports* 97.2–3 (1983), pp. 31 –145. ISSN: 0370-1573. DOI: http://dx.doi.org/10.1016/0370-1573(83)90080-7. URL: http://www.sciencedirect.com/science/article/pii/0370157383900807.

[122] A. Capella et al. "Dual parton model". In: *Phys. Rept.* 236 (1994), pp. 225–329. DOI: 10.1016/0370-1573(94)90064-7.

[123] A. Capella, J. Tran Thanh Van, and J. Kwiecinski. “Mini - Jets, QCD and Unitarity”. In: *Phys. Rev. Lett.* 58 (1987), p. 2015. DOI: 10.1103/PhysRevLett.58.2015.

[124] V. Gribov and L.N. Lipatov. In: *Sov. J. Nucl. Phys* 15 (1972), 438 and 675.

[125] L. N. Lipatov. “The parton model and perturbation theory”. In: *Sov. J. Nucl. Phys.* 20 (1975). [Yad. Fiz.20,181(1974)], pp. 94–102.

[126] Guido Altarelli and G. Parisi. “Asymptotic Freedom in Parton Language”. In: *Nucl. Phys.* B126 (1977), p. 298. DOI: 10.1016/0550-3213(77)90384-4.

[127] Yuri L. Dokshitzer. “Calculation of the Structure Functions for Deep Inelastic Scattering and e+ e- Annihilation by Perturbation Theory in Quantum Chromodynamics.” In: *Sov. Phys. JETP* 46 (1977). [Zh. Eksp. Teor. Fiz.73,1216(1977)], pp. 641–653.

[128] Bo Andersson, G. Gustafson, and B. Nilsson-Almqvist. “A Model for Low p(t) Hadronic Reactions, with Generalizations to Hadron - Nucleus and Nucleus-Nucleus Collisions”. In: *Nucl. Phys.* B281 (1987), p. 289. DOI: 10.1016/0550-3213(87)90257-4.

[129] Bo Nilsson-Almqvist and Evert Stenlund. “Interactions Between Hadrons and Nuclei: The Lund Monte Carlo, Fritiof Version 1.6”. In: *Comput. Phys. Commun.* 43 (1987), p. 387. DOI: 10.1016/0010-4655(87)90056-7.

[130] J. Ranft. “Hadron Production in Hadron - Nucleus and Nucleus-nucleus Collisions in the Dual Monte Carlo Multichain Fragmentation Model”. In: *Phys. Rev.* D37 (1988), p. 1842. DOI: 10.1103/PhysRevD.37.1842.

[131] J. Ranft. “Transverse Energy Distributions in Nucleus-Nucleus Collisions in the Dual Monte Carlo Multichain Fragmentation Model”. In: *Phys. Lett.* B188 (1987), p. 379. DOI: 10.1016/0370-2693(87)91401-8.

[132] Torbjorn Sjostrand and Maria van Zijl. “A Multiple Interaction Model for the Event Structure in Hadron Collisions”. In: *Phys. Rev.* D36 (1987), p. 2019. DOI: 10.1103/PhysRevD.36.2019.

[133] Torbjorn Sjostrand. “The Lund Monte Carlo for Jet Fragmentation and e+ e- Physics: Jetset Version 6.2”. In: *Comput. Phys. Commun.* 39 (1986), pp. 347–407. DOI: 10.1016/0010-4655(86)90096-2.

[134] Torbjorn Sjostrand and Mats Bengtsson. “The Lund Monte Carlo for Jet Fragmentation and e+ e- Physics. Jetset Version 6.3: An Update”. In: *Comput. Phys. Commun.* 43 (1987), p. 367. DOI: 10.1016/0010-4655(87)90054-3.

[135] "*AliRoot documentation: Definition of AliEvent class*". "http://aliroot-docs.web.cern.ch/aliroot-docs/AliVEvent.html.

[136] *LHC Filling Schemes*. http://lpc.web.cern.ch/lpc/fillingschemes.htm.

[137] S. Bufalino. “Performance of ALICE Silicon Tracking Detectors”. In: *PoS* Vertex2012 (2013), p. 048.

[138] Betty Abelev et al. “Measurement of inelastic, single- and double-diffraction cross sections in proton–proton collisions at the LHC with ALICE”. In: *Eur. Phys. J.* C73.6 (2013), p. 2456. DOI: 10.1140/epjc/s10052-013-2456-0. arXiv:1208.4968 [hep-ex].

[139] Torsten Dahms. “Measurement of photons via conversion pairs with the PHENIX experiment at RHIC”. MA thesis. SUNY, Stony Brook, 2005. URL: http://www.phenix.bnl.gov/phenix/WWW/publish/tdahms/master-thesis/tdahms_thesis.pdf.

[140] Friederike Bock. “Neutral Pion and Eta Meson Production in pp and Pb–Pb Collisions at the LHC with the ALICE Detector”. MA thesis. Heidelberg U., 2012. URL: http://www.physi.uni-heidelberg.de/~fbock/Masterthesis.pdf.

[141] Kathrin Koch. “Measurement of π^0 and eta mesons with photon conversions in ALICE in proton-proton collisions at $\sqrt{s}$ = 0.9, 2.76, 7 TeV”. PhD thesis. Heidelberg U., 2012. URL: http://www.ub.uni-heidelberg.de/archiv/13113.

[142] S. Gorbunov and I. Kisel. *Reconstruction of decayed particles based on the Kalman Filter*. 2007. URL: http://www.star.bnl.gov/~bouchet/KFParticle/DOC-2007-May-14-1.pdf.

[143] Friederike Bock. *ALICE figure repository*. https://aliceinfo.cern.ch/Figure/node/1173.

[144] G. I. Kopylov. “Like particle correlations as a tool to study the multiple production mechanism”. In: *Phys. Lett.* B50 (1974), pp. 472–474. DOI: 10.1016/0370-2693(74)90263-9.

[145] T. Matulewicz et al. “RESPONSE OF BaF-2 DETECTORS TO PHOTONS OF 3-MeV TO 50=MeV ENERGY”. In: (1990).

[146] B. Abelev et al. “Neutral pion and η meson production in proton-proton collisions at $\sqrt{s} = 0.9$ TeV and $\sqrt{s} = 7$ TeV”. In: *Phys. Lett.* B717 (2012), pp. 162–172. DOI: 10.1016/j.physletb.2012.09.015. arXiv:1205.5724 [hep-ex].

[147] G. D. Lafferty and T. R. Wyatt. “Where to stick your data points: The treatment of measurements within wide bins”. In: *Nucl. Instrum. Meth.* A355 (1995), pp. 541–547. DOI: 10.1016/0168-9002(94)01112-5.

[148] Constantino Tsallis. “Possible Generalization of Boltzmann-Gibbs Statistics”. In: *J. Statist. Phys.* 52 (1988), pp. 479–487. DOI: 10.1007/BF01016429.

[149] Roger Barlow. “Systematic errors: Facts and fictions”. In: *Advanced Statistical Techniques in Particle Physics. Proceedings, Conference, Durham, UK, March 18-22, 2002*. 2002, pp. 134–144. arXiv:hep-ex/0207026 [hep-ex]. URL: http://www.ippp.dur.ac.uk/Workshops/02/statistics/proceedings//barlow.pdf.

[150] Pedro González Zamora. “Dalitz-EMCAL and Dalitz-PHOS π^0 analysis”. PWG-GA General Meeting. May 2015. URL: https://indico.cern.ch/event/364049.

[151] T. Okubo et al. “Measurements of neutral π^0 meson production in p-Pb collisions at $\sqrt{s_{NN}}$ = 5.02 TeV with PHOS detector at ALICE”. ALICE Analysis Note. 2014. URL: https://aliceinfo.cern.ch/Notes/node/413.

[152] J. Kamin et al. "π^0 Measured by the EMCal in p-Pb collisions at $\sqrt{s_{NN}}$ = 5.02 TeV". ALICE Analysis Note. 2014. URL: https://aliceinfo.cern.ch/Notes/node/327.

[153] Daniel de Florian et al. "Parton-to-Pion Fragmentation Reloaded". In: *Phys. Rev.* D91.1 (2015), p. 014035. DOI: 10.1103/PhysRevD.91.014035. arXiv:1410.6027 [hep-ph].

[154] Rodolfo Sassot, Pia Zurita, and Marco Stratmann. "Inclusive Hadron Production in the CERN-LHC Era". In: *Phys. Rev.* D82 (2010), p. 074011. DOI: 10.1103/PhysRevD.82.074011. arXiv:1008.0540 [hep-ph].

[155] A. D. Martin et al. "Parton distributions for the LHC". In: *Eur. Phys. J.* C63 (2009), pp. 189–285. DOI: 10.1140/epjc/s10052-009-1072-5. arXiv:0901.0002 [hep-ph].

[156] Daniel de Florian, Rodolfo Sassot, and Marco Stratmann. "Global analysis of fragmentation functions for pions and kaons and their uncertainties". In: *Phys. Rev.* D75 (2007), p. 114010. DOI: 10.1103/PhysRevD.75.114010. arXiv:hep-ph/0703242 [HEP-PH].

[157] L. Adamczyk et al. "Neutral pion cross section and spin asymmetries at intermediate pseudorapidity in polarized proton collisions at $\sqrt{s} = 200$ GeV". In: *Phys. Rev. D* 89 (1 2014), p. 012001. DOI: 10.1103/PhysRevD.89.012001. URL: http://link.aps.org/doi/10.1103/PhysRevD.89.012001.

[158] B. I. Abelev et al. "Longitudinal double-spin asymmetry and cross section for inclusive neutral pion production at midrapidity in polarized proton collisions at $\sqrt{s} = 200$ GeV". In: *Phys. Rev.* D80 (2009), p. 111108. DOI: 10.1103/PhysRevD.80.111108. arXiv:0911.2773 [hep-ex].

[159] G. Agakishiev et al. "Identified Hadron Compositions in $p + p$ and $\mathrm{Au} + \mathrm{Au}$ Collisions at High Transverse Momenta at $\sqrt{s_{NN}} = 200$ GeV". In: *Phys. Rev. Lett.* 108 (7 2012), p. 072302. DOI: 10.1103/PhysRevLett.108.072302. URL: http://link.aps.org/doi/10.1103/PhysRevLett.108.072302.

[160] J. Pumplin, D. R. Stump, and W. K. Tung. "Multivariate fitting and the error matrix in global analysis of data". In: *Phys. Rev. D* 65 (1 2001), p. 014011. DOI: 10.1103/PhysRevD.65.014011. URL: http://link.aps.org/doi/10.1103/PhysRevD.65.014011.

[161] Torbjorn Sjostrand, Stephen Mrenna, and Peter Z. Skands. "A Brief Introduction to PYTHIA 8.1". In: *Comput. Phys. Commun.* 178 (2008), pp. 852–867. DOI: 10.1016/j.cpc.2008.01.036. arXiv:0710.3820 [hep-ph].

[162] Richard Corke and Torbjorn Sjostrand. "Interleaved Parton Showers and Tuning Prospects". In: *JHEP* 03 (2011), p. 032. DOI: 10.1007/JHEP03(2011)032. arXiv:1011.1759 [hep-ph].

[163] Astrid Morreale. "Measurement of neutral mesons in pp and Pb-Pb collisions at mid-rapidity with ALICE". In: 2015. arXiv:1512.05250 [nucl-ex]. URL: https://inspirehep.net/record/1409972/files/arXiv:1512.05250.pdf.

[164] A. Passfeld et al. “Neutral meson measurement via photon conversions in p-Pb collisions at $\sqrt{s_{NN}}$ = 5.02 TeV with ALICE at the LHC”. ALICE Analysis Note. 2014. URL: https://aliceinfo.cern.ch/Notes/node/285.

[165] A. A. Bylinkin and A. A. Rostovtsev. “Parametrization of the shape of hadron-production spectra in high-energy particle interactions”. In: *Phys. Atom. Nucl.* 75 (2012). [Yad. Fiz.75,1060(2012)], pp. 999–1005. DOI: 10.1134/S1063778812040047.

[166] Jaroslav Adam et al. “Multiplicity dependence of charged pion, kaon, and (anti)proton production at large transverse momentum in p-Pb collisions at $\sqrt{s_{\rm NN}}$ = 5.02 TeV”. In: (2016). arXiv:1601.03658 [nucl-ex].

[167] Betty Bezverkhny Abelev et al. “Transverse momentum dependence of inclusive primary charged-particle production in p-Pb collisions at $\sqrt{s_{\rm NN}} = 5.02$ TeV”. In: *Eur. Phys. J.* C74.9 (2014), p. 3054. DOI: 10.1140/epjc/s10052-014-3054-5. arXiv:1405.2737 [nucl-ex].

[168] S. S. Adler et al. “Absence of Suppression in Particle Production at Large Transverse Momentum in $\sqrt{s_{NN}} = 200$ GeV $d + \mathrm{Au}$ Collisions”. In: *Phys. Rev. Lett.* 91 (7 2003), p. 072303. DOI: 10.1103/PhysRevLett.91.072303. URL: http://link.aps.org/doi/10.1103/PhysRevLett.91.072303.

[169] Ilkka Helenius et al. “Impact-Parameter Dependent Nuclear Parton Distribution Functions: EPS09s and EKS98s and Their Applications in Nuclear Hard Processes”. In: *JHEP* 07 (2012), p. 073. DOI: 10.1007/JHEP07(2012)073. arXiv:1205.5359 [hep-ph].

[170] K. J. Eskola, H. Paukkunen, and C. A. Salgado. “EPS09: A New Generation of NLO and LO Nuclear Parton Distribution Functions”. In: *JHEP* 04 (2009), p. 065. DOI: 10.1088/1126-6708/2009/04/065. arXiv:0902.4154 [hep-ph].

[171] Daniel Stump et al. “Inclusive jet production, parton distributions, and the search for new physics”. In: *JHEP* 10 (2003), p. 046. DOI: 10.1088/1126-6708/2003/10/046. arXiv:hep-ph/0303013 [hep-ph].

[172] T. Lappi and H. Mäntysaari. “Single inclusive particle production at high energy from HERA data to proton-nucleus collisions”. In: *Phys. Rev.* D88 (2013), p. 114020. DOI: 10.1103/PhysRevD.88.114020. arXiv:1309.6963 [hep-ph].

[173] F. D. Aaron et al. “Combined Measurement and QCD Analysis of the Inclusive e+-p Scattering Cross Sections at HERA”. In: *JHEP* 01 (2010), p. 109. DOI: 10.1007/JHEP01(2010)109. arXiv:0911.0884 [hep-ex].

[174] Larry D. McLerran and Raju Venugopalan. “Computing quark and gluon distribution functions for very large nuclei”. In: *Phys. Rev.* D49 (1994), pp. 2233–2241. DOI: 10.1103/PhysRevD.49.2233. arXiv:hep-ph/9309289 [hep-ph].